PROPAGATION OF ELF WAVES GENERATED BY AN HF IONOSPHERIC HEATER IN THE EARTH'S PLASMA ENVIRONMENT

A DISSERTATION

SUBMITTED TO THE DEPARTMENT OF ELECTRICAL ENGINEERING

AND THE COMMITTEE ON GRADUATE STUDIES

OF STANFORD UNIVERSITY

IN PARTIAL FULFILLMENT OF THE REQUIREMENTS

FOR THE DEGREE OF

DOCTOR OF PHILOSOPHY

Denys Piddyachiy

December 2012

This dissertation is online at: http://purl.stanford.edu/yq198fk7787

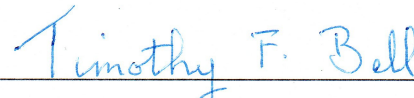A copy is also online at: http://vlf.stanford.edu/pubs/theses

Denys Piddyachiy

I certify that I have read this dissertation and that, in my opinion, it is fully adequate in scope and quality as a dissertation for the degree of Doctor of Philosophy.
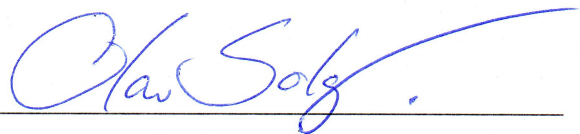
_____

(Umran S. Inan)   Principal Adviser

I certify that I have read this dissertation and that, in my opinion, it is fully adequate in scope and quality as a dissertation for the degree of Doctor of Philosophy.

_____

(Timothy F. Bell)

I certify that I have read this dissertation and that, in my opinion, it is fully adequate in scope and quality as a dissertation for the degree of Doctor of Philosophy.

_____

(Olav Solgaard)

Approved for the University Committee on Graduate Studies

_____

iii

This dissertation is dedicated to my mother and father

Lyudmila *and* Valeriy

Abstract

Electromagnetic waves in the Extremely Low Frequency range (ELF, 30–3000 Hz) have broad application in physics and engineering such as ionospheric and underground remote sensing and global submarine communications. Additionally, ELF waves can resonantly interact with energetic electrons, an important process that results in the removal of trapped electrons from the radiation belts. ELF waves can be generated by lightning discharges and by natural processes in the Earth's magnetosphere. However, it is extremely difficult to generate ELF waves artificially due to their long wavelengths. In this work, the High Frequency Active Auroral Research Program (HAARP) transmitter array is used to generate ELF waves. The HAARP array generates ELF waves by heating the lower ionosphere with a powerful (3.6 MW) high frequency (2.75–10 MHz) beam. The heating is modulated at an ELF frequency resulting in modulation of the natural auroral electrojet current, which in turn radiates at the ELF frequency. For four years, a set of experiments was conducted in which ELF signals generated by HAARP were detected by the DEMETER satellite at an altitude of 670 km. In addition to observations, the distribution of ELF power is examined with several modeling techniques to explain the observed features.

In the experiments and modeling, three distinct regions of ELF radiation are identified. Region 1, the most important region, is a column of radiation propagating upward into space with a horizontal extent of about the size of the heated region (50–100 km) and average field strengths of 100–150 μV$\cdot$m^{-1} at 2 kHz. In Region 2, which can extend up to 300 km laterally from HAARP, it is believed that the waves reach the satellite by propagating directly from the source in the ionosphere without reflection from the ground. In contrast, in Region 3, which can extend to 1000 km

from HAARP, the generated waves first propagate in the Earth-ionosphere waveguide and partially leak through the ionosphere to be detected on the spacecraft.

During the nighttime, the intense column of radiation (Region 1) is displaced by about 100 km horizontally to the south from the HAARP field line. During the daytime, there is no substantial north-south displacement from the HAARP field line. A horizontally homogeneous full-wave model is used to facilitate the physical understanding of the wave propagation. The model accurately predicts the extents of the three regions during daytime and nighttime conditions as well as the location of Region 1 during daytime. However, during the nighttime the model predicts that the column should be up to 100 km north of the HAARP field line. It is proposed that the displacement in observations during the nighttime is caused by a horizontal electron density gradient within the main ionospheric trough. Using ray tracing simulations, we estimate that the gradient of this trough should be an order of magnitude change over a latitude range of 3–5°. It is also demonstrated that the main ionospheric trough is an important parameter of the medium above HAARP not only for ELF observations but also for other types of experiments too. It is found to occur over HAARP during the nighttime in at least 50% of our cases.

The first satellite observations of one-hop and two-hop ELF waves generated via HF heating are reported. Among the important new understandings is the fact that daytime is preferential for this type of ELF generation and propagation to the conjugate region. The signal during the daytime is observed almost two times more often than during the nighttime, and triggered emissions are observed only in the daytime. We also find that the region with the strongest signal is displaced about 300 km toward the equator, and the signal is overall higher toward the equator than toward the pole. It is hypothesized that this can be the result of plasmapause guiding. Another important result is the fact that one/two-hop signals are observed over a long range of distances (> 1000 km) and over a wide range of L-shells, although always with roughly constant time delay. This observation suggests that the propagation in the magnetosphere is within the narrow range of L-shells or within a duct, and wide range in the observations is the result of ELF wave backscattering from the ionosphere.

Acknowledgments

There is no other place in the world as Stanford, intellectually and culturally. I am grateful to many people here from whom I had a chance to learn about science, technology and life during the years of Ph.D. studies.

First and foremost, I would like to thank my principal adviser, Prof. Umran Inan. He made a big leap of faith when he accepted me to his group while I was doing research across the ocean in Ukraine. This single event changed my career and personal life substantially. Umran has always believed in abilities of his students to complete the most challenging tasks and this has given everyone strength to tackle difficult problems. He is always completely devoted to and fascinated by the work he is doing. This devotion always encouraged me a lot and left no doubt that we are doing world class research. I am also extremely grateful to my associate adviser Dr. Timothy Bell. Tim possesses an incredible amount of knowledge in our field. He was the most useful person to consult with at the last and deep stage of this work. He has always been available for scientific and personal advises. Additionally, I thank Prof. Olav Solgaard for taking his precious time to serve in the defense committee and to read the dissertation. I would also like to thank my previous mentors at the Institute of Radio Astronomy of Ukraine Prof. Yuri Yamplosky and Dr. Victor Sinitsin who introduced me to scientific research and helped me in the selection of graduate school. Additionally, I thank Prof. Oleg Tyrnov and Prof. Victor Rozumenko who introduced me to space physics and wave propagation at Karazin Kharkiv University.

I especially would like to thank Nikolai Lehtinen who is one of the brightest theorists in my opinion. Discussions with him helped me a lot in the interpretation of the observations. Nikolai has become my best friend during the years at Stanford

Contents

List of Tables

List of Figures

Chapter 1

Introduction

'Try to learn something about everything and everything about something.[1] '

The subject of this work is the propagation of extremely low frequency (ELF) electromagnetic waves between 30–3000 Hz in the Earth's space environment. The ELF waves are generated in the lower ionosphere at an altitude of about 75 km as a result of the interaction of powerful high frequency (HF) electromagnetic waves with the natural currents in the ionosphere. The HF waves between 3–10 MHz frequency are produced by a man-made transmitter on the ground. The propagation of ELF waves is affected by the parameters of the HF transmissions and the properties of both the source region and the region of wave propagation. To study wave propagation, a series of experiments have been performed, the acquired data have been analyzed, and several numerical models have been used for the interpretation of new results. The emphasis of this work is on satellite observations of ELF wave propagation and on the simulation of ELF wave propagation in space. In this chapter, we briefly introduce the basic concepts used in the discussion of wave propagation, present the history and motivation of the research, and describe the structure of the work and specific contributions.

---

[1]Thomas Huxley (1825–1895), a British biologist and a prominent defender of Darwin's theory of evolution. He devised the words "agnostic" and "agnosticism".

1.1   The Earth's Magnetic Field

The propagation of electromagnetic waves in plasmas is affected by the presence of a magnetic field [*Inan and Gołkowski*, 2010, Chap. 10]. The absolute value of the magnetic field B defines an important parameter in plasma physics – the particle gyrofrequency $\omega_c = |q|\, B/m$, where q and m are correspondingly the charge and the mass of a charged particle. In this section, we will briefly describe the properties of the Earth's magnetic field $\mathbf{B_0}$ that affect the propagation of ELF waves.

It is a currently accepted hypothesis that the main field of the Earth is produced by the motion of an electrically conductive fluid in the Earth's core [*Tascione*, 2010, Ch. 4]. This main field constitutes about 99% of the magnetic field on the ground and in the ionosphere. The time scale of the main field variations are much larger than the time scales in our work (several minutes at most) so that this field can be considered stationary in all our calculations.

To a first approximation, the Earth's magnetic field is that of a dipole whose axis is tilted about 11° from the spin axis of the Earth. The Earth's magnetic field can be expressed as a gradient of a scalar potential Φ:

$$\mathbf{B_0} = -\nabla\Phi, \tag{1.1a}$$

$$\Phi = \frac{\mathbf{M} \cdot \mathbf{r}}{r^3}, \tag{1.1b}$$

where $\mathbf{r}$ is a radius-vector from the center of the Earth and $\mathbf{M}$ is a dipole magnetic moment with current magnitude of about 8×10^{15} T·m^3. The plane through the center of the Earth perpendicular to the dipole axis is called the magnetic equatorial plane. A spherical coordinate system that is fixed with respect to the dipole moment is often adopted. In this system the magnetic latitude θ is calculated from the magnetic equator. The equation for the magnetic field line in this spherical coordinate system can be written as

$$r = L \cos^2 \theta, \tag{1.2}$$

where r and L are often measured in Earth radii ($R_E = 6371.2$ km). The parameter L gives the number of Earth's radii at which a given field line intersects the magnetic equator. It is also called the McIlwain parameter [*McIlwain*, 1961] or L-shell because in three dimensions it uniquely identifies a specific 3D surface or shell that crosses the magnetic equator at L Earth radii. Figure 1.1 shows schematically the magnetic equator (solid line) and magnetic field lines (dashed) with corresponding L-shell numbers.
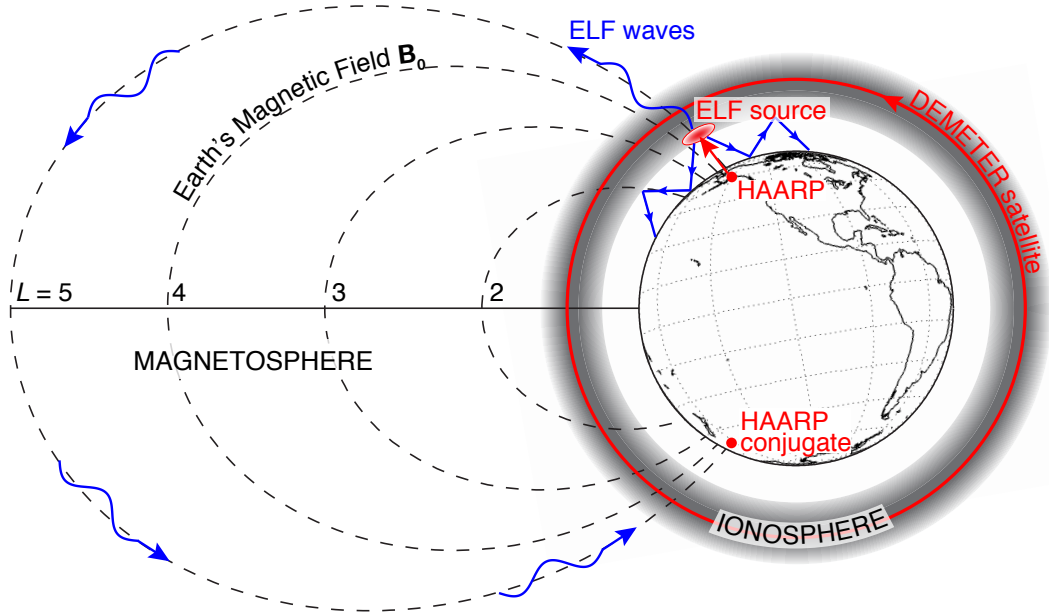
Figure 1.1: A schematic of the part of the Earth's Environment considered in this work together with several key concepts. The ionosphere altitude is not to scale; in reality it lies between 60–2000 km in altitude.

There exists a more precise model of the Earth's main magnetic field called the International Geomagnetic Reference Field or IGRF [*Finlay et al.*, 2010]. This model is based on a fit to observations collected by satellites, and magnetic observatories, as well as to data from magnetic surveys using a spherical harmonic analysis. This fit gives a field accuracy on the ground of about 0.5%. The model is revised every five years and is openly available. In the IGRF model, the magnetic field is also calculated

through a magnetic potential Φ (equation 1.1a) which is represented as the following:

$$\Phi = R_E \sum_{n=1}^{N} \sum_{m=0}^{n} \left(\frac{R_E}{r}\right)^{n+1} [g_n^m \cos m\phi + h_n^m \sin m\phi] P_n^m(\cos \vartheta), \qquad (1.3)$$

where ϑ denotes geocentric co-latitude, ϕ denotes east longitude, and $P_n^m(\cos \vartheta)$ are the Schmidt semi-normalized associated Legendre functions of degree n and order m. The maximum spherical harmonic degree of the expansion is at least $N = 10$. The Gauss coefficients g_n^m and h_n^m are calculated by a fit to the experimental measurements at multiple locations.

Using the IGRF model in a similar fashion as the dipole model, it is possible to develop a geomagnetic coordinate system. The L-shell parameter can also be calculated more precisely using the IGRF model. In all our numerical computations, the IGRF model is used for the calculation of the main magnetic field and the L-shells.

If we select some point on the ground, we can always trace a path along the magnetic field line of this point to the opposite hemisphere. The location where this field line crosses the Earth's surface in the opposite hemisphere is called the conjugate point. Figure 1.1 shows the location of HAARP and the geomagnetic conjugate point of HAARP. Similarly, we can always trace the path along the field line starting at some location in the ionosphere (or elsewhere) and find a point which is conjugate to this location in the opposite hemisphere.

1.2   The Ionosphere

The Earth's ionosphere is an ionized layer of the upper atmosphere situated between 60–2000 km in altitude. Below the ionosphere, there lies a neutral atmosphere. The top of the ionosphere gradually merges into the plasmasphere. The ionosphere consists of a weakly ionized plasma. The density of neutral particles in the ionosphere below 500 km is several orders of magnitude higher than the density of the ions and free electrons, but it is the ionized part of the plasma that defines the conductivity of the ionosphere and most importantly affects the propagation of the radio waves. We concentrate on the effects of the ionosphere on ELF waves, but the ionosphere also

has important effects on the higher frequency radio waves, including GPS signals at several gigahertz frequency.

Typical plasma density distributions in the ionosphere are presented in Figure 1.2 using the IRI model (discussed below) for the region of interest in this work. Usually plasmas are quasi-neutral, which means that the number of electrons is approximately equal to the sum of the number of ions at every location. Electrons produce stronger effects on waves above 100 Hz because they have higher mobility than ions. To first order, the electron density (N_e) profile with a clear maximum is formed by the interplay of two factors. First is the density of the neutral particles that decreases exponentially with increasing altitude. Second is the photoionization of the neutral particles by the sun that is stronger at the top of the ionosphere. At low altitudes there are many neutral particles to ionize, but the photoionization is low. At high altitude the flux of photons is high, but the neutral density is low. That is why there is an altitude at which the two factors are optimum and the maximum of electron density is formed therein. Also, the absence of photoionization in the night explains the lower plasma density as it is seen in Figure 1.2. The plasma density at night is maintained by the drainage from the overlying region, the ionization by cosmic rays and low recombination rates of some ions.

Usually, three major layers or regions are distinguished in the ionosphere [*Davies*, 1990, Ch. 1]: the D region (below 90 km), the E region (between 90 and 140 km), and the F region (above 140 km). The F region is further subdived into F_1 and F_2 layers, with the peak of the ionospheric density located in the F_2 layer. For the present work, the D and F_2 regions are of primary interest. The lowest ionosphere, the D region, is important because the high collision frequencies between charged and neutral particles make the highest contribution among all layers to the absorption of HF and ELF waves. The absorption is lower during the night when the plasma density is lower. The F_2 region is important for us because it contains the maximum electron density and the satellite observations that are the subject of this dissertation are made inside this region at the altitude of 670 km. Each layer can be characterized by its critical frequency or the frequency at which an electromagnetic wave just penetrates a given ionospheric layer. Signals at lower frequencies are reflected from the layer while
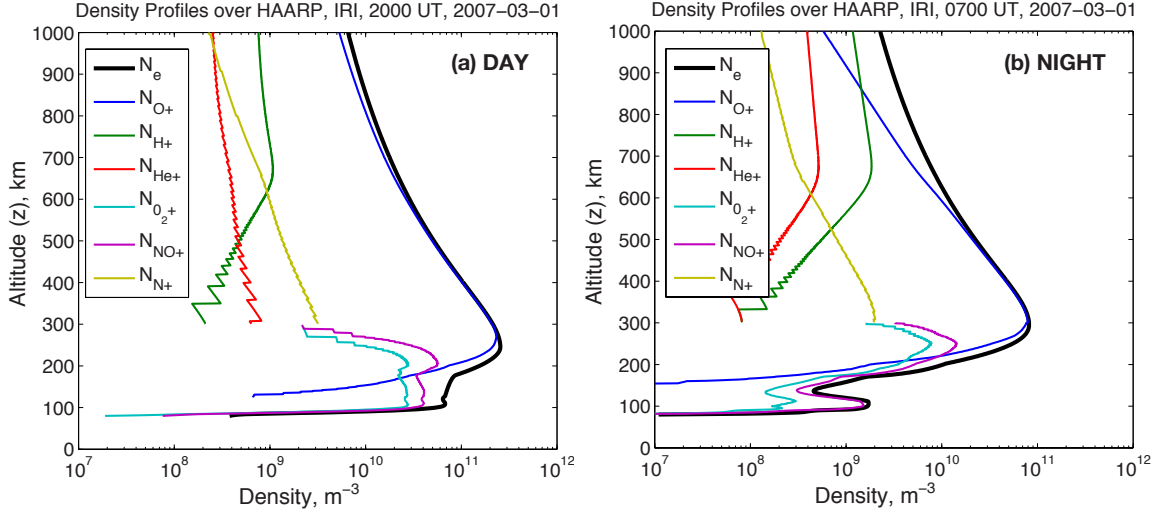
Figure 1.2: Typical profiles of electron and ion densities in Alaska for daytime (a) and nighttime (b) conditions. The data are from International Reference Ionosphere (IRI-2007) model. The electron density in the daytime can be from two to ten times higher than in the nighttime.

those at higher frequencies pass through it. To the first order, the critical frequency is defined by the maximum electron plasma frequency in the layer. The electron plasma frequency is given by the relation $\omega_0 = |q_e| \left(N_e/\epsilon_0 m_e\right)^{1/2}$, where q_e and m_e are correspondingly the charge and the mass of electrons. One of the most important ionospheric parameters is the critical frequency of the F_2 layer (usually labeled $f_0 F2$), because this layer has maximum electron density and maximum critical frequency. As a rule of thumb, $f_o F2 \propto (N_{e,\max})^{1/2}$, where $N_{e,\max}$ is the maximum electron density in the ionosphere.

One of the most common techniques to measure the electron density profile uses the reflection of the radio waves from the ionosphere. This technique is implemented in a device called the ionosonde [*Bibl and Reinisch*, 1978]. An ionosonde is a sweep-frequency pulsed radar which measures time delay at each frequency. From time delay it is possible to deduce the altitude of the layer from which a specific frequency is reflected, and from the value of the reflected frequency the electron density of the layer is deduced. The International Reference Ionosphere (IRI) model [*Bilitza and*

Reinisch, 2008] is an empirical model built from the measurements of ionospheric plasma density in multiple locations throughout the globe by several techniques including ionosondes. IRI describes monthly averages of ionospheric densities and temperatures in the altitude range 50-1500 km. For Figure 1.2 we use one of the latest versions of this model, IRI-2007.

The layers only approximately describe the structure of the ionosphere. In reality the ionosphere is a highly dynamic and irregular medium. It consistently contains transient and laterally inhomogeneous structures. These variations include dense slabs of ionization on scales of tens to hundreds of kilometers known either as sporadic E or spread F, depending on the altitude [*Calvert and Warnock*, 1969] as well as also much smaller, even meter scale, density irregularities [*Dyson*, 1969; *Gross and Muldrew*, 1984; *Pfaff et al.*, 2008]. Such irregularities make the analysis and prediction of wave propagation harder and lead to multiple phenomena some of which are discussed in this work. The dynamics of the ionosphere varies substantially with latitude. In our work we deal with the high-latitude ionosphere. The high-latitude ionosphere is greatly influenced by the magnetosphere and the solar wind, connecting to the ionosphere through the Earth's magnetic field. In the F region the ion-neutral collision frequency is small relative to the gyrofrequency, and therefore the plasma moves with the magnetic field lines rather than with the neutral wind as in the lower ionosphere. The speed of plasma flow is typically several hundred m·s^{-1} in high-latitude flow pattern [*Hunsucker and Hargreaves*, 2003, Ch. 5]. The main ionospheric trough [*Rodger et al.*, 1992], a region of depleted ionization, has its own pattern of behavior and is discussed in detail in Chapter 3.

Another important property of the ionosphere, and especially the high-latitude auroral ionosphere, is the ability to support a massive current system. The auroral electrojet is an intense, horizontally directed current that flows along the auroral oval in the D and E regions of the high-latitude ionosphere (Figure 1.3). The conductivity and the horizontal electric field in the auroral ionosphere are both generally higher then in the lower-latitude ionosphere, and this is why the auroral electrojet current can vary from a few thousand amperes to nearly 1.8 million amperes [*Kamide et al.*, 1982]. During its strongest period over Alaska in the nighttime, the auroral electrojet

is mostly a westward current with a maximum at 100 km altitude [*Kamide and Brekke*, 1993]. The electric field $\mathbf{E}_0$ of the auroral electrojet is supported by the magnetic field aligned currents from and to the magnetosphere [*Tascione*, 2010]. A few hours before midnight, the direction of the electrojet electric field changes from northward to southward. The directions of the electric field and the electrojet current are not parallel because the plasma medium is anisotropic due to the presence of $\mathbf{B}_0$ and is characterized by the conductivity tensor $\widehat{\sigma}$. The strength of the electric field is about 25 mV·m^{-1} on average [*Stubbe and Kopka*, 1977]. The strength of the auroral electrojet current is often experimentally measured by magnetometers on the ground and is characterized by a magnetic index AE measured in nanoteslas [*Davis and Sugiura*, 1966]. Excursions in the AE index from a nominal daily baseline are associated with magnetospheric substorms which may have durations of tens of minutes to several hours. In our work the auroral electrojet is modified by HF heating in order to generate ELF waves. It should be noted that there also exists an equatorial electrojet current in which ELF waves can also be successfully generated via HF heating [*Ferraro et al.*, 1982, 1984; *Stubbe et al.*, 1982].

1.3 The Magnetosphere and the Plasmasphere

At the altitude of about 2000 km the ionospheric plasma smoothly turns into the magnetospheric plasma which consists predominantly of electrons and protons. As seen from Figure 1.2, heavy ions tend to stay at lower altitudes because of the Earth's gravitational field. In the magnetosphere, the dynamics of the charged particles is strongly governed by the Earth's magnetic field. The outer shape of the magnetosphere is determined by the interaction of the Earth's magnetic field, the solar wind plasma, and the interplanetary magnetic field. The magnetosphere extends up to $10R_E$ on the sunward side and can stretch beyond $60R_E$ in the night side. The part of the magnetosphere in which the population of cold plasma with energies of ~ 1 eV and densities in the range from 10^7 to 10^{10} m^{-3} is called the plasmasphere. The bulk of the cold plasma in the plasmasphere mostly corotates with the Earth. The outer boundary of the plasmasphere, the plasmapause, is located between $L = 3$–6

FIELD ALIGNED
CURRENTS

AURORAL
ELECTROJET

FIELD ALIGNED
CURRENTS COUPLED
TO MAGNETOSPHERE

MIDLATITUDE
CURRENTS

EQUATORIAL
ELECTROJET

AURORAL OVAL

SOLAR RADIATION
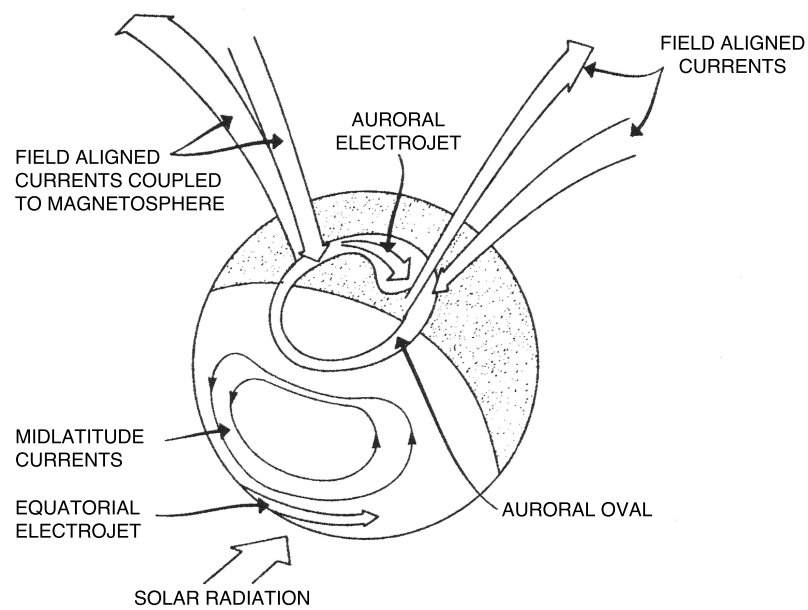
Figure 1.3: The configuration of the major current systems in the Earth's ionosphere. In this work we are concerned with the auroral electrojet current that exists in the high-latitude region of the ionosphere. The auroral electrojet is supported by the magnetic field aligned currents from and to the magnetosphere. Adopted from *Space Science Board* [1978].

(Figure 1.4) and was discovered by *D.L. Carpenter* through the analysis of ground observations of very low frequency (VLF) waves [*Carpenter*, 1963]. The plasmapause is characterized by the drop of plasma density by at least a factor of five over less than $0.5L$ [*Carpenter and Anderson*, 1992]. Such a density gradient can serve as a guiding structure for ELF waves [*Inan and Bell*, 1977]. The location of the plasmapause depends on the degree of magnetospheric activity [*Spasojevic*, 2003]. Following geomagnetic disturbances in the magnetosphere caused by activity of the sun, the plasmapause shrinks. Global geomagnetic activity in the magnetosphere is often indicated by the K_p indices [*Bartels et al.*, 1939]. The planetary K_p index is calculated every three hours from measurements at 12 magnetic stations throughout the globe. The scale varies from 0 to 9 and is logarithmically proportional to magnetic field variations. The geomagnetic conditions with K_p below 4 are considered non-disturbed. It has been determined empirically [*Moldwin et al.*, 2002] that the L-shell of the plasmapause L_{pp} can be represented as a function of K_p: $L_{pp} = 5.6 - 0.46K_{p,\max}$, where $K_{p,\max}$ is the maximum K_p observed in the previous 24 hours.

Besides a dense population of cold low-energy plasma in the plasmasphere, there is a population of much less dense (below 10^6 m^{-3}) but much more energetic particles called the radiation belts or Van Allen belts. The energy of particles in the radiation belts ranges from several keV up to as high as 10 MeV for electrons and 500 MeV for protons. These energetic particles (red curves in Figure 1.4) execute three periodic motions in the the Earth's magnetic field in accordance with their three adiabatic invariants [*Landau and Lifshitz*, 1976, Ch. 7] [*Walt*, 2005, Ch. 4]. First, they quickly gyrorotate around magnetic field lines with gyrofrequency ω_c. Second, they bounce back and forth between conjugate hemispheres. Third, they slowly drift azimuthally around the Earth as a result of the gradient and curvature magnetic drifts.

1.4   Basics of Wave Generation and Propagation

In this work we deal primarily with Extremely Low Frequency (ELF) waves and secondarily with High Frequency (HF) waves as a means of generation of ELF waves. The HF designation commonly refers to frequencies between 3–30 MHz. The ELF
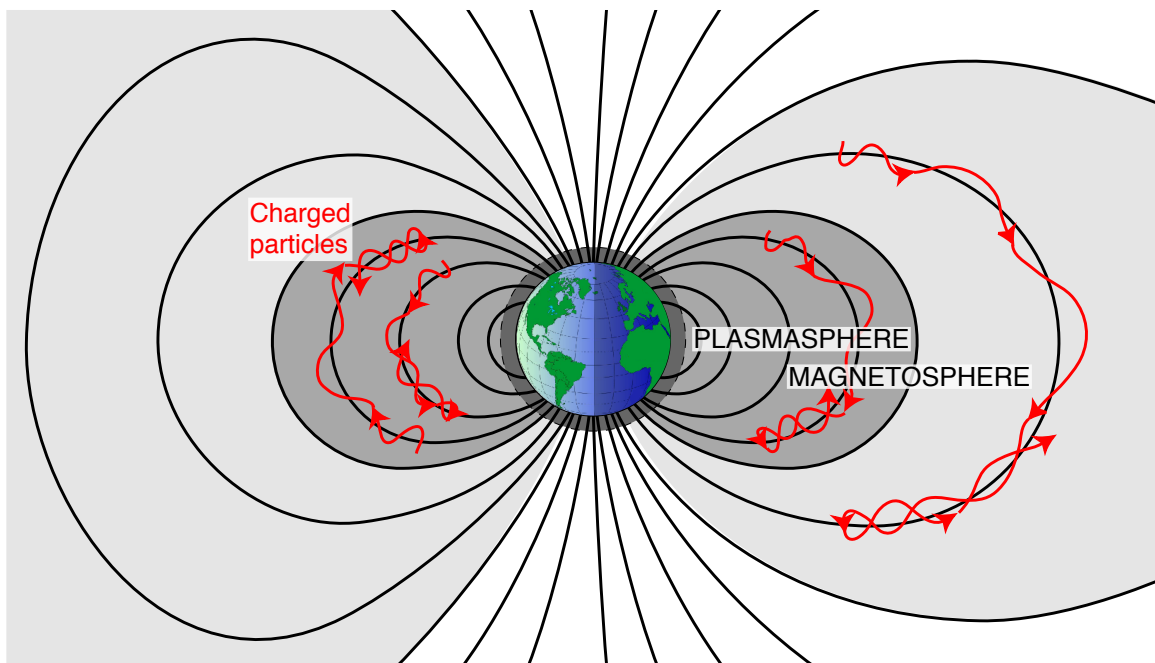
Figure 1.4: Schematic configuration of the Earth's magnetosphere and plasmasphere. The relative density of cold plasma in each region is approximately represented by gray color. Adopted from *Inan* [1977] and *Gibby* [2008].

designation can vary in the literature depending on the field of study, but here by ELF we mean the frequencies between 30–3000 Hz. This range is closely related to the adjacent Very Low Frequency (VLF) band of 3–30 kHz. ELF and HF waves can propagate both in the neutral atmosphere and in space plasmas. The propagation of these waves in the neutral atmosphere obeys the laws of propagation similar to those in free space and is in the form of broadly-used transverse electromagnetic waves. We only briefly cover this type of propagation here when we discuss the propagation in the Earth-ionosphere waveguide. On the other hand, the propagation of ELF and HF waves in space plasmas is a complicated subject to which much research and literature (including more than a half of the bibliography in this work) is devoted. Here we only briefly introduce several concepts of propagation in space plasmas in order to facilitate understanding of the rest of the dissertation.

1.4.1   ELF Waves in Free Space and their Applications

The primary source of ELF/VLF waves in the Earth's atmosphere is a lightning discharge. A lightning discharge produces a current that acts like a vertical antenna of 5–7 km length, radiating at all frequencies from a few Hz [*Burke and Jones*, 1992] through to the optical band [*Weidman and Krider*, 1986]. There is a peak in the radiated spectrum in the VLF band, from a few kHz to about 30 kHz [*Uman*, 2001, Ch. 7]. An ELF/VLF wave packet generated by a lightning discharge propagates in the Earth-ionosphere waveguide with a group velocity close to the speed of light and its form as received by ground receivers was historically called a radio atmospheric or a sferic. In a frequency-time spectrogram with duration of more than several seconds, a sferic is represented as a straight vertical line in ELF range, demonstrating that various frequencies in this range arrive with the same time delay.

ELF waves can propagate over long distances because the Earth and the lower ionosphere form a parallel-plate waveguide with boundaries that are close to perfect conductors in the ELF range. *Wait* [1965] developed a simple model of such a waveguide with lossy walls. Energy is mostly lost during the propagation through the finitely conducting ionosphere. In the first approximation, the curvature of the

Earth and the finite conductivities of the boundaries can be neglected. In such an approximation, the classical theory of parallel-plate waveguide can be applied [*Inan and Inan*, 2000, Ch. 4]. If the height of waveguide h is assumed to be 80 km (in reality 70 to 90 km), we can calculate that the lowest TE and TM modes will have a lower cutoff frequency $f_{\text{cut}} = c/(2h) = 1875$ Hz. Also, there exists one TEM mode without a cutoff frequency. For frequencies above the lowest cutoff, the TEM mode and several TE/TM modes are important. The TE modes can have lower attenuation than the TEM mode and can constitute the main contribution to the propagation of wave energy over long distances. Below the lowest cutoff frequency, the TEM mode is important, while all other modes are evanescent and almost undetectable at distances in excess of 1000 km. The discussion above is only a very simplistic model; in reality we use a much more complete full-wave model to describe all deviations from the ideal parallel-plate waveguide.

The possibility of ELF/VLF wave propagation over long distances (5–20 megameters) with low attenuation (from 0.6 dB/Mm at 30 Hz to 10 dB/Mm at 5 kHz [*Bernstein et al.*, 1974; *Said*, 2009]) gives rise to several important applications. Lightning flashes can be detected and located with at least 4 km accuracy using the reception of ELF/VLF waves by ground receivers [*Said*, 2009]. Also the strength of the current, the timing and other characteristics of the lightning discharge can be determined [*Reising et al.*, 1996; *Cummer and Inan*, 1997; *Inan et al.*, 2006]. In addition, ELF/VLF waves can be used for the diagnostic of D region of the ionosphere [*Cummer et al.*, 1998].

In the process of wave propagation in the Earth-ionosphere waveguide, part of the ELF/VLF energy leaks not only upward through the ionosphere, but also downward through seawater and earth. A plane wave propagating downward in the seawater is created, and this is why ELF/VLF waves can be used for communication with submarines. The seawater can be approximated as a good, but lossy, conductor with conductivity $\sigma \simeq 4$ Sm·m^{-1} in ELF/VLF range. The efficiency of wave penetration into a good conductor is determined by the skin depth $\delta = (\pi f \mu \sigma)^{-1/2}$. In seawater it can be from several meters to several tens of meters in ELF/VLF frequency range. ELF/VLF waves can also be used in geophysical prospecting for underground imaging

[*McNeill and Labson*, 1991]. For dry earth $\sigma \approx 10^{-4}$ Sm·m^{-1} and the skin depth can be hundreds of meters.

The decrease of attenuation with decrease of the frequency in the waveguide and in the water calls for the usage of the lower part of the spectrum for submarine communication. However, there are two factors which limit the communication at lower frequencies. First, the available bandwidth decreases. Second, with the decrease of frequency it becomes more difficult to generate waves efficiently. The second factor limits not only applications in communications, but all other applications as well.

The wavelength in free space, λ_0, in the ELF/VLF bands ranges from 10 to 10,000 km. Any practically realizable antenna for these wavelength would be in the form of an electrically short dipole for which the antenna length $L \ll \lambda_0$. For short dipoles, the radiated power $P \propto (L/\lambda_0)^2$ [*Stutzman and Thiele*, 1998, Ch. 3], so that the antenna efficiency decreases with the increase of the wavelength. There are also two additional limitations. First, the maximum antenna efficiency is achievable only over a small bandwidth, which limits the rate of communication. Second, as it was mentioned before, the ground is conductive in the ELF/VLF range, and an image current is created in the Earth if the antenna is positioned horizontally. The less the separation between the current in the antenna and the image current in comparison to the wavelength, the bigger the part of the radiation that is canceled by the image current. The total power of the transmitter cannot be increased infinitely not only because of economical reasons, but also because of the electrical breakdown in the atmosphere.

Despite many difficulties, several types of antenna systems have been built for operation in the ELF and VLF frequency ranges (review by *Barr et al.* [2000]). Currently, there are several systems with vertical monopole antennas of about 500 m long that operate in 18–24 kHz frequency range. Even though frequencies around 20 kHz would not penetrate much deeper than about 10 m into seawater, these systems are currently the only type which are reasonably efficient and operate regularly for communications with submarines. Such systems more efficiently inject waves into the waveguide rather than into the space, because the maximum antenna radiation is approximately perpendicular to a vertical antenna. In the past there was also a

U.S. Navy system in Clam Lake, Wisconsin capable of wave generation at 76 Hz. At this frequency, communication with deeply submerged submarines was possible at depth of about 100 m [*Navy Fact File*, 2001]. The transmitting antenna consisted of a horizontal 28 mile long transmission line located over a bedrock layer with lower conductivity for increased efficiency. Despite the increased efficiency, the antenna could only radiate on the order of 10 W [*Jones and Burke*, 1995].

The ELF transmission system with the closest frequencies to those emphasized in this work was operated by Stanford University at Siple Station, Antarctica ($L = 4.3$) from 1973 to 1988. Initially, the setup consisted of an 80 kW transmitter and a horizontal 21.2 km antenna with resonant frequency of approximately 5 kHz [*Helliwell and Katsufrakis*, 1974]. Later, the Siple facility was upgraded to a 150 kW transmitter and two 42 km long antennas arranged in a crossed dipole geometry, leading to a resonant frequency of 2.5 kHz and an estimated radiated power of 1.5 kW [*Carpenter and Bao*, 1983; *Gibby*, 2008]. The radiation efficiency was relatively high for these frequencies and reached 1–3% [*Raghuram et al.*, 1974]. This efficiency was achieved via the separation of the horizontal antenna from the conducting ground plane by a 2 km thick ice sheet. The purpose of Siple facility was the injection of ELF waves into the magnetosphere and the study of ELF waves and their effects in the magnetospheric plasma. The waves in plasma and their effects are considered in the next section.

1.4.2 Electromagnetic Waves in Plasma and their Applications

The propagation of electromagnetic waves in plasma is a vast subject with many different approaches and applications [*Stix*, 1992; *Davies*, 1990; *Budden*, 1985]. Here we briefly mention important features relevant to waves that are usually described within the magneto-ionic framework [*Alpert et al.*, 1953; *Ratcliffe*, 1959]. The most important difference from free space is the presence of charged particles in a plasma that are coupled to electromagnetic waves through the Lorentz force. Because of the Lorentz force, the Earth's magnetic field also becomes important in wave propagation and makes the medium anisotropic. The Lorentz force (equation 1.4a), two Maxwell's

equations (1.4b,c), and the definition of the current (1.4d) constitute the complete set of equations from which the wave equation in plasmas can be derived with appropriate approximations.

$$m\frac{d\mathbf{v}}{dt} = q\mathbf{E} + q\mathbf{v} \times \mathbf{B}, \tag{1.4a}$$

$$\nabla \times \mathbf{E} = -\frac{\partial \mathbf{B}}{\partial t}, \tag{1.4b}$$

$$\nabla \times \mathbf{B} = \mu_0 \mathbf{J} + \mu_0 \epsilon_0 \frac{\partial \mathbf{E}}{\partial t}, \tag{1.4c}$$

$$\mathbf{J} = \sum_i q_i N_i \mathbf{v}_i. \tag{1.4d}$$

The refractive index of ELF waves can be derived with several assumptions. First, the medium is considered homogeneous and the Earth's magnetic field is assumed to be much larger then the wave magnetic field. Other perturbations are also considered to be small, and as a result the equations can be linearized. The effect of the thermal motion of the particles is neglected in magneto-ionic theory, and the plasma is considered cold. This assumption is generally a good approximation in the ionosphere and the magnetosphere because the density of cold plasma is usually much larger than the density of energetic particles. With this approximation, the refractive index is given by the Appleton-Hartree equation [*Appleton*, 1932]:

$$n^2 = 1 - \frac{X(U-X)}{U(U-X) - \frac{1}{2}Y^2 \sin^2\Theta \pm [\frac{1}{4}Y^4 \sin^4\Theta + Y^2 \cos^2\Theta(U-X)^2]^{\frac{1}{2}}}, \tag{1.5a}$$

$$X = \frac{\omega_0^2}{\omega}, Y = \frac{\omega_c}{\omega}, U = 1 - i\frac{\nu}{\omega}, \tag{1.5b}$$

where i is the imaginary unit; Θ is an angle between the wave vector $\mathbf{k}$ and the Earth's magnetic field $\mathbf{B}_0$ (the dependence on $\mathbf{k}$ can be explicitly expressed with the next substitution $\cos\Theta = \mathbf{k} \cdot \mathbf{B}_0/(|\mathbf{k}| |\mathbf{B}_0|)$); ω is wave frequency; ω_0, ω_c, ν are correspondingly plasma, cyclotron and collision frequencies. The imaginary part of

the refractive index determines the wave attenuation. Equation 1.5 describes ordinary (plus sign) and extraordinary (minus sign) modes at different frequencies. For wave frequencies $\omega < \omega_c$ and $\omega \ll \omega_0$ and small Θ, the ordinary mode is called the whistler mode. In the Earth's plasma, the frequency of whistler mode waves intersects with the audible range and can be detected by standard radio receivers. The ELF/VLF waves in plasma that we consider in this work propagate in the whistler mode. In the first approximation in a collisionless plasma when Θ is small (longitudinal approximation), the refractive index for whistler mode waves is given by

$$n^2 = 1 - \frac{\omega_0^2}{\omega(\omega - \omega_c \cos\Theta)}. \tag{1.6}$$

If there were no magnetic field in the plasma so that $\omega_c = 0$, then n^2 would be less than zero in the equation (1.6) at $\omega < \omega_0$. This means that whistler mode cannot exist without a magnetic field since all waves in a plasma below the plasma frequency would decay in such a situation.

The typical value of refractive index in the ionosphere is around 30 for a 1 kHz wave. Applying Snell's Law, it can be deduced that the wave vector in the ionosphere is essentially vertical for a wide range of incident angles of waves propagating from below. It also can be shown that the direction of the electromagnetic energy flow of whistler mode waves is confined to a narrow semi-angle less than 19° from $\mathbf{B}_0$, leading to the dominant propagation direction being along the Earth's magnetic field lines [*Davies*, 1990]. From the expression for the refractive index, it is seen that whistler waves are dispersive. It can be shown that as it propagates along the magnetic field line, the time delay T of a wave packet is: $T \propto \omega^{-1/2}$.

Whistler waves are elliptically polarized. For waves propagating along $\mathbf{B}_0$, the wave electric field rotates in a right hand sense with the frequency of the wave ω. With the same sense, the electrons gyrate around $\mathbf{B}_0$ at the frequency ω_c. As a result, when $\omega = \omega_c$, there is a cyclotron resonance between whistler waves and cold plasma electrons at frequency $\omega = \omega_c$ when $\cos\Theta \to 1$. The resonance is also seen from equation (1.6). However, there is another important type of cyclotron resonance not included in the equation (1.6). It is the resonance between whistler

waves and energetic electrons (that is why it is not included when the plasma is treated as cold) and occurs when the doppler-shifted wave frequency as seen by an energetic electron is equal to electron gyrofrequency [*Inan*, 1977]: $\omega + kv_\parallel \simeq \omega_c$, where k is the wave number and $v_\parallel$ is the component of the electron velocity along the magnetic field. In this resonance, the electrons also rotate synchronously with the whistler wave electric field, so that they experience a constant electric field that can accelerate or decelerate them continuously. The energy can be transfered from electrons to whistler waves and vice versa. This transfer leads to an effective wave-particle interaction between energetic electrons from the Earth's radiation belts and whistler waves. There are several important manifestations (or applications) of wave-particle interactions such as ELF/VLF triggered emissions [*Gibby*, 2008] and energetic electron precipitation [*Inan et al.*, 2007; *Peter*, 2007; *Cotts*, 2011]. As a component of the triggered emission process, the energy is transferred from electrons to waves, and as a result the waves are amplified. In precipitation, the electron trajectory is modified by whistler waves, causing the electrons to penetrate to the lower atmosphere as they bounce between conjugate ionospheres while traveling along the Earth's magnetic field lines. The penetration to the lower atmosphere leads to a higher probability of an electron-neutral collision, and as a result the electrons are deposited in the atmosphere or "precipitate". In this process, ELF/VLF waves can potentially be employed to remove energetic particles, which are damaging to communication satellites, from the Earth's radiation belts. The electron precipitation by ELF/VLF waves generated via lightning discharges is also an important fundamental process that partially controls the population of the Earth's radiation belts [*Abel and Thorne*, 1998a,b].

The absorption of plasma waves is described by the imaginary part of the refractive index (1.5). If the mode is not evanescent, then the non-zero imaginary part arises from a finite collision frequency ν. Different types of collisions may be dominant in different regions. Most of the absorption in the ionosphere occurs in the lower part between 70 and 120 km as the result of collisions between electrons and neutrals. In the F region, coulomb collisions between electrons and charged particles are dominant [*Helliwell*, 1965]. The absorption coefficient α in a homogeneous medium is related to the imaginary part of n as:

$$\alpha = \text{Im}(n)\frac{\omega}{c}. \tag{1.7}$$

In the simplest approximation for a longitudinally propagating whistler mode wave in the ionosphere, expression (1.7) can be written as [*Helliwell*, 1965]:

$$\alpha = \frac{\omega_0 \nu}{2c\left|\omega_c \cos\Theta\right|^{3/2}}\sqrt{\omega}. \tag{1.8}$$

This equation approximately demonstrates how absorption depends on wave and collision frequencies. The total absorption through a layer can be obtained by the integration of α at every altitude. The results of the integration depend strongly on the assumed parameters of the ionospheric densities and generally can vary substantially depending on the time of day, location, and geomagnetic conditions. In the numerical integration the imaginary part of the refractive index can be obtained from the full Appleton-Hartree expression (1.5). The curves from *Helliwell* [1965] present an estimation of the total absorption for several typical models of the ionosphere (Figure 1.5). The absorption is calculated separately for the lower (60 to 200 km) and the upper (200 to 1500 km) ionosphere. The total absorption is the sum of the two absorptions. It should be noted that the reflection from the bottom ionosphere is not taken into account in the Helliwell curves and about 4 dB should be added to the total absorption in ELF/VLF range if the signal enters from the neutral atmosphere [personal communication with *N.Lehtinen*].

As was mentioned above, the plasma in the ionosphere and magnetosphere is not homogeneous. The refractive index for the whistler mode can only approximately describe the behavior of ELF waves in these regions. In current practice, the refractive index is used in more complete numerical models in which media are only locally treated as homogeneous. Such models are described in Chapter 2. There are usually no obstacles to use the complete Appleton-Hartree expression (1.5) in numerical simulations. The approximate version (1.6) is mainly used for simplified interpretations of the results.
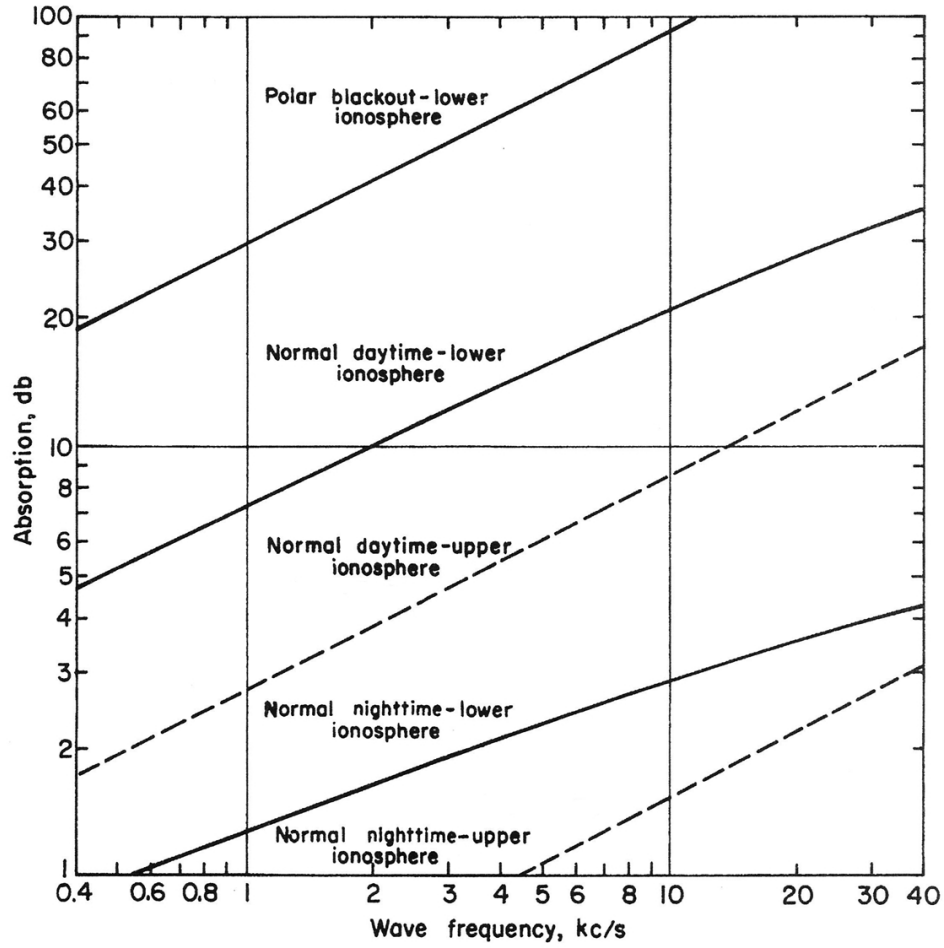
Figure 1.5: Integrated absorption as a function of wave frequency (kc/s $\equiv$ kHz) for different models of the upper and lower ionosphere: normal daytime f_0F2 = 12.5 MHz; normal nighttime f_0F2 = 5.5 MHz. $f_c \cos\Theta \equiv (\omega_c/2\pi)\cos\Theta = 1.1$ MHz. Adopted from *Helliwell* [1965].

1.5 ELF Waves via HF Ionospheric Heating

1.5.1 The Concept

As mentioned in Section 1.4.1, the generation of ELF/VLF waves presents a big challenge due to the enormous size of the required antenna and antenna separation from the ground in case of its horizontal placement. Except for the case of Siple transmitter in Antarctica, all attempts of generating ELF waves have proved to be highly inefficient. An alternative method of ELF/VLF wave generation via HF ionospheric heating has been investigated since the 1970's [*Getmantsev et al.*, 1974; *Stubbe and Kopka*, 1977; *Kapustin et al.*, 1977; *Dowden et al.*, 1981; *Ferraro et al.*, 1984]. The concept of HF heating is shown schematically in Figure 1.6.
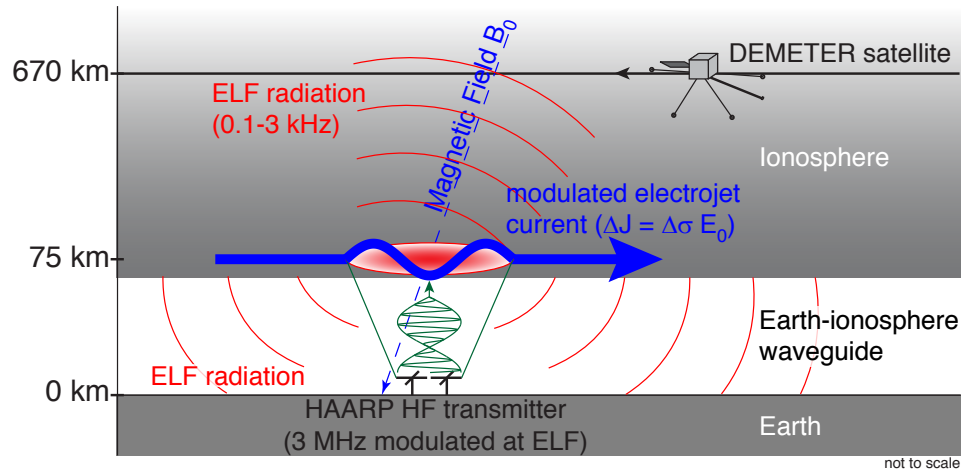
Figure 1.6: ELF wave generation via HF ionospheric heating.

As described in Section 1.2, the ionosphere supports several major current systems, the most important of which are the auroral electrojet and midlatitude currents. The conductivity tensor $\hat{\sigma}$ of the ionospheric plasma depends on the electron collision frequency which in turn depends on electron temperature [*Kelley*, 2009, Ch. 2]. In this work we consider the heating of the D region in which electron-neutral collisions dominate, as was discussed above. The electron temperature can be efficiently

increased by HF waves [*Ginsburg*, 1960]. To the first approximation, the Appleton-Hartree expression (1.5) can be applied to the calculation of HF power absorbed in the ionospheric D region. However, a more rigid kinetic treatment of HF heating exists in which the modification of the Maxwellian electron energy distribution is taken into account [*Papadopoulos et al.*, 1990]. It is important that the increase and decrease of electron temperature due to HF power variation can happen fast enough, so that if HF carrier frequency is modulated with ELF frequency, the change in conductivity also occurs at ELF frequency [*Moore*, 2007]. This change, according to Ohm's Law, creates a current at ELF frequency $\Delta \mathbf{J}(\omega_{ELF}) = \Delta \widehat{\sigma}(\omega_{ELF}) \mathbf{E}_0$, where $\mathbf{E}_0$ is DC electric field of the electrojet current. Also, harmonics of the main ELF frequency are created due to the non-linearity of the HF heating process. HF waves used in heating have wavelength of about 100 m in free space and can be effectively generated and directed upward into the ionosphere by available techniques. The ELF current created in heating can be considered as a horizontal giant antenna in the D region of the ionosphere ($\sim$ 75 km altitude) where heating occurs most effectively. The antenna has approximately the size of the heated region and is separated from the conducting ground by a substantial part of the wavelength. Also, since the antenna is already immersed in the plasma, the generated wave can be effectively injected into the magnetosphere without reflection from the bottom ionospheric boundary. However, the immersion in the plasma media with complicated particle density and field distributions and the complex heating process make the radiation problem difficult to track analytically. The main purpose of this work is to describe the distribution of the generated ELF wave field and the propagation of ELF waves further from the source through experimental and simulation techniques.

1.5.2 Previous Work

Several important features of ELF field generation via HF heating have been learned in prior experiments. The majority of results were obtained through ground measurements, but several satellite experiments were also performed.

The first observations of ELF waves via HF heating were obtained by a group

of Russian scientists at Zimenki, Nizhny Novgorod region at a magnetic latitude of 51° (*Getmantsev et al.* [1974]; *Mironenko* [2000]; the first paper does not include the location of the experiment most likely due to the Cold War security). The HF transmitter operated at the frequency of 5.75 MHz and had a power of 150 kW. It was amplitude modulated at 1259, 1773, 2525, 4000, and 7246 Hz. All frequencies were registered by a ground receiver 180 km to the north from the transmitter. The strength of the electric field at 2525 Hz was twice higher than the next strongest frequency. The lack of strong ambient ionospheric currents over the region of the transmitter led to the overall weak ELF signal strength [*Belyaev et al.*, 1987].

The HF transmitter in Tromso, Norway (2.7–8.0 MHz, ∼1300 kW, a part of the European Incoherent Scatter (EISCAT) Association facility) has been operating in the auroral region for the generation of ELF waves since 1980 [*Stubbe et al.*, 1981]. The amplitude modulation in the range of 200 Hz to 6.5 kHz have been used to produce ELF/VLF waves. On the ground, the magnetic field of ELF waves was detected with strengths of 1, 0.1, and 0.03 pT at distances of 20, 200, and 500 km respectively [*Stubbe et al.*, 1982; *Barr et al.*, 1985]. The signal on the ground was detected as far away as 2000 km with the magnitude of about 10 fT [*Barr et al.*, 1991]. The observed ELF/VLF fields exhibited maxima in frequency near multiples of 2 kHz at distances of less than 100 km [*Stubbe et al.*, 1982]. These peaks were shown to be the result of vertical resonances in the Earth-ionosphere waveguide [*Stubbe et al.*, 1982; *Barr and Stubbe*, 1984]. The strength of ELF/VLF waves generated using X-mode HF polarization was typically more than 3 dB higher in amplitude than those generated using O-mode HF polarization, as measured both on the ground [*Stubbe et al.*, 1982; *Barr et al.*, 1999] and in space [*James et al.*, 1984]. The variations in ELF/VLF signal amplitude on time scales of hours and days have shown correlation with geomagnetic activity measured by the K_p index [*Barr et al.*, 1985]. The observations in space over Tromso are discussed below. The ELF/VLF waves were detected only in overhead passes. It is most likely the location of the transmitter at $L = 6.2$ that caused ELF waves to propagate mostly at open magnetic field lines and outside the plasmasphere and resulted in the lack of detection of whistler mode echoes. Nevertheless, the vast experience of EISCAT facility operation substantially helped in the planning of future

heating experiments for space observations.

The High Power Auroral Stimulation (HIPAS) facility, near Fairbanks, Alaska, was used in a number of experiments to modulate the auroral electrojet for generation of ELF/VLF waves [*McCarrick et al.*, 1990]. The HIPAS facility was operating at 2.85 and 4.53 MHz with 800 kW of power. Experiments with three different modulation techniques (amplitude modulation, phase modulation, and beat-frequency modulation) were performed. It was found that amplitude modulation produced the strongest ELF fields [*Villasenor et al.*, 1996].

The most modern HF heating facility, the High Frequency Active Auroral Research Program (HAARP), is located in Gakona, Alaska. The HAARP HF antenna array was built in three stages which were completed in 1998, 2003 and 2007. This facility is the one which is used in the current work, and its detailed specifications are given in Section 2.3.1. *Milikh et al.* [1999] made the first experiments with modulated heating at the very early construction stage, which produced only 10 MW of power. Also *Milikh et al.* [1999] were the first to utilize two nearby HF heating facilities, with simultaneous detection of ELF/VLF signals from HAARP and HIPAS HF heating. Subsequently, HAARP was used to demonstrate the transmission of ELF waves up to distances of 4400 km on the ground [*Moore et al.*, 2007] and into space [*Platino et al.*, 2004; *Platino et al.*, 2006]. A new method of ELF modulation, geometric modulation, have been developed using HAARP [*Cohen et al.*, 2008; *Cohen*, 2009]. The magnetosperic injection of ELF waves with HAARP has produced the first examples of detectable wave-particle interactions initiated by ELF/VLF waves from modulated HF heating [*Inan et al.*, 2004; *Golkowski et al.*, 2008]. *Golkowski et al.* [2009] also report cross modulation between the signals returning to the HAARP region after reflection from the conjugate region and simultaneous HF transmissions.

1.5.3 Previous Satellite Observations

Previously, satellite experiments that successfully detected ELF waves from HF ionospheric heater existed only over the heating region and in the magnetosphere, but not over the conjugate region. Below we review the most import features of these

observations.

The measurements of HF-heating generated ELF signals include those at low alti-
tudes observing signals propagating from the source to the satellite without reflection
from the ground [*James et al.*, 1984] and those at laterally distant locations–involving
propagation in the Earth-ionosphere waveguide and continuous penetration through
the ionosphere upward to higher altitudes [*Platino et al.*, 2006]. However, until the
experiments described in Chapters 2–5, there existed relatively few spacecraft ob-
servations of ELF waves generated via HF heating, and many unknowns remained.
One important parameter concerns the amount of ELF power propagating upward
from the heated region. In the work of *James et al.* [1984] at the Tromso facility, the
E-field measured aboard the ISIS 1 spacecraft at ~1200 km altitude was sustained
at the level of 200 μV·m^{-1} for 525 Hz, 1575 Hz and 1725 Hz in the close region of
$d \leq 50$ km (where d is the lateral distance at the altitude of the source between the
magnetic footprint of the satellite at this altitude and the center of the source). The
field magnitude even reached the value of 2.6 mV·m^{-1} for 525 Hz at one data point,
which was disregarded by the authors as a possible measurement anomaly. The ef-
fective source currents deduced from ISIS data were one to two orders of magnitude
larger than currents calculated from ground-based measurements for the same event.
The authors did not take into account the directional injection of ELF waves into the
space by a column of the radiation discussed in this work. In the work of *Kimura
et al.* [1991] at the HIPAS facility, the results of *James et al.* [1984] were questioned.
Measurements on the Akebono satellite over HIPAS [*Kimura et al.*, 1991] showed
maximum fields of $E \simeq 15$ μV·m^{-1} and $B \simeq 0.25$ pT for 2.5 kHz signal. Maximum
fields in Akebono measurements over the Tromso HF heater [*Kimura et al.*, 1994]
were found to be $E \simeq 4$ μV·m^{-1} and $B \simeq 2$ pT at 2.5 kHz. For these fields in
space lower than those from the ISIS 1 measurements, the effective source currents
were calculated to be consistent with ground observations. This consistency may be
explained with a simple model because the satellite most likely did not pass directly
over the narrow column of radiation as it probably happened in ISIS 1 measurements,
and as we demonstrate in this work with DEMETER measurements.

1.6 Thesis Organization

The present work is organized into 8 chapters.

In Chapter 1, the current chapter, we introduce the reader to the general concepts used in this work, present the history and motivation of the research, and briefly describe the specific contributions.

In Chapter 2 we present the geometrical domain and logistics of the research. Also, the description of the scientific instruments and models used in the research is given.

In Chapter 3 we analyze the ionospheric plasma environment over HAARP and especially pay attention to an important feature of it–the main ionospheric trough.

In Chapter 4 we present DEMETER satellite observations and analysis of case studies over HAARP. This introduces the reader to the basic physical concepts of our research and gives examples of new observational results.

In Chapter 5 we conduct more rigorous analysis of the data using the aggregation of multiple cases and statistics. The hypotheses suggested in case studies are also confirmed here and several new patterns are revealed.

In Chapter 6 we use numerical models to interpret the results of observations. Many features are confirmed and interpreted with full-wave modeling, but some of the features can not be explained by this model. Then, ray tracing is used to interpret the discrepancies in observations and full-wave modeling.

In Chapter 7 we analyze DEMETER satellite observations in space over the HAARP conjugate region. With first observations in space over the conjugate region, several patterns are revealed and discussed.

In Chapter 8 we summarize the results of the research over the HAARP ionospheric heater and over its conjugate region. Also, possible future work is suggested here.

1.7 Scientific Contributions

The specific contributions of the present work can be summarized as follows:

1. Discovery of an intense column of ELF electromagnetic radiation generated via

HF ionospheric heating [*Piddyachiy et al.*, 2008]. The column is marked as Region 1 in Figure 1.7.

2. Identification of three distinct regions of ELF radiation generated via HF iono-spheric heating and their dependence on frequency and local time. The regions are shown schematically in Figure 1.7.

3. Interpretation of the shape and location of the column, as well as frequency and diurnal variations of the illuminated regions using full-wave modeling and ray tracing.

4. Assessment of the influence of the main ionospheric trough on ELF and HF waves and associated observations of ELF electrostatic turbulence [*Piddyachiy et al.*, 2011].

5. First satellite observations of one-hop and two-hop ELF waves generated via HF ionospheric heating. The observations of higher signals during the daytime and the displacement of the strongest signal toward the equator.
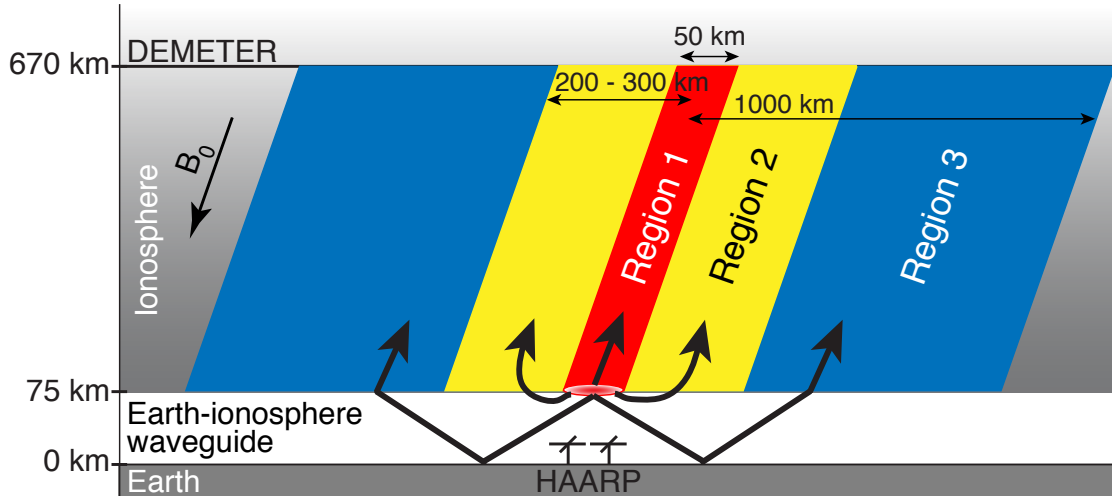
Figure 1.7: Schematic overview of ELF radiation regions.

Chapter 2

Problem Setup and Solution Techniques

2.1 Time and Coordinate Systems

The default global coordinate system used in this work is geographic (geocentric) coordinate system (GEO). For timing, Coordinated Universal Time (UTC) is used by default and is also abbreviated as UT for short in this work. Local time (LT) is used to specify the position relative to the Sun. The local time at each location is the difference between its longitude and the longitude of the sun converted to hours plus 12 hours:

$$\text{LT} = \frac{\text{longitude(observer)} - \text{longitude(sun)}}{15} + 12 \text{ h.} \tag{2.1}$$

LT is 12 (noon) if the observer faces the Sun, and LT is 24 (midnight) if the observer faces away from the sun. The Magnetic Local Time (MLT) is computed in the similar way, but the longitude in solar magnetic system (SM) is used instead of geographic longitude. For details on coordinate systems used in space physics see [*Kivelson and Russell*, 1995, Appendix A].

The Cartesian coordinate system (x, y, z) in Figure 2.1 is used by default throughout the work for presentation of results locally unless specified otherwise. The origin
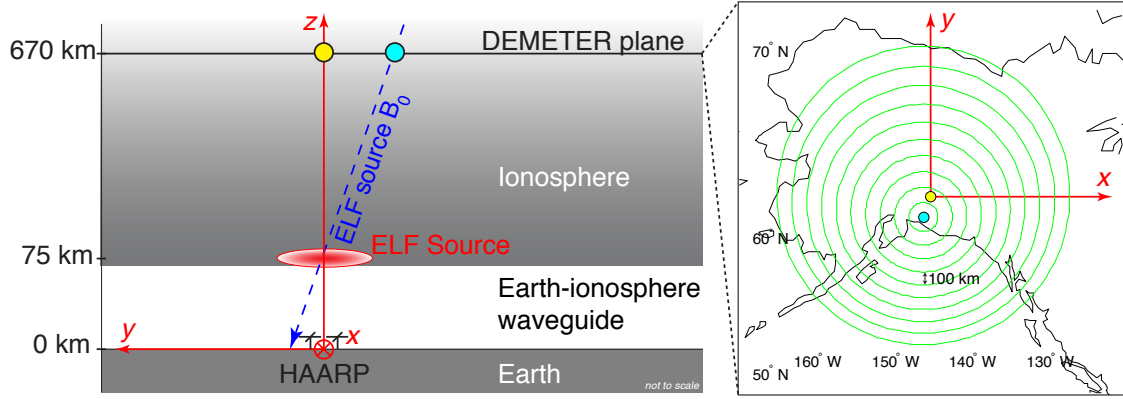
Figure 2.1: Coordinate system and reference parameters.

is placed at the location of HAARP. The z-axis is directed vertically up. The x-axis is along east-west direction pointing to the east, and the y-axis is along north-south direction pointing to the north. If the Earth's curvature is neglected, the xy planes are horizontal planes parallel to the ground and DEMETER observations are located within one of these planes referred to herein as the "DEMETER plane". The Earth's curvature can be neglected in many practical cases, such as done in one of the models we use in this work [*Lehtinen and Inan*, 2008]. This approximation is valid because the Earth's radius is much bigger than the domain size of the considered problem. Please note that Figure 2.1 is schematic and not to scale.

The DEMETER altitude changed throughout the course of our experiments in the range from 668 to 673 km, but these variations are negligible in comparison to absolute DEMETER altitude. As a reasonable approximation we assume DEMETER to always be at the altitude of 670 km. The point at which the vertical from HAARP intersects the DEMETER plane is marked by a yellow filled circle (Figure 2.1).

Another important reference is the Earth's magnetic field line that intersects the center of the ELF source region created by HAARP. We refer to it as "$\mathbf{B}_{0,\mathrm{source}}$" throughout the work. *Barr et al.* [1986] found by modeling that the ELF source is located at the altitude of 70–80 km. We assume it to be at 75 km. The point at which $\mathbf{B}_{0,\mathrm{source}}$ intersects the DEMETER plane is marked by a cyan filled circle. This point is at $x_{B_0} = -58$ km, $y_{B_0} = -153$ km, and $z_{B_0} = 670$ km in our coordinate system,

if the IGRF magnetic field model is used. For simplicity, $\mathbf{B}_{0,\text{source}}$ is presented as a straight line in Figure 2.1. Actually, if the Earth's magnetic field is approximated by straight lines, the location of this intersection is at $x_{B_0} = -52$ km, $y_{B_0} = -137$ km, $z_{B_0} = 670$ km. This approximation introduces a relatively small error which is well justified in practice.

On the right-hand side of Figure 2.1, the DEMETER plane with a geographical map underneath is shown. The same cyan and yellow reference points are also indicated. When DEMETER observations are discussed in this work, the intersection of the DEMETER plane with $\mathbf{B}_{0,\text{source}}$ is often used as a primary reference. The distance between this intersection point and the DEMETER satellite is equal to the horizontal distance between $\mathbf{B}_{0,\text{source}}$ and DEMETER. In this context we often call this distance, for simplicity, the distance from $\mathbf{B}_{0,\text{source}}$. The green circles in the DEMETER plane are concentric circles around $\mathbf{B}_{0,\text{source}}$ with radius increments of 100 km.

2.2   Logistics of Experiments

The experiments with HAARP and DEMETER were conducted in a campaign format for four years (2007–2010). Each campaign usually lasted for seven to fourteen consecutive days. The breaks between campaigns were between one to four months and depended on HAARP personnel availability. HAARP was operated by several BAE Systems engineers who also had primary roles in HAARP design and construction. The available HF transmitting time was usually shared between several research institutions. There were cases when HAARP operations lasted for several consecutive days, 24 hours per day. However, more often HAARP operated for about 10 hours continuously. Each campaign required substantial resources, preparation, and planning.

The most important criteria for the allocation of HAARP operation time slots were the natural ionospheric and magnetospheric conditions. Some of them could be planned well ahead, such as daytime/nighttime. Other factors were dependent on current space weather and could not be planned ahead. The Stanford group of researchers, including the author of this work, introduced a new real-time HAARP

management system with the usage of an Internet chat room. With the chat room, the formats of experiments were planned ahead, but the decision to run a specific experiment could be made in real time after observing space weather conditions and data from ground stations. Since DEMETER passes produced a lot of valuable information and lasted for relatively short period, they were often given priority. Usually, 20 to 30 minutes of transmission time were dedicated to DEMETER passes. The part of a pass where it was possible to see the signal lasted up to ten minutes. In view of the sub-synchronous nature of the DEMETER orbit, there were regularly two night and two daytime opportunities every day to see the signal on DEMETER. Even though DEMETER passes lasted for a short time and did not require a lot of HAARP operation time, it was usually not possible to operate HAARP only for DEMETER passes because the start and shutdown of the system required additional time of about an hour and as well the availability of personnel time.

The time and position of DEMETER passes were calculated several weeks before each campaign. As a HAARP campaign was scheduled, DEMETER was programmed for BURST mode operations both over HAARP and over the HAARP conjugate region. Because HAARP could not operate for every pass, usually the closest passes were given priority. For instance, the passes within 300 km distance from $\mathbf{B}_{0,\text{source}}$ were often prioritized. Several HAARP campaign schedules were built around DEMETER passes, and in such situation almost all DEMETER passes could be covered. DEMETER recorded in BURST mode for all planned HAARP campaigns. As a result, there are DEMETER data over HAARP and the HAARP conjugate region when HAARP is both ON and OFF. The ELF transmission format for DEMETER was usually planned ahead, but there were cases when the format was changed in real time just before a DEMETER pass. Such decisions were made on the basis of natural conditions and by monitoring real-time ELF data from ground stations.

2.3   Scientific Instruments

2.3.1   HAARP HF Facility

The High Frequency ionospheric heater used in our study [*Kennedy and Kossey*, 2002] is a component of the High-frequency Active Auroral Research Program (HAARP) facility located near Gakona, Alaska, at the geographic position of 62.39°N, 145.15°W, corresponding to the magnetic shell $L \simeq 4.9$. The construction of the last stage of the HAARP HF facility was completed in 2007. The HAARP HF heater consists of a 180-element phased array antenna fed by distributed transmitters at each antenna element with total maximum continuous power of 3.6 MW. HAARP can operate at HF frequencies ranging from 2.7 MHz to 10 MHz, and in the experiments described below it was used at 2.75–3.25 MHz to provide maximum heating in the D region of the ionosphere [*James et al.*, 1984]. At 3.25 MHz the net radiated power is 3.2 MW, the antenna array gain is 21 dB, the effective radiated power (ERP) at the center of the beam is 407 MW, and the full-width half-power beamwidth is 17.2° in the north-south plane and 13.5° in the east-west plane. In most of our experiments the HF beam was directed vertically upward and the HF carrier was modulated with different types of ELF/VLF modulation which effectively reduces the average HF power by a factor of two. The array can be split into two independent parts, each fed by its own waveform generators.

2.3.2   DEMETER Satellite

DEMETER[1] (Detection of Electro-Magnetic Emissions Transmitted from Earthquake Regions) is a French micro-satellite operated by the Centre National d'Études Spatiales (CNES). The main scientific objectives of the DEMETER mission are to study disturbances of the ionosphere due to seismo-electromagnetic effects, as well as anthropogenic activities such as power line harmonic radiation (PLHR), VLF transmitters, and HF broadcasting stations [*Parrot et al.*, 2006]. It was launched on June 29, 2004

---

[1]The word also refers to "the Goddess of the Harvest" in Greek mythology. In etymology, the word can be interpreted as "Mother-Earth".
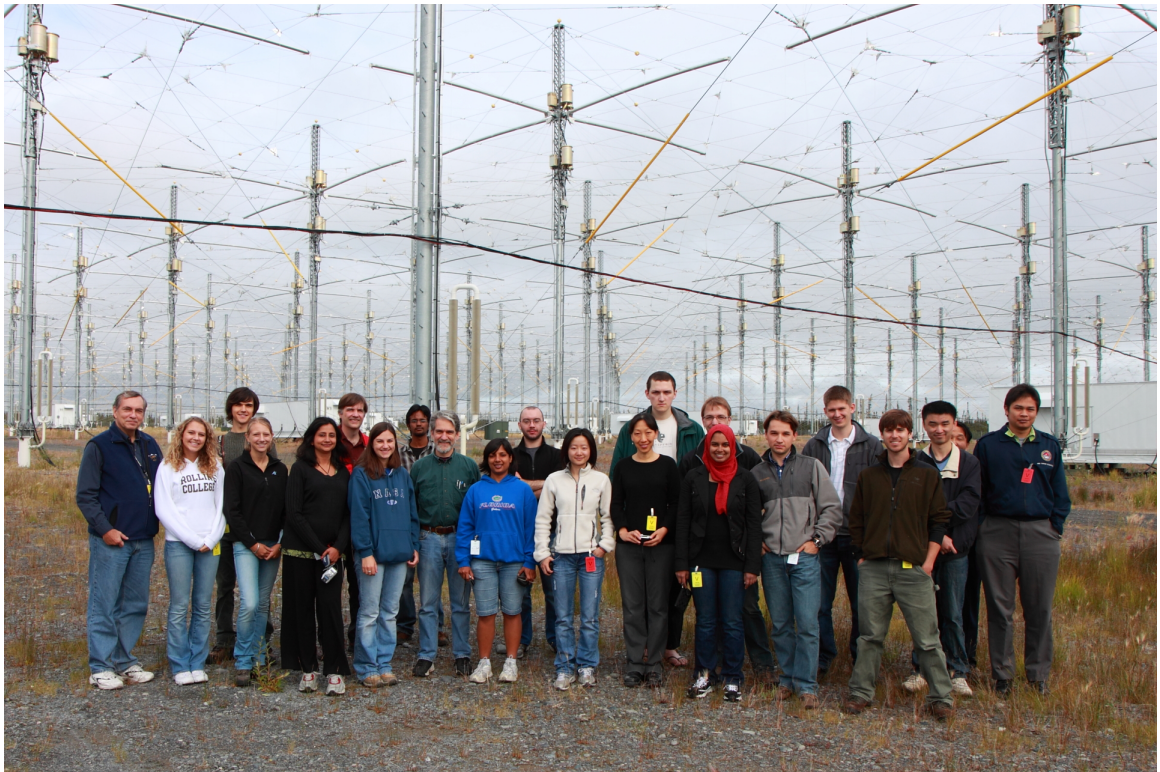
Figure 2.2: A photograph from 2009 HAARP Summer Student Research Campaign. Participants, including the author, stand in the middle of HAARP phased antenna array. There exists a metallic wire sheet below the radiating dipoles at the height of several meters which not only improves the antenna performance but also protects humans and animals.

3.25 MHz vertical HAARP HF beam at 75 km altitude   3.25 MHz vertical HAARP HF beam at 670 km altitude
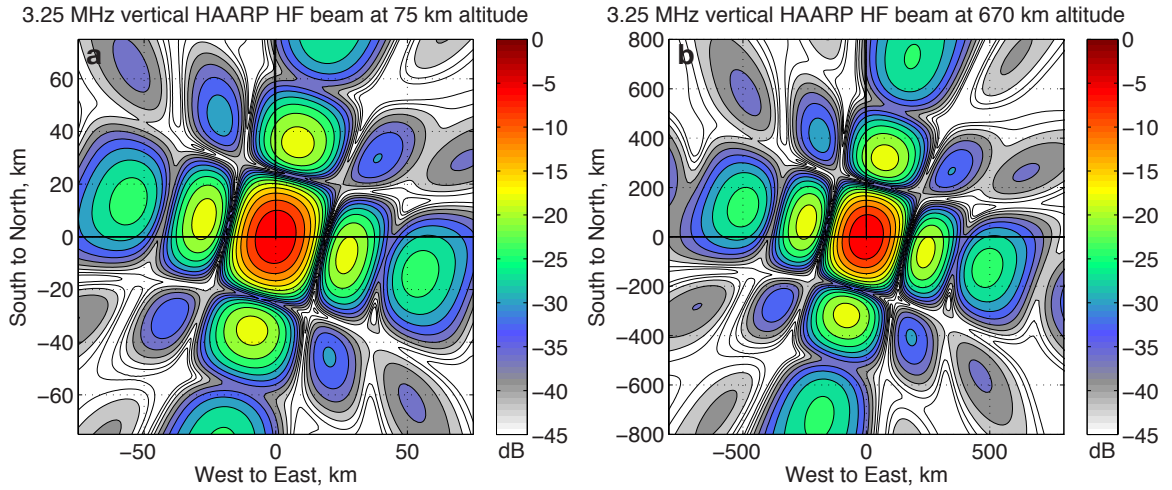
Figure 2.3: The simulated standard pattern of the HAARP antenna array beam at the altitudes of (a) 75 km and (b) 670 km. HAARP beam is directed vertically upward and the HF frequency is 3.25 MHz. The pattern is simulated with the assumption that HF waves propagate in straight lines. This is a good assumption for the propagation in free space up to 75 km altitude, but not always a correct one for the propagation in the plasma up to 670 km altitude.

at 06:30 UTC by a Dnepr rocket from the Baikonour Cosmodrome. It is a three-axis stabilized spacecraft, i.e., nonspinning. The orbit is quasi sun-synchronous circular with an inclination of 98.3°, and the horizontal velocity is about 7.6 km·s^{-1}. The original altitude was 715 km and was decreased to about 670 km (it is between 668 and 673 km) in December 2005. The orbit drifts slowly in local time, crossing the equator close to 10:30 LT on the dayside and 22:30 LT at nightside [*Berthelier et al.*, 2006]. In the first part of the mission, measurements were limited to latitudes below 65° invariant latitude, but starting in early 2007 the possibility to extend this latitude in specific regions beyond 65° was implemented. This extension enabled observations directly over the HAARP HF transmitter. An example of one day of DEMETER orbit projections is shown in Figure 2.4. Since the orbit is quasi sun-synchronous the DEMETER passes can be easily separated into daytime and nighttime events. Figure 2.4 shows the region of interest above HAARP by red circles. From day to day the specific orbit configuration only shifts in the east-west direction and there is always a pair of passes, a nighttime and daytime, that occurs over the green region of interest. The proximity of the passes to the center of the region changes from day to day. Roughly, the configuration repeats every 3–4 days which means that a close pass within 200 km of horizontal distance from the center of the green region occurs at least every 4 days (at least one close nighttime and one close daytime pass every 4 days).

For HAARP experiments, DEMETER operated in the burst mode. In this mode the satellite can record 3 components of DC/ULF **E** field up to 19.5 Hz, 3 components of both ELF **E** and **B** fields up to 1.25 kHz, one component of each field up to 20 kHz (VLF), and HF *E*-field power spectra up to 3.33 MHz. ICE (Instrument Capteur Electrique) is an abbreviation used for the electric field instrument and IMSC (Instrument Magnétomètre Search-Coil) for the magnetic field search coil instrument. Electron and ion densities can be measured by two types of instruments: a Langmuir probe (ISL: Instrument Sonde de Langmuir) and a thermal plasma analyzer (IAP: Instrument Analyseur de Plasma). For HAARP experiments, DEMETER burst recordings were specially extended beyond the normal termination at the invariant latitude of 65°.
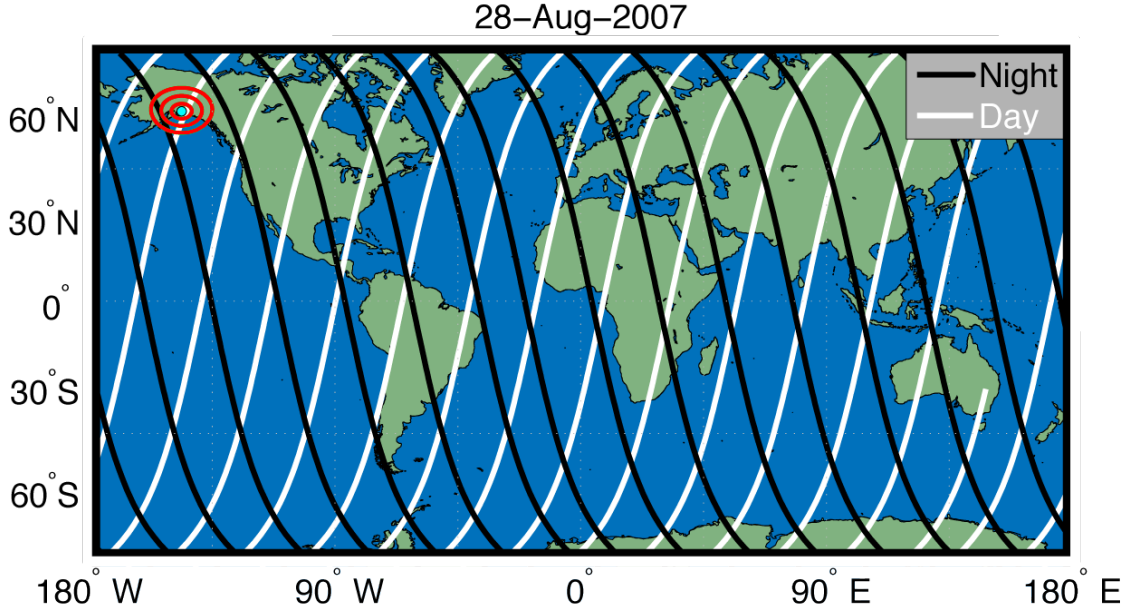
Figure 2.4: Projection of DEMETER passes to the ground during a 24-hour period.

For this work, ICE and IMSC were used in the VLF mode. As shown in Figure 2.5, ICE sensors are deployed on booms 4 meters from the satellite [*Berthelier et al.*, 2006]. The component of **E**-field reported here is a horizontal component E_{12} perpendicular to the orbital plane. ICE has a sensitivity of $\sim$0.1 μV·m^{-1}·Hz$^{-1/2}$, and the dynamic range is $>$80 dB. The search coil magnetometers of IMSC are mounted at the end of a 1.9 m boom and have a sensitivity of -28 dBpT at 1 kHz [*Parrot*, 2006]. In this work the horizontal component of **B** inclined at $45°$ to the **E**-field component is used.

The DEMETER Langmuir probe measures primarily the electron density N_e and electron temperature T_e with 1 second time-resolution [*Lebreton et al.*, 2006]. N_e can be measured in the range of 10^8–5×10^{11} m^{-3} and T_e in the range of 600–10000 K. Accuracies of $\pm 30\%$ for N_e and $\pm 15\%$ for T_e are generally accepted for the situations in which the real ionospheric plasma with bulk motion and magnetic field effects is approximated by "ideal" plasma conditions, i.e., Maxwellian distributions. Due to the contamination of the ISL probe at launch, the measured values of T_e are in general thought to be significantly higher than real ones by about 800 K for a mean temperature of $\sim$2500 to 3000 K (*J.-J. Berthelier* [2010], private communication; *Lebreton*
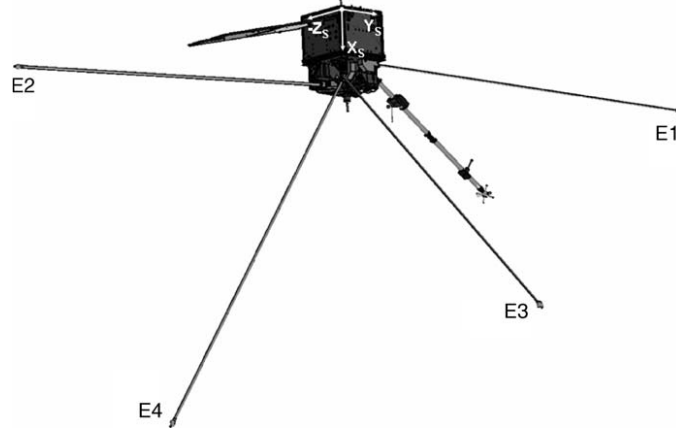
Figure 2.5: The configuration of the DEMETER satellite **E**-field sensors [*Berthelier et al.*, 2006]. By default, the component of **E**-field used in our work is the horizontal component E_{12} perpendicular to the orbital plane. The orbital plane is the geometrical plane in which the orbit lies (XZ in the figure).

[2012]). *Lebreton et al.* [2006] also noted that under auroral plasma conditions the plasma parameters may be inaccurate in absolute value but that their variations may still be identified. Data for ion densities and temperature from IAP are used as auxilary data in this work. It should be noted that sometimes unusually high peaks in ion temperature are seen, e.g., on 2007-02-26 07:13 UT. Most often, these high peaks are due to overestimations resulting from the specifics of automatic data processing (*J.-J. Berthelier* [2010], private communication), but this topic is beyond the scope of the current work since it does not affect our results.

2.3.3 Ground ELF/VLF Receiver System

Even though the emphasis of the current work is on satellite measurements, the ELF measurements on the ground are also used as complimentary and baseline observations. Ground ELF observations were obtained with Stanford AWESOME (Atmospheric Weather Electromagnetic System for Observation, Modeling, and Education) ELF/VLF receiver system [*Cohen et al.*, 2010c]. In particular, observation from Chistochina, AK; Gakona, AK; Juneau, AK and shipboard observations on R.V. Tangaroa

are used. The author participated in maintenance and deployment of AWESOME systems before and during several HAARP campaigns.
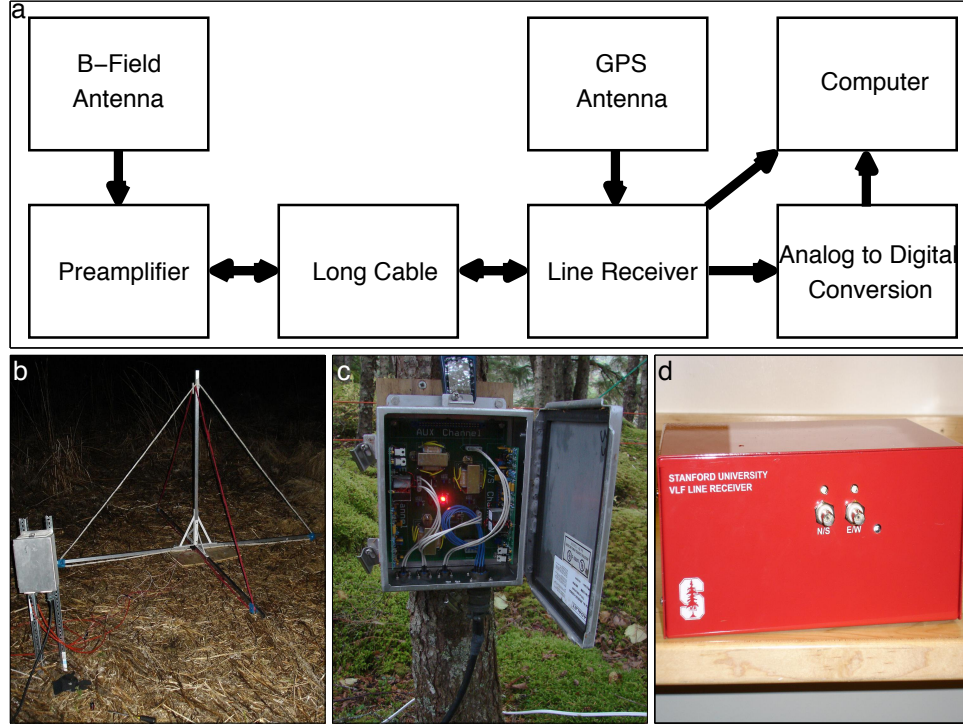
Figure 2.6: (a) Block diagram of AWESOME ELF/VLF ground receiver system: (b) antenna, (c) preamplifier, (d) line receiver. *Courtesy of M.Cohen.*

The main components of AWESOME system are the antenna, preamplifier and line receiver (Figure 2.6). The antenna and preamplifier are installed outdoors and as far away from any noise sources as possible (up to 2 km from the antenna). The line receiver is installed indoors and is usually connected to a computer with an Internet connection, so that the data can be accessed in real time from anywhere. Each antenna consists of wire loops sensitive to the magnetic field. Two orthogonal loops record two horizontal components of the ELF magnetic field. The AWESOME receiver samples data at 100 kHz and the upper cutoff frequency is 47 kHz. The low cutoff frequency can be as low as 80 Hz. Sensitivity over the ELF frequency range enables detection of signals over a 1 Hz bandwidth as low as $\approx$1 fT when the area

of the loop antenna is 25 m^2 [*Cohen*, 2009]. GPS is used for timing accuracy, and at least 100 ns accuracy can be achieved.

2.4 Description of Models

Here several models of ELF wave propagation are introduced. The emphasis is on full-wave and ray tracing models that are used in this work. However, a finite-difference time-domain (FDTD) technique is also mentioned in comparison with the full-wave method. Several properties of the models relevant to this work are described. The descriptions given below are by no means complete and are simply intended to review the conditions in which the models can be applied and the types of solutions they produce. Complete description of the models can by found in the given references.

2.4.1 Full-Wave Modeling and FDTD

The Stanford Full-Wave Method (SFWM) used in this work is described thoroughly by *Lehtinen and Inan* [2008]. A full-wave solution implies that all field components of electromagnetic waves can be found within the geometrical domain of a problem. In other words, the 3D distribution of **E** and **B** (or **H**) is calculated from Maxwell's equations either in the frequency domain or in the time domain. Another popular method that solves for the full solution of electromagnetic fields is the finite-difference time-domain (FDTD) technique. FDTD requires little assumptions about the media in the problem, except on the boundary of the geometrical domain [*Taflove and Hagness*, 2005; *Elsherbeni and Demir*, 2009; *Inan and Marshall*, 2011]. FDTD is a straightforward and intuitive method, but often requires more computer resources than are available, even on supercomputers. Also, it uses the resources inefficiently if only monochromatic waves are considered. To circumvent this inefficiency, numerical methods can be developed in the frequency domain using Fourier transforms in time. Doing so does not imply any assumption in any given problem, because any waveform can be transformed into the Fourier domain and then transformed back after the solution for each monochromatic wave is found [*Bracewell*, 2000]. Numerically, every

Fourier component (monochromatic wave) can be calculated independently either consequently or at the same time (parallel computation), within the extent of available computer resources. The SFWM is a frequency domain method not only in time, but in space. The solutions of the fields are given in the form of a linear combination of monochromatic plane waves $\sim e^{i(k_0 \mathbf{n}\cdot\mathbf{r} - \omega t)}$, where i is the imaginary unit, $k_0 = \omega/c$, ω is the wave frequency, c is the speed of light in vacuum, and $\mathbf{n}$ is the refractive index vector. In such situation, Maxwell's equations for source-free medium are converted from first-order differential to algebraic equations

$$\mathbf{n} \times \mathbf{H} = -\hat{\varepsilon}\mathbf{E}, \tag{2.2a}$$

$$\mathbf{n} \times \mathbf{E} = \mathbf{H}, \tag{2.2b}$$

where $\mathbf{n}$ and $\hat{\varepsilon}$ are respectively the dimensionless refractive index vector and the permittivity tensor, with permeability $\mu = 1$, and $\mathbf{E}$ is in SI units, while $\mathbf{H} = \sqrt{\mu_0/\varepsilon_0}\mathbf{H}_{\text{SI}}$.

The SFWM method employed here uses several important assumptions which makes it computationally much more effective than FDTD, albeit less universal. The key assumption is that the media is stratified along one dimension (Figure 2.7). In other words, the geometrical domain is 3D but the refractive index changes just along one coordinate. In our case it is the vertical z-coordinate along which the medium is divided into horizontal layers. Within each layer the refractive index is taken to be constant. This approximation is possible because the Earth's ionosphere is a good example of a horizontally stratified media in which parameters change predominantly along one vertical dimension. Other methods for finding fields in stratified media are reviewed in [*Budden*, 1985, Ch. 18]. Many of those methods lack numerical stability because waves which are evanescent in one direction numerically and non-physically grow in the opposite direction. As a result they "swamp" the physically possible waves of interest [*Budden*, 1985, pp. 574–576]. The SFWM method is stable and is designed to suppress such "swamping". It uses a recursive calculation of reflection coefficients and mode amplitudes [*Nygren*, 1982], and also allows the use of an arbitrary configuration of the radiating sources.
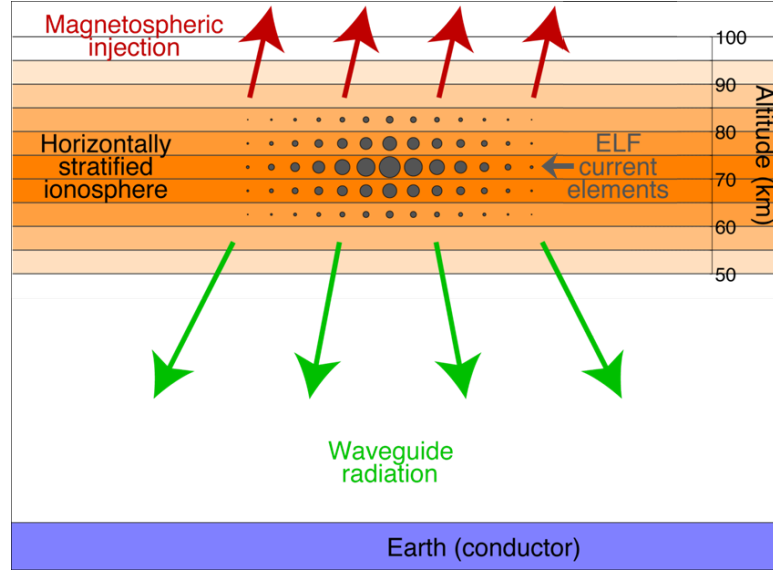
Figure 2.7: Stanford Full-Wave Method (SFWM) geometry with key assumptions: horizontally stratified media and Earth as a good or perfect conductor. *Courtesy of M.Cohen.*

The SFWM method assumes the ground surface and ionospheric boundary to be planar. This approximation is discussed in Section 2.1. As a result, the Cartesian coordinate system from this section can be used.

The altitude-dependent Earth's magnetic field is modeled as homogeneous in every layer. The values of the magnetic vector are taken from the IGRF model [*Finlay et al.*, 2010] on the ground at the location of HAARP. Those values together with the plasma density are used to calculate the wave refractive index at each layer. The assumption of homogeneous magnetic field in a layer is justified by the small size of the computational domain in comparison to the characteristic size of Earth's magnetic field variation.

The ground in this frequency range is modeled either as a good conductor with finite conductivity or with infinite conductivity. The last approximation holds well in the considered frequency range, and leads to a condition that the horizontal electric field should be equal to zero at the Earth's surface. On the other hand, the ionosphere is modeled with a finite conductivity tensor in each layer, which leads to realistic

penetration of ELF energy up into space. In other words, the propagation in the space between the ground and the ionosphere is similar to that within a parallel plate waveguide with ideal bottom boundary and non-ideal top boundary.

The current source for which it is possible to find solution of the fields in the model is a horizontal current with harmonic dependence on time and perpendicular coordinates that flows only in plane $z = z_s$:

$$\mathbf{J} = \mathbf{I}_\perp \delta(z - z_s) e^{ik_0(\mathbf{n}_\perp \cdot \mathbf{r}_\perp) - i\omega t}. \tag{2.3}$$

where $\mathbf{I}_\perp$ is the perpendicular current amplitude. If the source region has an arbitrary shape, the horizontal Fourier decomposition of the sources is used at each altitude:

$$\mathbf{J}_\perp(\mathbf{n}_\perp, z) = \iint \mathbf{J}_\perp(\mathbf{r}_\perp, z) e^{-ik_0(\mathbf{n}_\perp \cdot \mathbf{r}_\perp)} d^2 \mathbf{r}_\perp. \tag{2.4}$$

The fields are calculated separately for every Fourier space component of the current and are then used in an inverse Fourier transform to get the full distribution of fields.

The auroral electrojet current modification by HAARP, the ELF source current, was modeled by *Payne et al.* [2007]; *Cohen* [2009]; *Cohen et al.* [2011]. The model used in these works implements the classical ideas of heating plasmas by powerful electromagnetic waves described in [Ch. 8, *Ginsburg*, 1960; *Stubbe et al.*, 1982; *Rietveld et al.*, 1986]. The HF heating model solves an energy balance equation for electron temperature in 3D space for consequent time steps. The electron temperature is used to calculate a modified ionospheric conductivity tensor. Only part of the energy of the HF waves is absorbed in the ionospheric D-layer. The remaining HF energy propagates upward and can be detected by DEMETER, as described in Chapter 3. For ELF generation we are concerned about the energy absorbed and transformed to random electron motion (i.e., electron temperature; electron temperature distribution is assumed to remain Maxwellian) over the altitude range where the auroral electrojet current is present. At these altitudes, modification of the electron temperature and conductivity creates the most effective modification of the natural electrojet current. An example of such modification is presented in Figure 2.8 for an HF frequency of 3.2 MHz and an ELF frequency of 1875 Hz. Similar currents are used as source currents

in SFWM model. From Figure 2.8 it is seen that the horizontal size of the source region is about 30–50 km. The maximum current is at the altitude of 78 km.
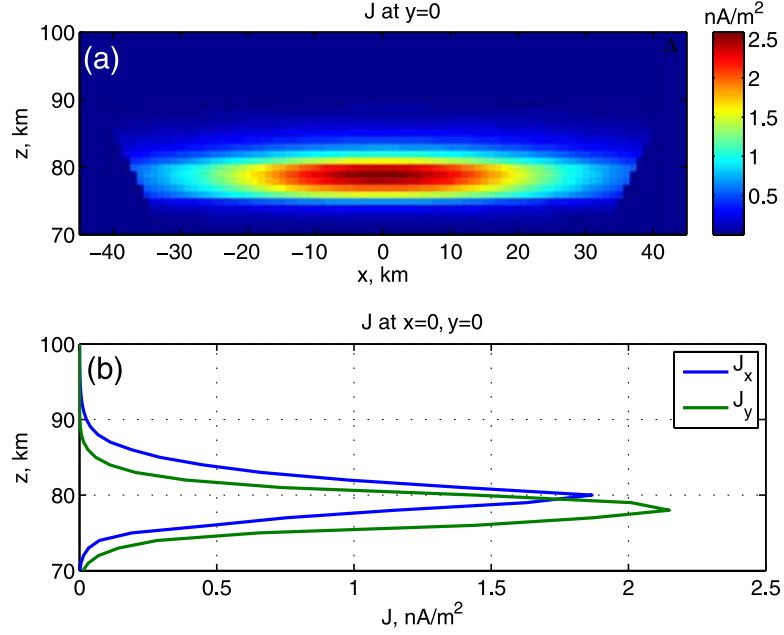
Figure 2.8: (a) Absolute value of the amplitude of the modulated current density. The vertical currents are negligible, and the horizontal ones are due to the Pedersen and Hall mechanisms. (b) The components of the current density in the middle of the source region. The ambient electrojet field is $E_0 = \hat{x}(-25\,\mathrm{mV\cdot m^{-1}})$, so J_x corresponds to the Pedersen, and J_y to the Hall current. Adopted from *Lehtinen and Inan* [2008].

2.4.2   Ray Tracing

Ray tracing is a classical and established method [*Debye*, 1911; *Kravcov and Orlov*, 1980; *Born et al.*, 1999] to solve Maxwell's equation in the approximation where the wavelength is small compared to variations in medium parameters. Ray tracing is the first approximation of geometrical optics when only ray trajectories are calculated. Because of this, ray tracing and geometrical optics terms are often used interchangeably in the same context. Mathematically similar methods are widespread in other disciplines: geometrical acoustics, geometrical seismics, WKB method in quantum

mechanics and so on. The ray tracing method can give an easy visual solution for the rays of electromagnetic waves in complicated inhomogeneous media. From a mathematical point of view, a ray is a line along which the electromagnetic energy propagates away from a point source. From a physical point of view, a ray occupies a finite volume in space. It is possible to show that this volume is equal to the Fresnel volume, or the volume spanned by the enveloping surface of the first Fresnel zones along the mathematical ray [*Kravcov and Orlov*, 1980]. The differential equation of geometrical optics give solutions for the mathematical rays, but the physical meaning of them should always be carefully interpreted.

Ray tracing equations can be written as a system of six ordinary differential equations of the first order for 3D problems. The unknowns are 3 coordinates $\mathbf{r}$ and 3 wave vectors $\mathbf{k}$. The equations are presented below in the vector form:

$$\frac{d\mathbf{r}}{d\tau} = \frac{c}{\omega}\mathbf{k} - \frac{\omega}{c}\frac{\partial n^2}{\partial \mathbf{k}}, \tag{2.5a}$$

$$\frac{d\mathbf{k}}{d\tau} = \frac{1}{2}\frac{\omega}{c}\frac{\partial n^2}{\partial \mathbf{r}}, \tag{2.5b}$$

where τ is a parameter along a ray trajectory, n is a refractive index of the medium, c is the speed of the light, and ω is the angular frequency of the wave. The dependence of the refractive index n on position $\mathbf{r}$ and wave vector $\mathbf{k}$ should be known beforehand so that the terms with partial derivatives on the right are calculated before solving the differential equations. In the simplest case when the refractive index of the media depends neither on the position nor on the wave vector, the terms with partial derivatives are equal to zero and the ray trajectory is a straight line. Also, initial conditions should be specified: $\mathbf{r}(0) = \mathbf{r}_0$ and $\mathbf{k}(0) = \mathbf{k}_0$. Since the dependence of the refractive index on $\mathbf{r}$ and $\mathbf{k}$ is usually a complicated function, the differential equations are often solved numerically.

The ray tracing method can be used if the next three conditions are satisfied

[*Kravcov and Orlov*, 1980]:

$$\frac{\lambda_0}{2\pi n} \ll \frac{|A|}{|\nabla A|} \text{ (for amplitude),} \tag{2.6a}$$

$$\frac{\lambda_0}{n} \ll \frac{|k_i|}{|\nabla k_i|} \text{ (for direction),} \tag{2.6b}$$

$$\frac{\lambda_0}{n} \ll \frac{|n|}{|\nabla n|} \text{ (for medium),} \tag{2.6c}$$

where λ_0 is the wavelength in free space, A is the wave amplitude, and k_i is a component of the wave vector. The first condition states that the amplitude of the wave should be changing slowly over the distance of one wavelength. The second condition states that the wave vector direction should be changing slowly over the distance of one wavelength. The third condition states that the refractive index of the medium should be changing slowly over the distance of one wavelength. The quantities on the right hand side have the dimensions of length and are called the characteristic scales of the corresponding parameter variation. In our work we use ray tracing to study the behavior of the Region 1 Column of radiation (discussed later in detail). The first two conditions are easily satisfied for the column everywhere because the direction of the column and the amplitude within it change smoothly. The third condition for medium is not satisfied everywhere in the ionosphere. Figure 2.9 shows the values of the wavelength in the medium (λ_0/n) for 2 kHz by blue curve and the characteristic scale of n variation by green curve as a function of altitude. The condition 2.6c starts to be satisfied consistently only above approximately 200 km. This is the altitude at which we start ray tracing of the waves propagating upward.
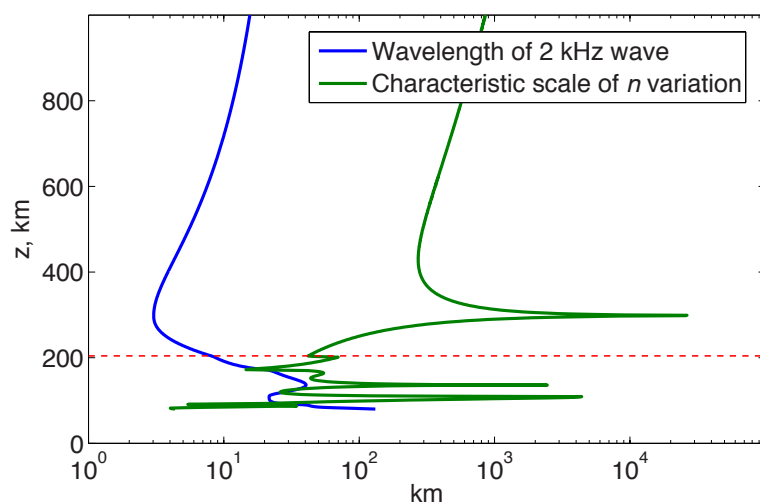
Figure 2.9: The applicability of ray tracing for 2 kHz whistler waves. At the altitude of about 200 km and above, the characteristic scale of refractive index variation exceeds the wavelength for the selected model of plasma density, and therefore ray tracing can be used in this region.

Chapter 3

Ionospheric Plasma Environment above HAARP

3.1 Introduction

The comprehensive discussion of wave propagation phenomena is impossible without an understanding of the media in which these waves propagate. The purpose of this chapter is to describe several important characteristics of the high-latitude ionospheric plasma as related to HF-heating. The plasma density is the primary parameter affecting the propagation of ELF and HF waves in the ionosphere. Moreover, there is a possibility that powerful HF radiation can modify the plasma density [*Duncan et al.*, 1988; *Gondarenko et al.*, 2002; *Frolov et al.*, 2008]. This modification can be excluded in the case of artificially generated ELF waves because of their low relative power. These ELF waves can only be affected by pre-existing plasma variations driven by other effects.

Recently there have been several reports of the modification of the ionospheric plasma density by powerful high frequency (HF) heaters situated in high-latitude regions [*Milikh et al.*, 2008; *Wong et al.*, 2009]. In these works the observed variation of plasma density is attributed to HF-heating. However, the detection of HF-generated density modifications is generally a complicated problem in this region, because it is

directly affected by the solar wind and energetic particles from the Earth's magnetosphere, and as a consequence the ionospheric parameters therein are more variable than at lower latitudes [*Hunsucker and Hargreaves*, 2003, Ch. 5]. One important feature of the ionosphere above the HAARP HF heater which introduces variability is the main ionospheric trough. Unfortunately, this feature was not discussed in the works of *Milikh et al.* [2008] and *Wong et al.* [2009], although satellite observations from these works clearly show the presence of the main trough.

The main ionospheric trough, often also called the mid-latitude trough [*Kelley*, 2009], is a region at F-layer altitudes and in the topside ionosphere, where the plasma, dominated by heavy O^+ ions, is depleted and usually displays irregularities of large amplitude. The main trough is limited in latitudinal width, but extended in the east-west direction, and marks the boundary between high- and middle-latitude regions of the ionosphere [*Hunsucker and Hargreaves*, 2003, Sec. 5.4]. In general, the trough can be observed at invariant latitudes of $50°$–$70°$, and it has a latitudinal width up to $10°$, but these figures are highly variable. The main trough is mostly a night-side phenomenon and moves to lower latitudes with increasing geomagnetic activity. The basic cause of the main ionospheric trough is considered to be the structure of ion convection paths in which some of the paths do not encounter a production region for several hours, which is enough for the plasma density to decay [*Rodger et al.*, 1992].

Another important phenomenon observed on satellites in the region above HAARP is ELF electrostatic turbulence. ELF electrostatic turbulence often disrupts satellite observations of ELF waves generated by ionospheric modification with the HAARP HF transmitter. In the work of *Piddyachiy et al.* [2008] several ELF pulses are masked by the presence of ELF electrostatic turbulence. ELF electrostatic turbulence prevents the detection of those pulses at DEMETER altitude but not their generation due to HF heating, because the generation occurs at lower altitudes in the D region [*Moore et al.*, 2007]. Overall, ELF electrostatic turbulence should be taken into account during the analysis of satellite observations of ELF waves produced by such active experiments.

The name "electrostatic turbulence" was given to the phenomenon observed in

this work in the pioneering paper by *Kelley* [1972]. Here we call it ELF electrostatic turbulence to distinguish from other types of electrostatic turbulences found in literature, e.g. in *Berthelier et al.* [2008]. The main signature of ELF electrostatic turbulence is the presence of broadband impulsive perturbations from DC up to a few kHz in the electric field and no corresponding perturbations in the magnetic field in the frequency range DEMETER can reliably observe ($\sim$100 Hz to 20 kHz). Because of the previously established association of ELF electrostatic turbulence with density irregularities [*Kelley*, 1972; *Temerin*, 1978; *Kelley*, 2009, and references therein], in situ ELF *E*-field recordings of electrostatic turbulence can in fact be used as an additional diagnostic tool to determine the location and structure of such irregularities.

Below we present DEMETER satellite observations of the ionospheric trough and density irregularities in relation to HF transmitter operation. First, we show specific cases which demonstrate that the trough and density irregularities can occur in the region over HAARP as well as in regions well displaced from the HAARP location. Then, making use of data from 100 passes of DEMETER over HAARP we show that there is no apparent correlation between the trough observations and HF transmitter transmissions. The observations demonstrate that the ionospheric trough is often observed in the region near HAARP and generally constitutes the dominant component of all density variations in this region. Afterwards, a comparison with works of *Milikh et al.* [2008] and *Wong et al.* [2009] shows that the effects presented therein can be attributed not only to HF heating but to natural density variations in the main trough also. The implication of the trough presence in relation to HF heating experiments is discussed at the end.

Substantial portions of the work reported in this chapter have been published in *Piddyachiy et al.* [2011].

3.2 DEMETER Observations of the Main Ionospheric Trough

A typical representation of data from instruments used in this chapter is shown in Figure 3.1. Panel (a) contains an on-board spectrogram from ICE for HF frequencies relevant to each experiment. Panel (b) is an on-board spectrogram from ICE in the ELF range that contains the effect discussed in this work. Panels (c) and (d) show corresponding recordings of N_e and T_e measured by the DEMETER Langmuir probe. Panels (e) and (f) represent ion density (usually just the dominant ions O^+) and ion temperature measured by IAP. In this work we are interested in the variation of these parameters. Also the trajectory of DEMETER projected vertically onto the ground is shown on a map in the lower right hand corner. Crosses on the satellite path correspond to five time and position labels below the panels. A red dashed vertical line marks the closest approach of the DEMETER sub-satellite point to HAARP, and vertical black dotted lines mark the approximate boundaries of the main trough. When referring to a distance between the satellite and a ground object we refer to the distance d between the sub-satellite point and the object, unless specified otherwise.

3.2.1 HAARP Transmitter ON

One of the first observed cases (we will call it Case 1) which motivated the current investigation occurred around 06:53 UT on 29 July 2007 (Figure 3.1). The local time is 21:12. This DEMETER pass is relatively close to HAARP within $d =100$ km. HAARP is transmitting vertically upward a signal designed to study ELF waves on DEMETER. The format of the signal represents AM modulation of the HF carrier of 3.3 MHz with a repeated sequence of tones of 613 Hz (1 sec long) and 2011 Hz (1 sec), and a ramp from 0 to 2 kHz (2 sec). X-mode polarization is used. Table 3.1 summarizes the parameters of this and the rest of the cases presented below. The detailed discussion of the ELF wave generation by HAARP is postponed to the next chapters. For the purposes of this chapter the ELF format modulation is irrelevant and is given for this case only for reference.
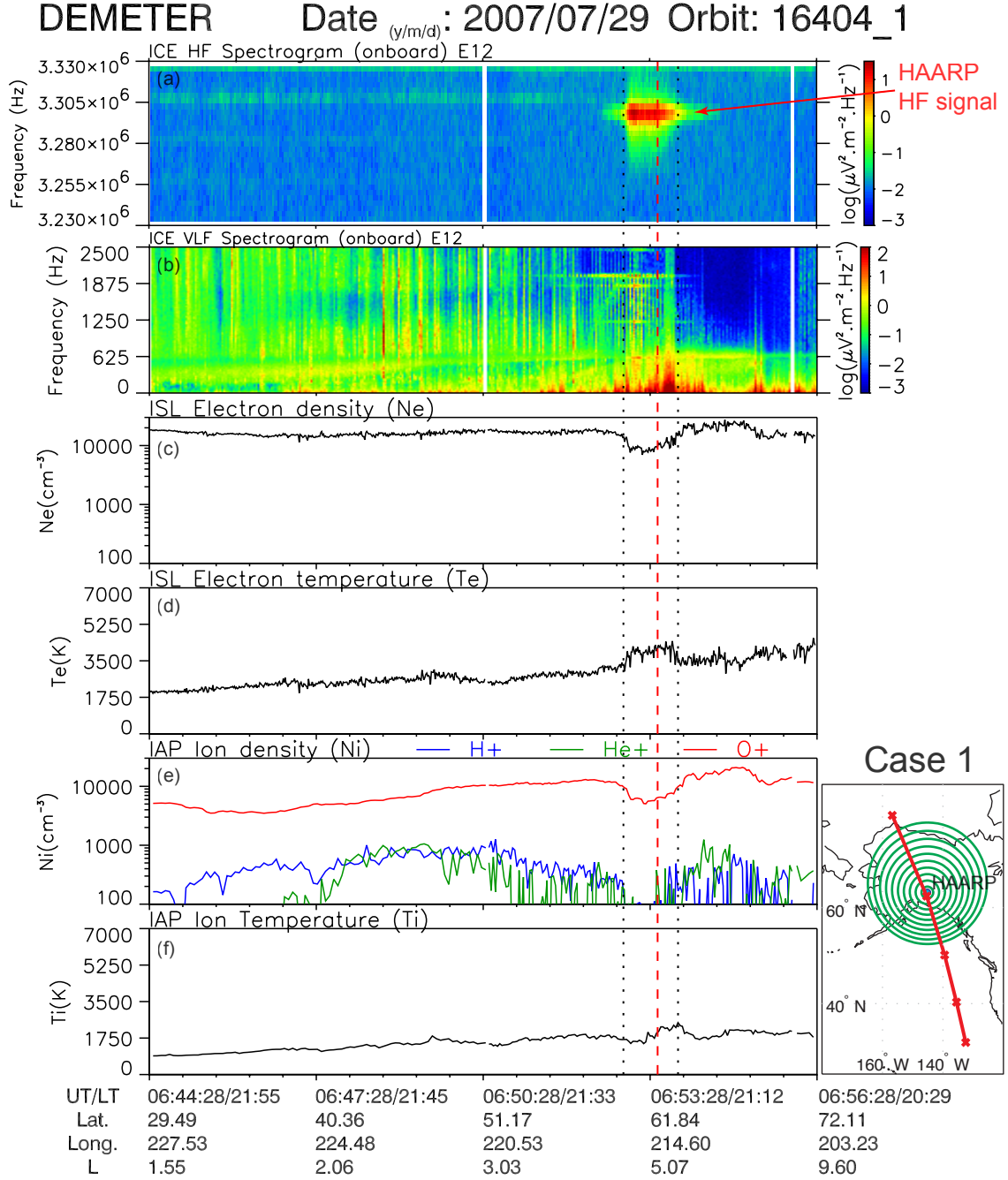
Figure 3.1: DEMETER observations of the trough over transmitting HAARP. (a) HF spectrogram of *E*-field. (b) VLF spectrogram of *E*-field showing HAARP signal, natural emissions, and ELF electrostatic turbulence. (c) electron density; (d) electron temperature; (e) ion density; (f) ion temperature showing the main trough over HAARP.

Table 3.1: Parameters of HAARP transmissions

Case #	Date and time[a], UT	HF power, kW	HF freq., MHz	Polari- zation	Modu- lation	d, km
1	2007-07-29 06:53	3560	3.30	X	AM	60
2	2007-02-26 07:10	3540	3.25	X	AM	210
3	2008-03-19 07:03	3600	2.75	X	AM	230
4	2007-04-30 06:40	0	-	-	-	150
5	2007-09-21 06:40	0	-	-	-	110
6	2007-04-21 06:58	0	-	-	-	100
7	2007-12-01 06:58	0	-	-	-	150
8	2007-04-28 07:16	3560	3.20	O	AM	310

[a] – The time represents the closest approach of DEMETER. The actual HAARP operation lasted for 20 minutes at least.

From the top spectrogram (a) of Figure 3.1 it can be clearly seen that HAARP HF waves penetrate up to the altitude of DEMETER and are observed for about 100 s which is equivalent to a satellite path length of 760 km. The maximum intensity is observed for 60 s, or 450 km. Most likely this corresponds to the main beam of the transmitter which has spread after propagation through the ionospheric plasma. For comparison, if the HF signal were propagating in free space, the width of the main lobe at DEMETER altitude at the half power level would be 200 km, and at the level of the first zero in the radiation pattern it would be 450 km. The maximum level of the signal is estimated to be 1 mV·m^{-1}.

In panel (b) natural and HAARP-generated ELF emissions in the range 0–2500 Hz are shown. The maxima of ELF and HF waves are separated by ∼100 km possibly because ELF radiation in the whistler mode propagates predominately close to the Earth's magnetic field lines (this will be discussed in detail in chapters below), while HF waves propagate mostly vertically upward in this case.

Panels (c)–(d) show that the electron density and temperature exhibit relatively small (less than 10%) variations below 60° latitude. From 60° to 65°, a large scale decrease in the electron density is observed, followed by an increase from 65° to 70°. The electron temperature exhibits only a large scale increase from 60° to 65°.

Also starting at 60°, an increase of small scale variations in these two parameters is present. It is clear that the dominant ion density and temperature in panels (e)–(f) show similar large scale variations.

It is interesting that in this case a region of density decrease and temperature increase corresponds exactly to the region of high HF field (panel (a)). Also low frequency broadband noise up to ∼600 Hz in the ELF electric field (panel (b)) can be recognized. The magnetic component of the ELF field (not shown here) exhibits no similar increase in noise. This broadband noise is purely electrostatic and most likely it is ELF electrostatic turbulence.

Figure 3.2 shows waveforms of the Ultra Low Frequency (ULF) detector for the same case. It is seen that the scale of perturbations inside the main trough is broad, i.e. from the size of the whole region of the trough (several hundreds of kilometers) to much smaller sizes of variations within the trough, and down to a minimum detectable level of tens of kilometers. Here we suppose that ULF variations are the continuation of ELF variations down to DC frequencies and that they stem from the spatial variations inside the trough. However, temporal variations may also be present, and on the moving platform they cannot be easily distinguished from spatial variations.

Another HAARP/DEMETER experiment at a similar local time is presented in Figure 3.3 (Case 2). The HAARP HF signal in this case is seen over a much larger region (for 250 s or about 2000 km). This is a more typical situation than in Case 1. In such situations we most probably also see the first side lobes of the transmitter signal which are typically 15 dB less than the main lobe. The maximum of the ELF signal is also shifted in space with respect to the HF, but that fact is not as clear here because the HF region is more spread.

The important observation in this case is that the region illuminated by the HAARP HF transmitter and the region of density irregularities generally do not coincide. Irregularities in electron density and temperature together with ELF electrostatic turbulence start at higher latitudes.

Figure 3.4 shows a typical spectrogram of the B-field from a ground-based receiver in Chistochina (30 km from HAARP) and typical higher resolution ELF spectrograms of both E and B fields on DEMETER. It is clear that the search-coil magnetometer on
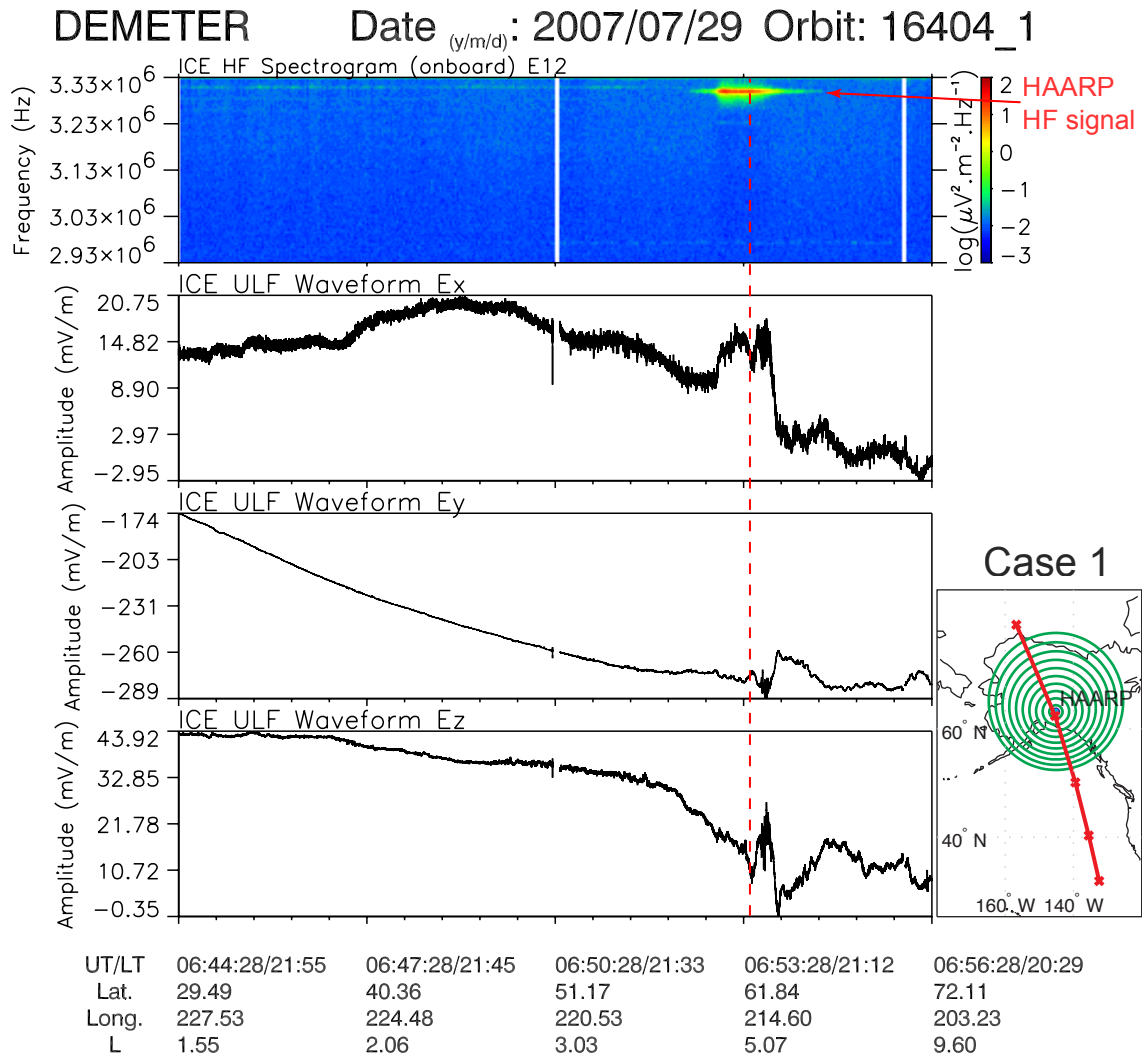
Figure 3.2: Additional data for Case 1 together with repeated HF spectrogram. ULF recordings (three bottom panels) in the region above HAARP show the broad scale of variations inside the main trough, from tens to hundreds of kilometers.
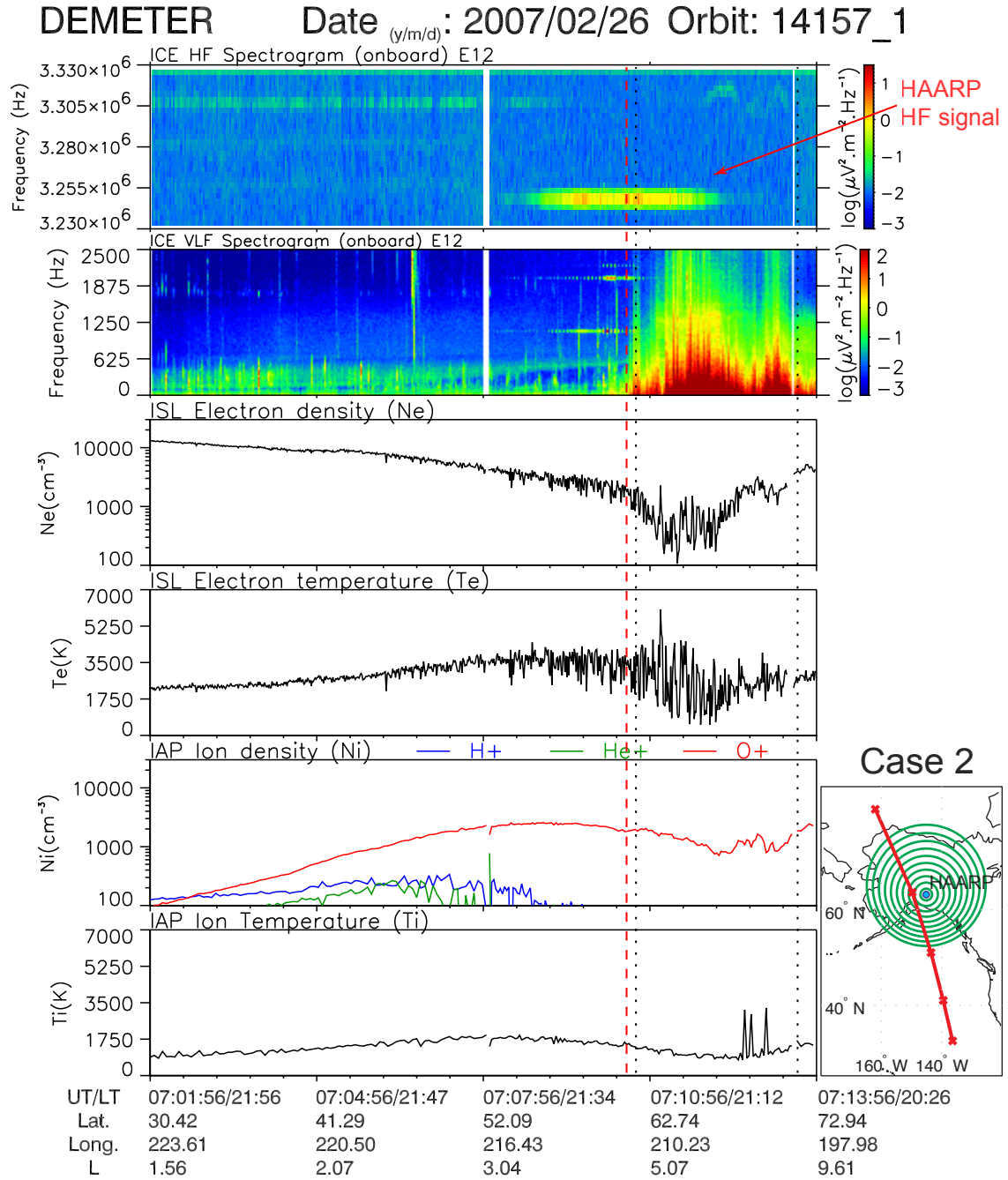
Figure 3.3: Panels are similar to those in Figure 3.1. This is Case 2 on 2007-02-26 which demonstrates that perturbations (five bottom panels) can be displaced from the HAARP HF radiation (top panel) when HAARP is ON.

the satellite shows no response in the region with irregularities where ELF electrostatic turbulence is seen. The ground receiver also does not record any signals similar to electrostatic turbulence; only sferics and HAARP-generated pulses are seen. On the ground, free space EM waves are observed, and therefore the E-field can easily be deduced from the B-field measurements. This means that perturbations in the E-field are not present either, and there are no propagating waves associated with the ELF electrostatic turbulence that reach the ground.
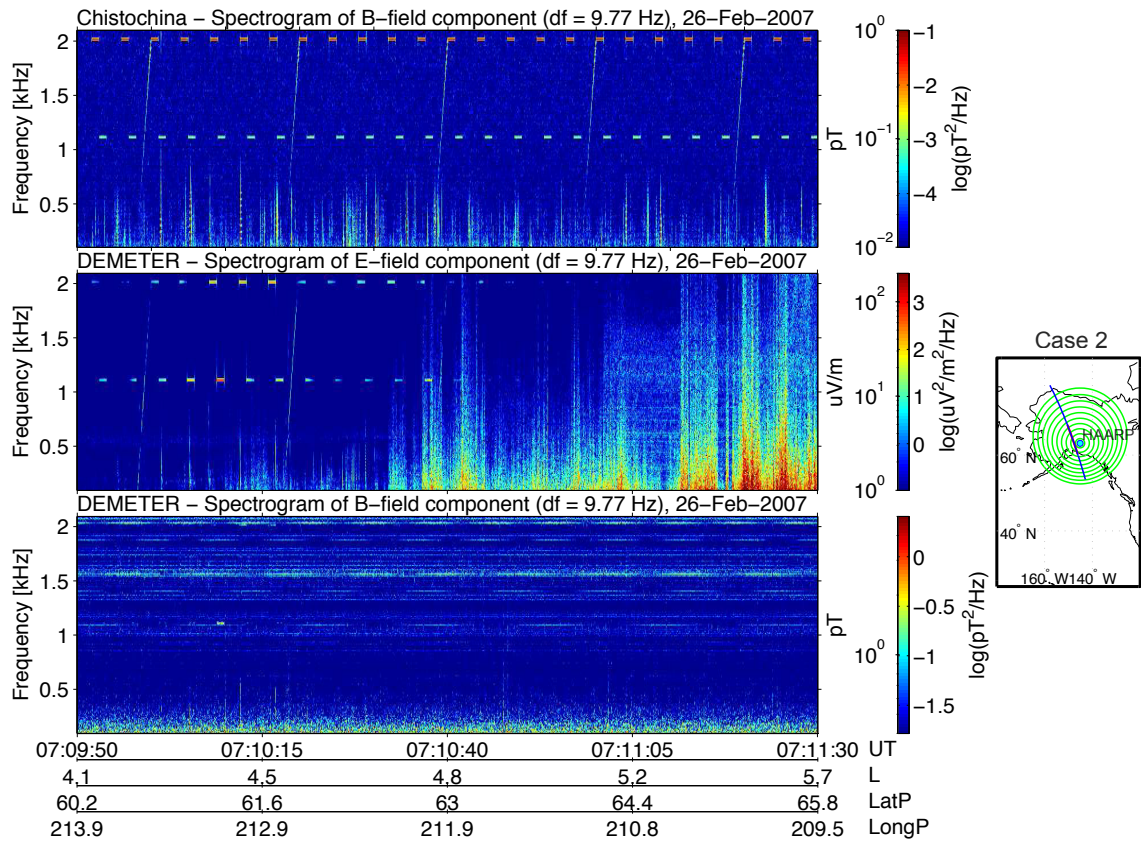
Figure 3.4: Additional data for Case 2. The top panel contains a spectrogram from a ground-receiver in Chistochina near HAARP. The middle and bottom panels show the typical high resolution spectrograms of E and B fields on DEMETER in ELF range over a part of the main trough. This clearly shows that ELF electrostatic turbulence is a phenomenon that occurs only in E-field observations in space and not on the ground.

One more case with HAARP transmission on 2008-03-19 is shown in Figures 3.5

and 3.6 (Case 3). The behavior of HF and VLF HAARP-generated radiation is similar to Case 2. Here it also does not coincide with the perturbations in ion and electron densities and temperatures. In this case two types of perturbations occur. One is a confined trough in electron and ion densities around 70° with corresponding ELF electrostatic turbulence. Another occurs at lower latitude and consists of electron density irregularities that are spread over a much bigger region. The second perturbation also coincides well with ELF electrostatic turbulence. Figure 3.6 shows that ELF electrostatic turbulence goes down to ULF frequencies which is a typical characteristic of its observation on DEMETER.

Lower frequencies corresponds to large scale variations such as those seen in Figure 3.2 where the ULF waveform for a similar case is plotted.

3.2.2 HAARP Transmitter OFF

In order to check the connection between HAARP radiation and the occurrence of density perturbations and ELF electrostatic turbulence, it is also important to look at observations of DEMETER over HAARP when the transmitter is not operating. In the case on 2007-04-30 (Figure 3.7, Case 4), the HAARP HF transmitter has been off for 6 hours before, as well as during, the DEMETER satellite pass. Around 55° in latitude a large scale decrease in plasma density and increase in temperatures can be seen. After the large scale decrease you can also see a relatively weak large-scale increase in plasma density similar to the Case 1. In addition, there are smaller scale perturbations within large scale changes. ELF electrostatic turbulence is also clearly seen in the same region.

Generally, the form of the density variations observed above and around the HAARP region is substantially variable. However, the main feature of these variations—the density decrease of about an order of magnitude that lies within 50°–70° and extends for 5°–10° in latitude—is the most commonly observed large scale variation. Two additional examples shown in Figures 3.8 and 3.9 (Cases 5 and 6) can shed more light on the different forms of troughs observed. HAARP was not transmitting for these cases so that we see purely natural variations. In Case 5 as in Case 3
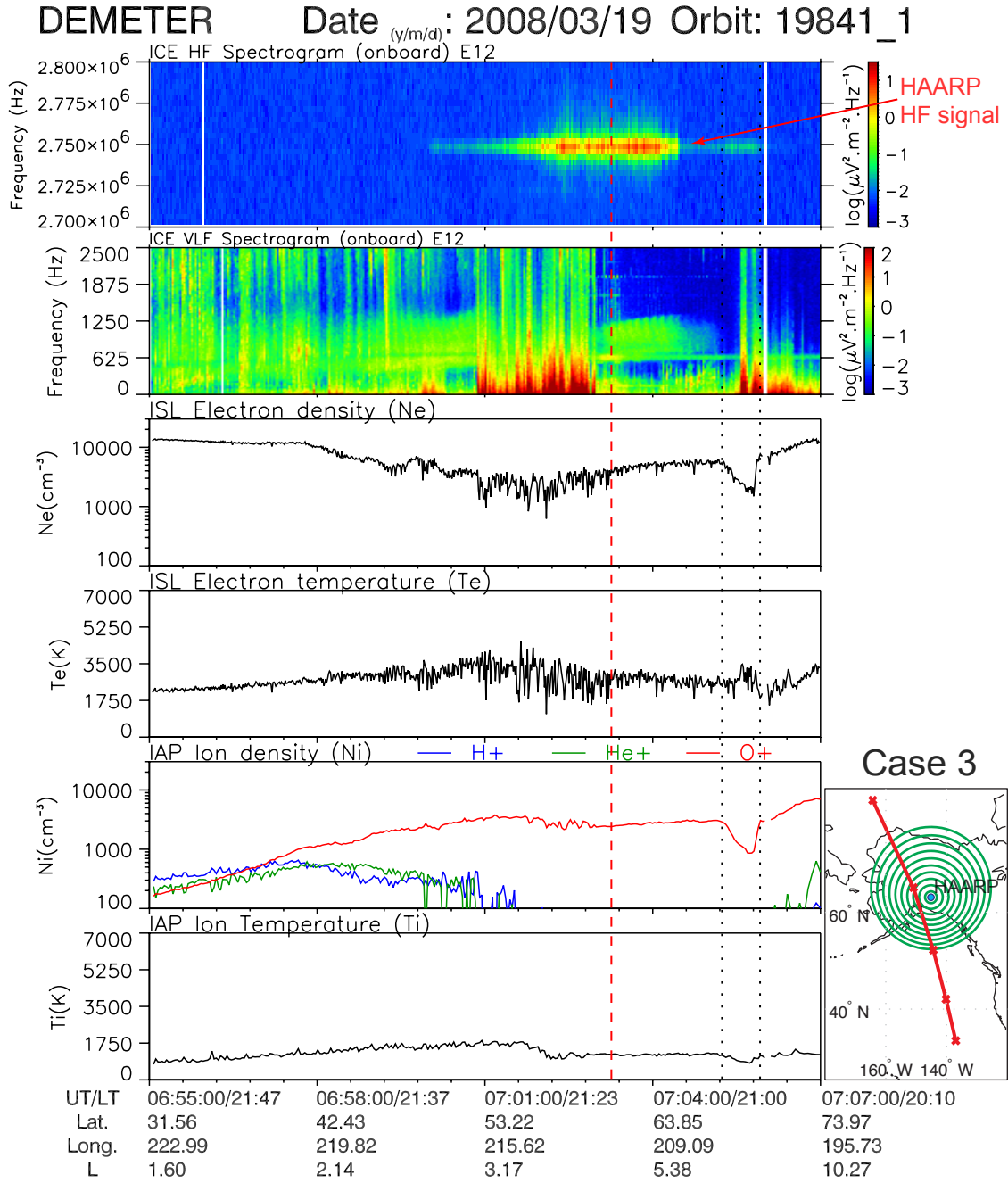
Figure 3.5: Panels are similar to those in Figure 3.1 . This is Case 3 on 2008-03-19. It is another example where density perturbations do not coincide with HAARP HF transmission. Here two types of density perturbations are observed as explained in the text.
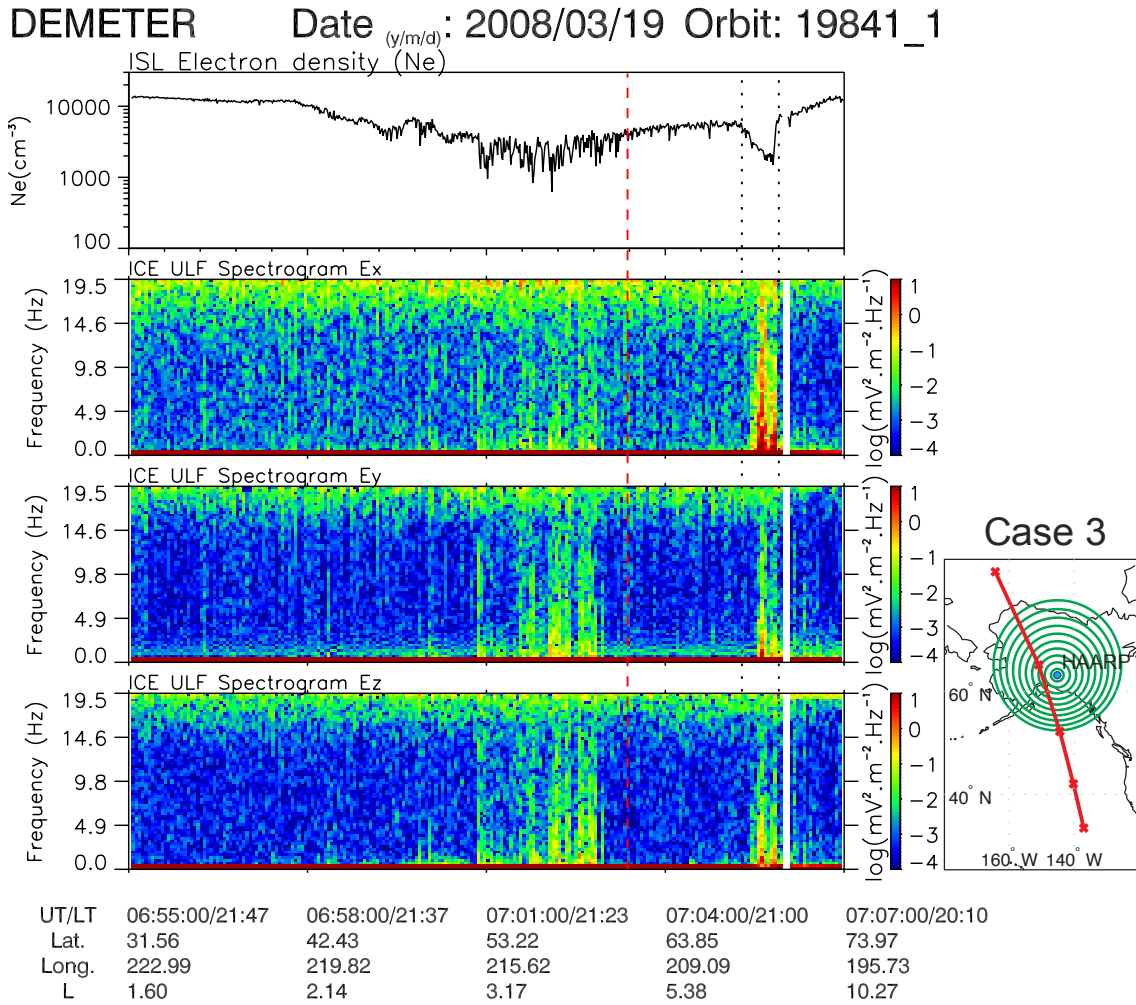
Figure 3.6: Additional data for Case 3 with ULF variations (three bottom panels) shown in spectrogram form. This demonstrates that ELF electrostatic turbulence is observed on DEMETER down to the DC *E*-field.
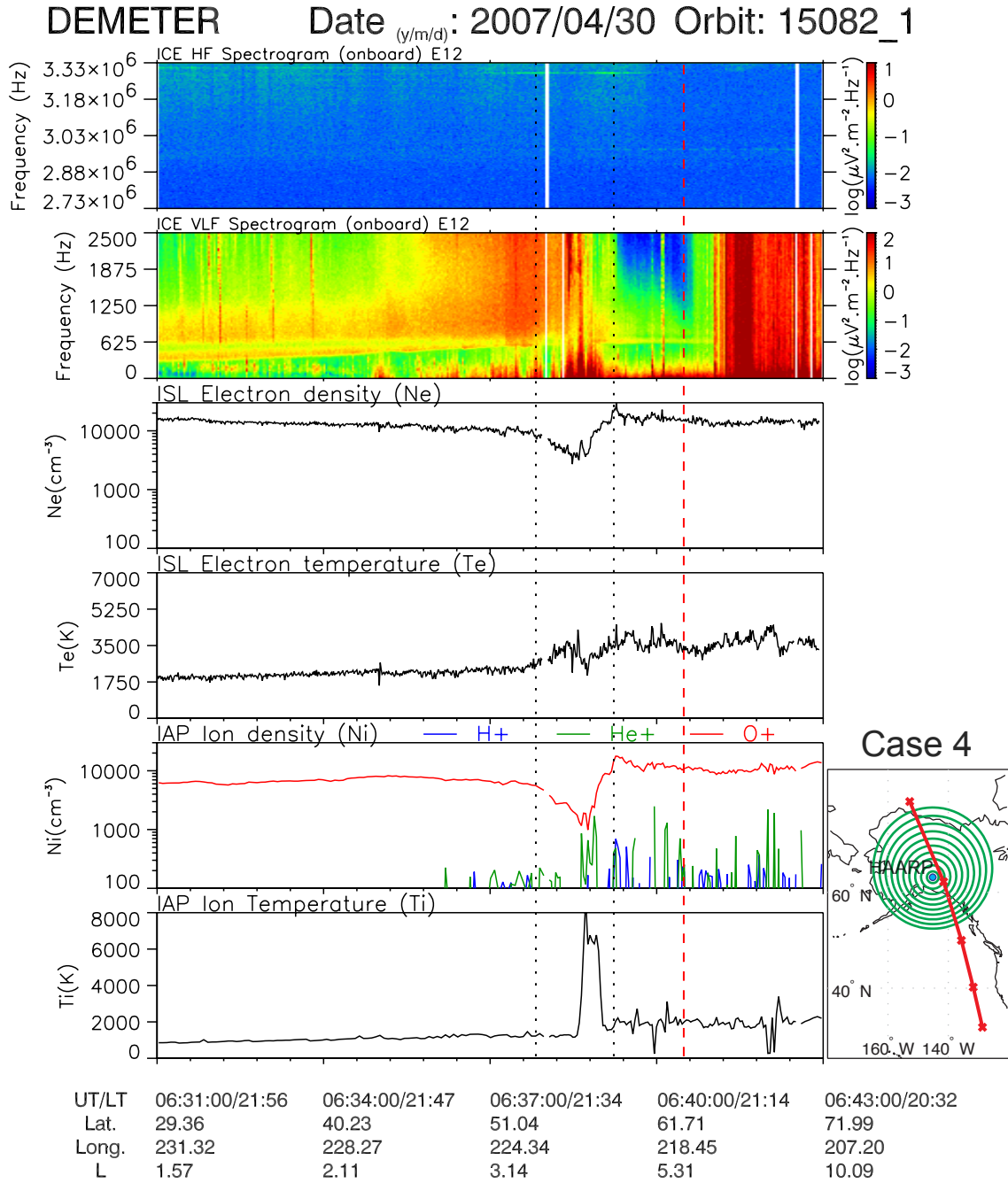
Figure 3.7: Panels are similar to those in Figure 3.1 . This is Case 4 on 2007-04-30. HAARP was turned off for 6 hours before the satellite pass. Perturbations associated with the main trough are clearly visible around the latitude of 55° and are displaced from the HAARP location.

we see at first small scale perturbations and then a pronounced trough in densities with small scale variations inside. In Case 6, the density trough is confined to a specific region that is similar to Case 1. It is interesting that in this example ELF electrostatic turbulence is not seen continuously within the trough. This probably is the result of the mostly smooth density within the trough. This supports previous observations that ELF electrostatic turbulence is first of all associated not with the trough itself but with commonly observed density variations within it [*Kelley*, 1972]. Similar situations were observed in several other cases.

3.2.3 Statistics

In total, 100 cases over the HAARP region have been analyzed. The summary of this analysis is presented in Table 3.2. The cases included in the statistics are those when the satellite is within a distance $d < 350$ km from HAARP. The cases are sorted by the conditions when they occur. The number of cases for each condition is shown in square brackets. The daytime passes of DEMETER over HAARP always happen from around 11:30 to 12:30 LT (20:30–21:30 UT), while nighttime passes occur from around 21:30 to 22:30 LT (06:30–07:30 UT). If the transmitter operated during the pass and at least several minutes before, then such condition is specified as HAARP ON. For a condition to be called HAARP OFF the transmitter was required to be off during the pass and for at least 30 minutes prior to the pass.

Table 3.2: Summary of observations: number of cases and specific cases.

Conditions		Results		
		No trough or no variations	Trough/variations not over HAARP	Trough/variations over HAARP
Daytime [20]	HAARP ON [12]	12	0	0
	HAARP OFF [8]	8	0	0
Nighttime [80]	HAARP ON [40]	8	11 (Cases 2 and 3)	21 (Case 1)
	HAARP OFF [40]	8	7 (Cases 4 and 6)	25 (Cases 5, 7, 8)

The results of a visual analysis of every case were classified into three categories depending on the electron density behavior. "No trough or variations" is assigned to
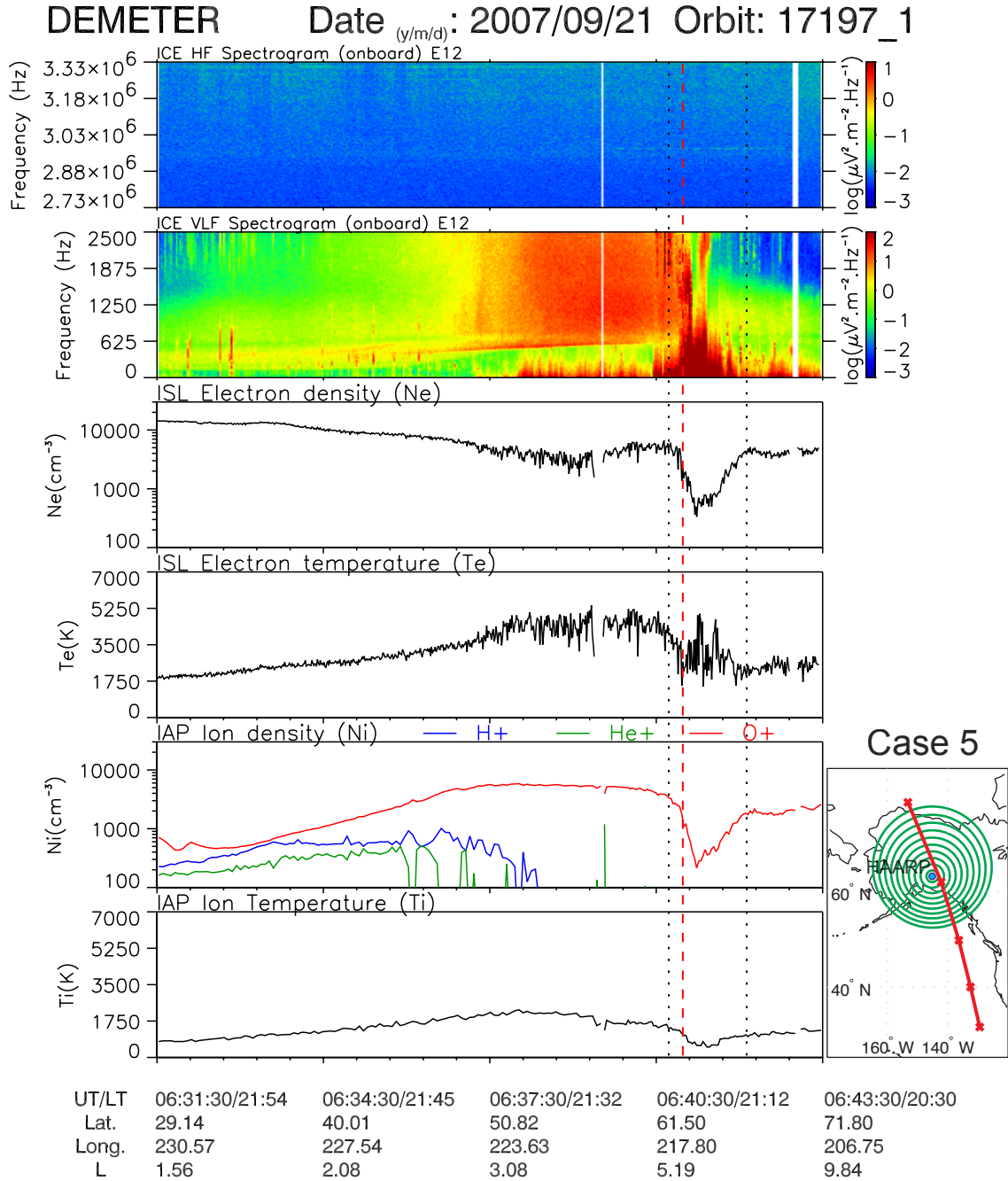
Figure 3.8: Panels are similar to those in Figure 3.1 . This is Case 5 on 2007-09-21. HAARP was turned off for 7 hours before the satellite pass. HAARP is located within the perturbations associated with the main trough.
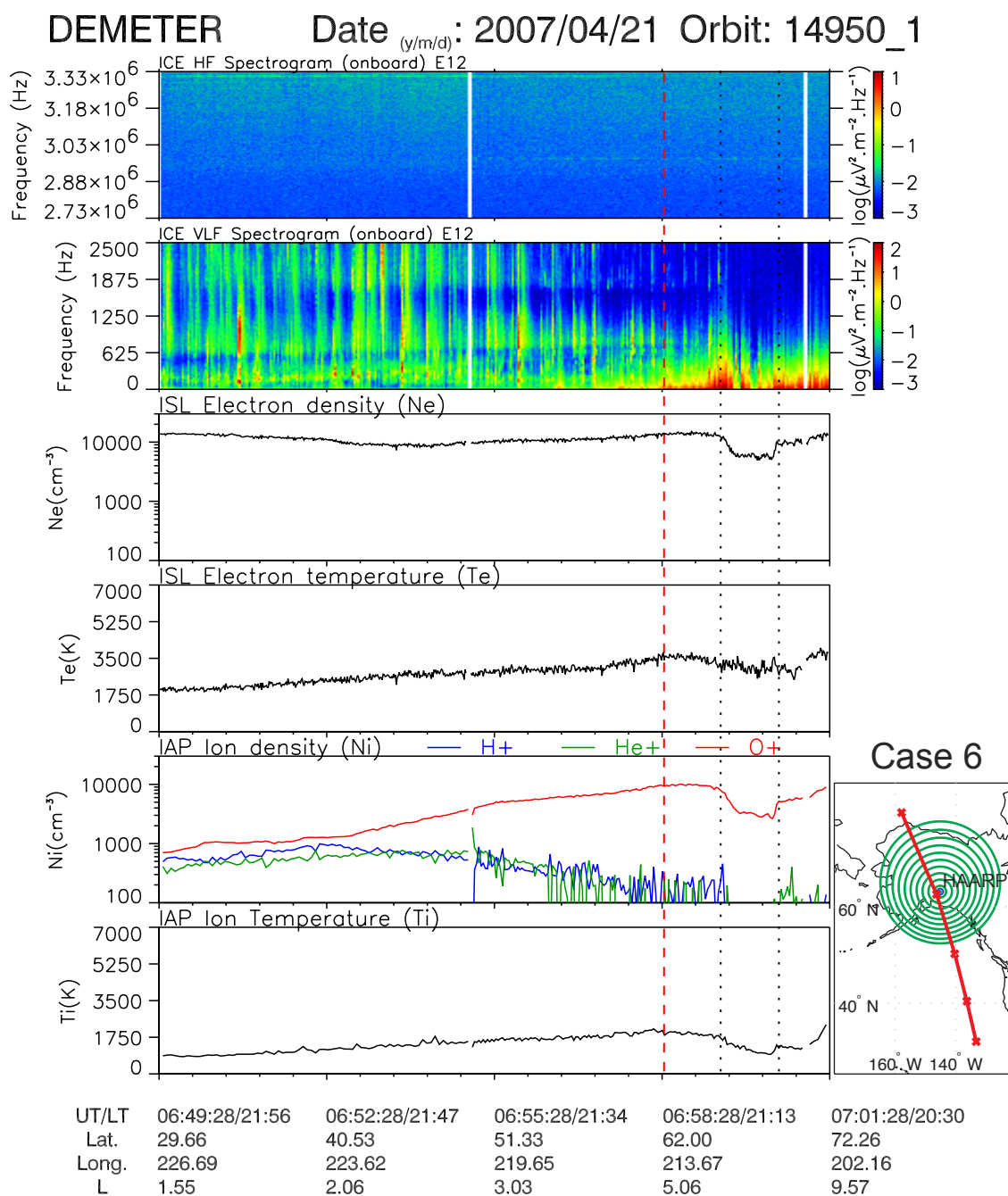
Figure 3.9: Panels are similar to those in Figure 3.1 . This is Case 6 on 2007-04-21. HAARP was turned off for 2 hours before the satellite pass. Perturbations associated with the main trough are displaced from the HAARP location.

the case when variations over HAARP are less than 30% or variations are smooth, i.e. the change occurs over a distance of more than 200 km. Such density behavior can be seen in Cases 1, 2, 4 and 6 below 50° latitude. For example, the small variation around 06:48:30 UT on 2007-07-29 (Case 1) or smooth variation from 06:52 to 06:58 UT on 2007-04-21 (Case 6) would be classified as "no variation". Cases fall into categories with "trough/variations" only when a more than 30% change in electron density is observed over a distance less than 200 km, as in the cases presented above. Sometimes the variations occur in a relatively confined region like in the regions marked with dotted lines in Case 1, Case 3, and Case 6. Sometimes the region is not well-defined from the electron density as in Case 2. In such cases, the location of the main trough is determined from the position of the corresponding ELF electrostatic turbulence. The perturbation is considered to be ELF electrostatic turbulence if it extends up to at least 300 Hz and the power spectral density exceeds $\sim$10 μV^2·m^{-2}·Hz^{-1}. A small amount of cases in which neither of these approaches work were not included in the analysis. Both of the types of variations are categorized as "trough/variations". If the closest approach to HAARP occurs within a variation region then the case is put in the category "over HAARP". There are cases when due to variations inside the trough, ISL data processing does not work properly and produces no acceptable results (Figure 3.10). In this case an interpolation of only a few reasonable data points is made, and as a result the electron density is usually recorded as a constant equal to 1000 cm^{-3}. Those cases were also classified as ones with variations.

The most important conclusion which follows from Table 3.2 is that HAARP operation does not correlate well with large scale density or temperature variations over HAARP. For daytime, such variations have not been observed at all, whether HAARP is ON or OFF. For this reason, the statistics were limited to only 20 cases in the daytime. For nighttime, large scale variations appear in 32 cases out of 40 when HAARP is ON and in 32 out of 40 when HAARP is OFF. Moreover, there are 21 cases with variations over HAARP when HAARP is ON versus 25 cases with variations over HAARP when HAARP is OFF. This distribution clearly suggests that the variations are not caused by HAARP.

We can also see that the region above HAARP is disturbed in more than half
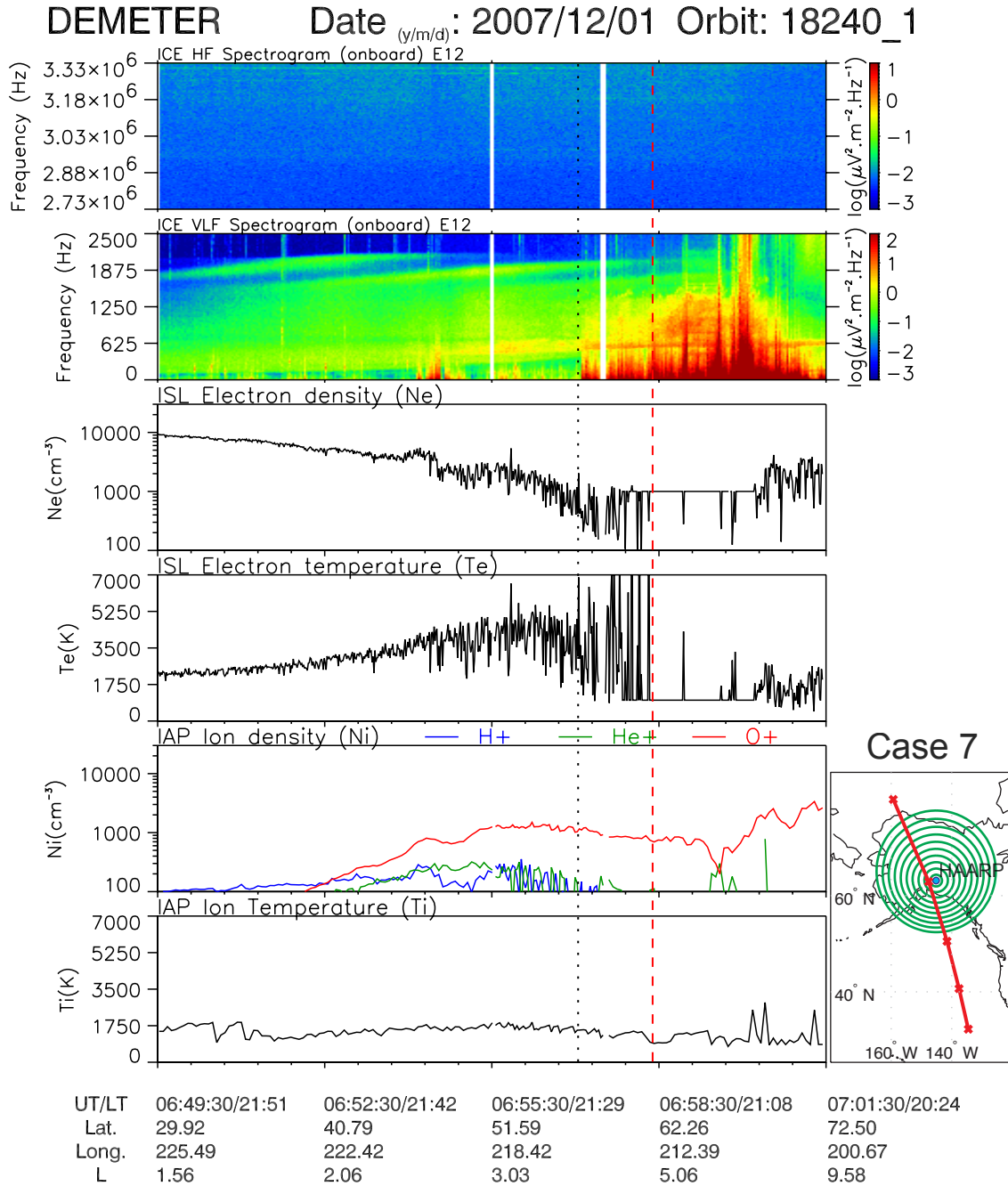
Figure 3.10: Panels are similar to those in Figure 3.1 . This is Case 7 on 2007-12-01. HAARP was turned off for many days before the satellite pass. The flat response in electron density is produced due to the ISL instrument limitations and not due to HF heating.

of the number of cases at nighttime. However, in many such cases the large-scale variations occupy the whole region of high latitudes, which the region above HAARP is just a part of. That is why there are not many cases in the "Trough/variations displaced from HAARP" category since in such cases variations should be localized but not over HAARP.

3.2.4   High-Latitude Regions of Non-HAARP Longitude

Since the main emphasis of the current work is devoted to the HAARP region, we discussed here in detail data from this region. However, the observations of the main ionospheric trough on DEMETER are not unique to the region above HAARP. In Figure 3.11 DEMETER observations over the same latitudes and different longitudes are presented for comparison. In general, the structure of the trough and ELF electrostatic turbulence is similar to the cases presented before for the region over HAARP.

3.3   Discussion and Comparison with Other Experiments

In the work of *Milikh et al.* [2008] two cases were presented in their Figures 3 and 4 in an attempt to show DEMETER observations of ionospheric ducts. It is clear that in both cases the main ionospheric trough is present during the observations. We can see sharp minima from 06:54:30 to 06:55:00 UT on 2007-04-24 and from 06:45:30 to 06:47:10 UT on 2007-08-01. The authors claim that "both the ion temperature and O^+ density rise due to the HF-heating by about 60-70%" and that there is "a duct associated with the density gradient between 06:51:00 and 06:51:30" on 2007-04-24. Also they refer to "a series of few percent short length ducts between 06:52:00 and 06:53:30". Our observations demonstrate that similar gradients and short length ducts can be observed by DEMETER when HAARP is OFF such as in Cases 6 and 7 of the current work. It is typical to see irregularities of various scales around the trough, and in such situations HAARP might have affected the plasma density but it is not possible to conculisively assert this based only on satellite observations because
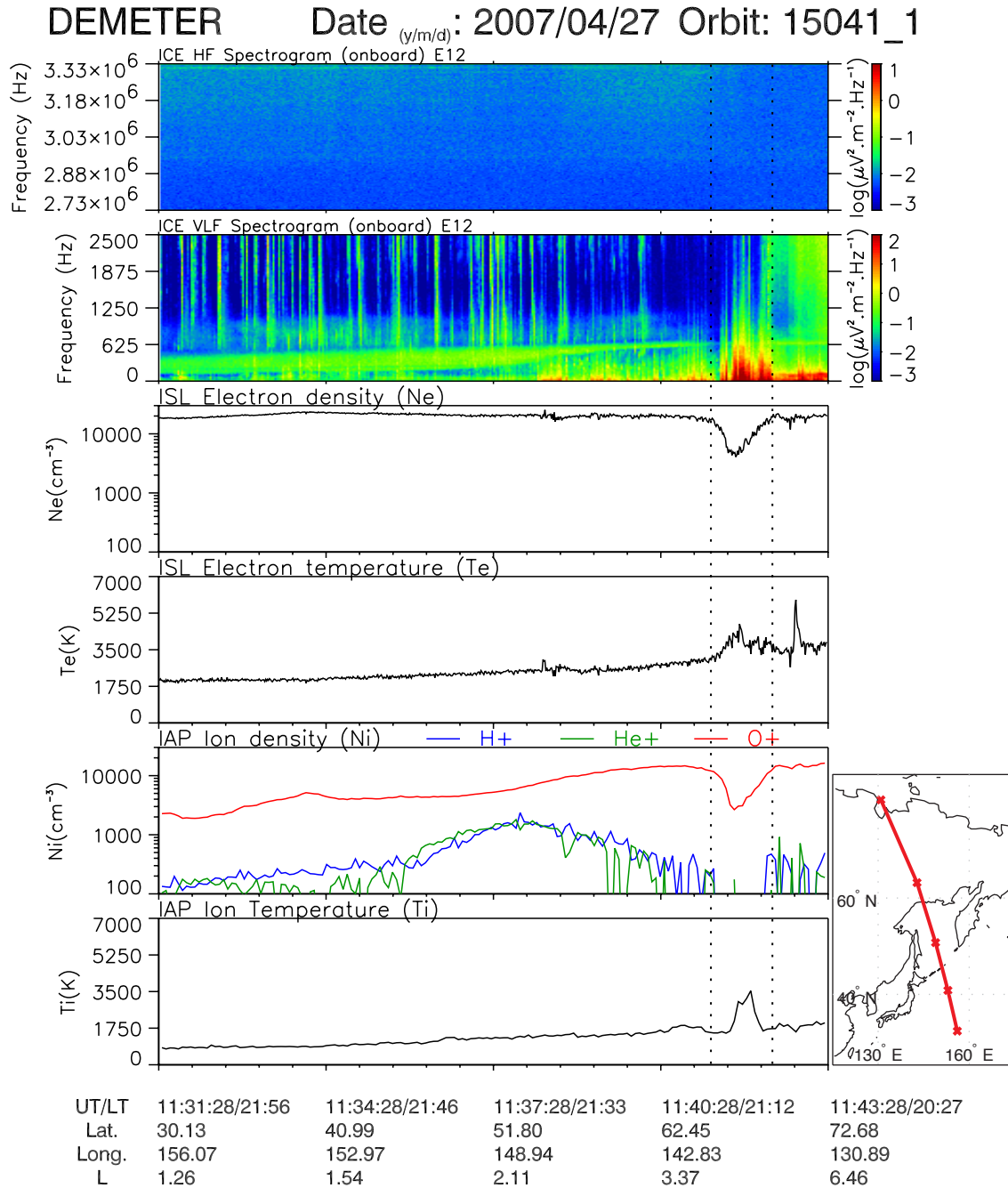
Figure 3.11: Panels are similar to those in Figure 3.1. Here the observations of the main trough in a region other than over HAARP are shown.

of the possible presence of the ionospheric trough.

In *Wong et al.* [2009] it was claimed that an electron hole was created by HIPAS HF transmitter in the cases presented in Figures 1 and 2 of that work. However, it appears that in those cases we see only an instrumental effect in the region of large density variations which is typical of high latitudes. The same instrumental effect of constant density at the 1000 cm^{-3} level is presented in Figure 3.10. It was observed in several cases when HF transmitters were OFF.

From the observations presented here it is seen that at high latitudes large-scale irregularities are very common at nighttime. Sometimes they occur together with a clear trough in plasma density, but this is not the case all the time. The most important implication for HF heater related research is that such natural irregularities would often prevent the detection of effects such as ducts or holes created by the HF heater. While we do not mean to imply that such effects cannot exist and cannot be detected, it is obviously important that natural effects should be taken into account in such experiments. For instance, one can try to select times of observations when the ionospheric density is relatively undisturbed. Unfortunately, daytime is not the best choice because HF waves do not usually penetrate through the higher density ionosphere during the day. However, as seen from statistics there also exist days without irregularities over HAARP during nighttime.

Plasma convection at high latitudes should also be taken into account during experimental observations of density variations. It is well-known that at high latitudes the typical speed of plasma flow in the F layer is several hundred m·s^{-1} in the horizontal direction [*Hunsucker and Hargreaves*, 2003, p. 228]. Thus, if some density variations in the F layer are created by an HF heater in a region with a horizontal extent of 100–200 km, then in about 10 minutes the plasma with density variations moves away from this region if the heater is turned OFF. (Such is the reason why for statistics with HF heater turned OFF we included only cases for which the HF heater is OFF for at least 30 minutes before the satellite pass.) In other words, for an effect to be observed on a satellite in the F layer it should have a time scale of development of no more than 10 minutes, and averaging over longer time scales would also not be beneficial.

Finally, it is supposed that in cases similar to Case 1 when the trough location coincides closely with the location of the HF maximum on a satellite, the HF may in fact have been guided by a natural density duct to the satellite. For instance, for Case 1 the region of HF detection on the satellite is unusually confined. Most often the region of HF detection spreads over longer distances, as seen from other cases. However, such confinement of HF to the trough region does not always happen. Another strong case that supports the theory of HF guidance by a natural density duct is presented in Figure 3.12. In this case HF waves were also detected in a confined region inside the trough, and the trough was not directly over HAARP but about $5°$ lower in latitude. The HF beam was actually directed along magnetic field line which crosses DEMETER altitude at $61°$. However, the HF signal is seen at latitudes from $55°$ to $57°$ where the trough is located at the time of observation.
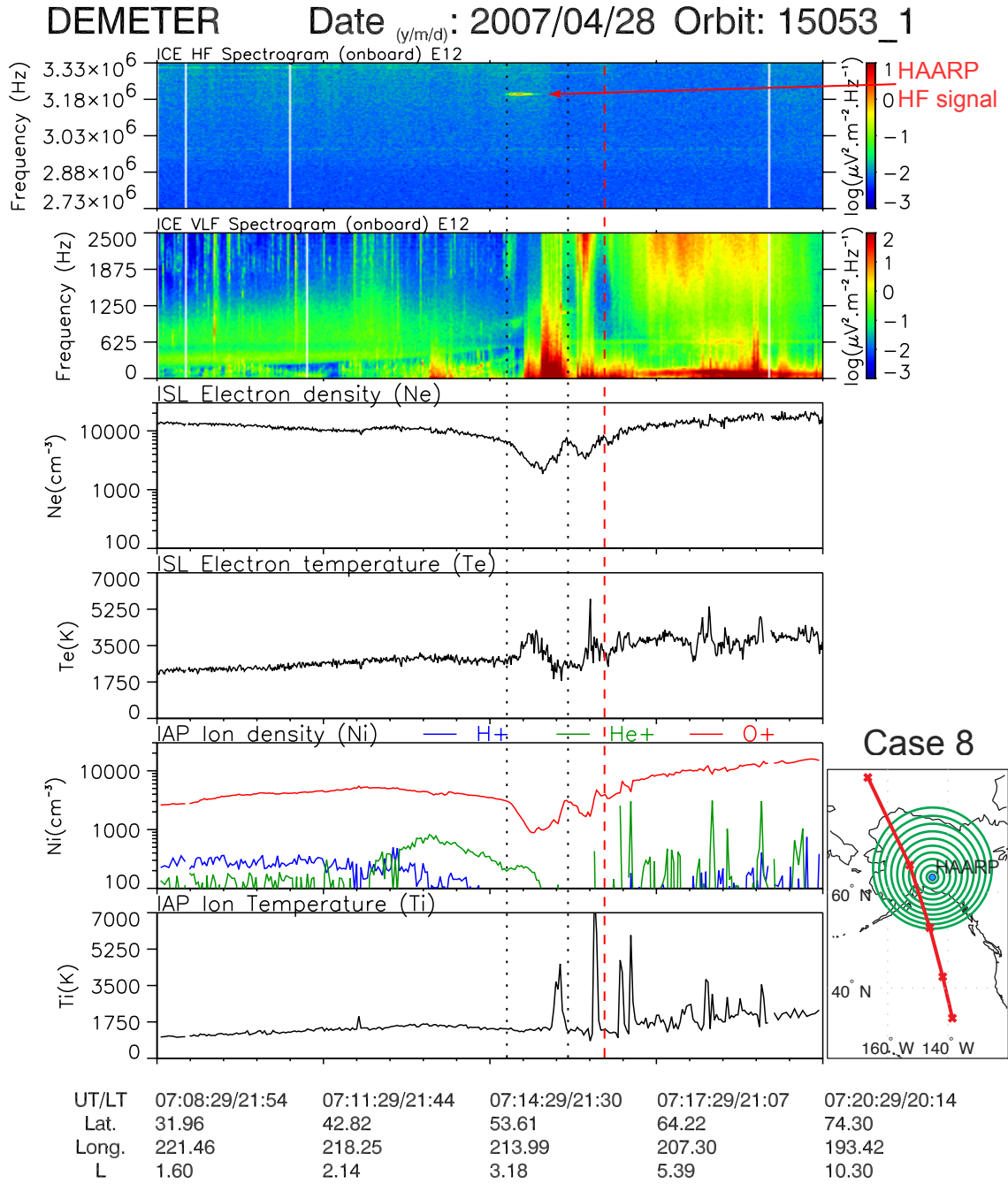
Figure 3.12: Panels are similar to those in Figure 3.1. Here the observation of the HF signal from HAARP coincides with the location of the main trough and not with the location of HAARP, which is about 5° higher than that. This suggests guiding of HF waves by the trough.

Chapter 4

Case Study Observations over HAARP

DEMETER satellite observations above the HAARP HF transmitter constitute the basis of this dissertation. In previous chapters we discussed the basic structure of the environment above HAARP and also the details of the high-latitude environment. This knowledge makes it easier to understand the features of ELF wave propagation. However, the order in which we present our findings is not exactly the same in which those findings were discovered. Our learning process evolved in the course of multiple experiments, usually grouped in the campaigns as described in Chapter 2.2. Initially we learned from specific cases of DEMETER passes over HAARP. This knowledge enabled us to improve experiments over time and helped us to recognize the repetitive features in the observations. Also numerical modeling was developed during the course of the experimental observations. The modeling primarily helped in the physical interpretation of observations. However, the experimental studies would not be complete without an overall look at data. Such aggregated analysis of multiple cases was done after all the data were collected, and this helped to confirm and refine the things we learned from the case studies. Eventually, several case studies can describe the basic physical features of wave propagation if one is already cognizant about correct interpretation of such observations. For these reasons, we start our description with several representative case studies for various natural conditions and point out

to the reader the important observed features. A specific case makes physical concepts easy to understand at the beginning. After that we present aggregate studies in which similar features can be seen, but in a different and more rigorous type of analysis.

Portions of the results reported in this chapter were published in *Piddyachiy et al.* [2008].

4.1   HAARP Transmission Format

For ELF experiments with HAARP, the HF carrier frequency was in the range of 2.75–3.25 MHz to provide maximum heating in the D-region of the ionosphere [*James et al.*, 1984]. The lower the frequency in that range, the more HF power will be absorbed in the D-region of the ionosphere, which in turn leads to better heating and generation for ELF frequencies. 2.75–3.25 MHz is the primary frequency range for which HAARP transmitter was designed and in which it is the most efficient. 2.75 MHz was unavailable for the first year of experiments with DEMETER and 3.25 MHz was used instead. The difference between 2.75 MHz and 3.25 MHz is negligible in comparison with the daily variations of the ionospheric critical frequency and the electrojet intensity. The critical frequency of the D-region is hard to measure reliably, but for the sense of variability, the F2 layer critical frequency is shown in Figure 4.1 as measured by the Digisonde at HAARP. Also, the HF wave is polarized in the extraordinary (X) mode to provide the maximum ELF radiated power [*Kapustin et al.*, 1977; *Stubbe et al.*, 1982].

The HAARP HF frequency is Amplitude Modulated (AM) with ELF frequencies in order to study the generation and propagation of ELF waves. Several modulation formats are presented in Table 4.1. For an estimation of the spatial distribution of ELF power at the altitude of the DEMETER satellite, a special ELF pattern of HAARP modulation was devised. This pattern is called "Default" in Table 4.1 and is also presented graphically in Figure 4.2. The periodicity of the pattern is 4 s which corresponds to a DEMETER horizontal travel distance in the ionosphere of 31 km. Within each 4-s sequence, two 1-s long tones of 613 and 2011 Hz and a 2-s long ramp
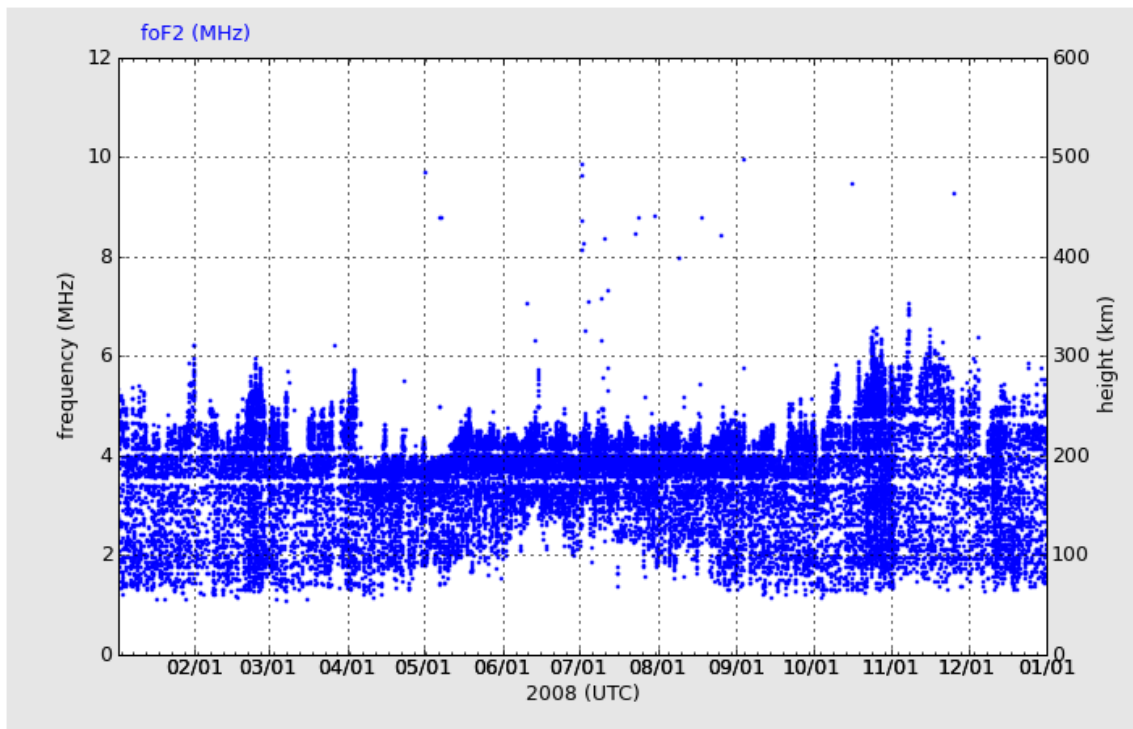
Figure 4.1: Variability of ionospheric critical frequency over HAARP. As an example the whole year of 2008 is shown. The data are collected by an HF ionosonde at HAARP. The critical frequency of the F2 layer is one of the most important parameters of the ionosphere related to F2 layer plasma density. The height of the F2 layer maximum (y-scale on the right) is also inferred from ionosonde measurements.

Table 4.1: Formats of ELF modulation frequencies transmitted by HAARP

Dura-tion, s	Default pattern $f(t)^a$, Hz	Dura-tion, s	Test pattern $f(t)^a$, Hz
1	613	1	510
1	2011	1	820
2	$1000t$	1	1225
		1	1510
		1	1875
		1	2125
		1	2375
		1	3165
		1	3365
		1	4365
		10	$200t + 20\sin(10t) + 400$ (snake ramp)
		5	$500t + 500$
		1	5 chirps^b starting at 1000 Hz
		1	1225
		1	5 chirps^b starting at 1500 Hz
		1	1875
		1	5 chirps^b starting at 2000 Hz
		10	$100t + 30\sin(3.33t) + 1100$ (snake ramp)
		10	$200(t - 40) + 500$
		10	$200t + 40\sin(5t) + 400$ (snake ramp)

^{a} – In each interval t starts with 0 s.
^{b} – Duration of each chirp is 0.2 s. It is described as $f(t) = f_0 + 1000\sqrt{5t}$, where f_0 of the first chirp in a sequence is the starting frequency in the table which decreases by 70 Hz for each next chirp.

of 0–2011 Hz are transmitted. The 4-s sequence is repeated throughout the whole DEMETER pass over HAARP. The precise ELF frequencies were chosen to avoid interference from power line harmonics [*Helliwell et al.*, 1975]. The choice of the pattern is a compromise between spatial resolution, the number of frequencies, and the averaging time. First, let us consider averaging time. Previous test experiments showed that a tone (or pulse) should be about 1 s in duration in order to have enough time averaging for reliable measurement of the signal strength as it reaches the satellite. The signal amplitude within a pulse can be quite variable because of scattering from ionospheric plasma density irregularities resulting in multipath propagation to a specific location. The multipath effect is largely minimized with 1-s averaging but most probably not completely eliminated in cases of very irregular plasma density, as seen later.

Now, let us consider the length of the ELF pattern sequence. The length cannot be made too short to measure at least two tones and one ramp, but it cannot be too long because of the need to have enough spatial resolution, which is selected herein to be 31 km. Because of scattering, the ramps are not useful to measure spatial signal strength distribution at every frequency between 0 and 2011 Hz. The time duration of any reasonable frequency band selected from the ramp is too short. However, averaging between ramps over some region may give the overall frequency dependence of ELF wave propagation into the ionosphere.
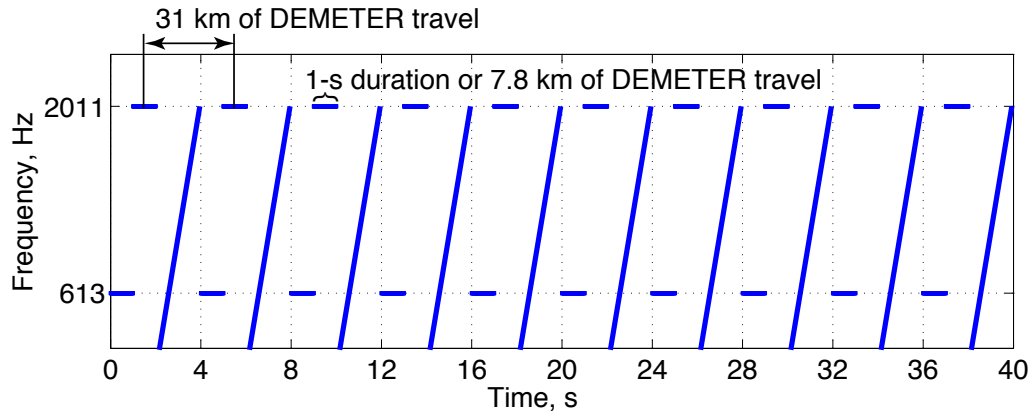
Figure 4.2: Default ELF pattern of HAARP modulation.

An example of the default ELF pattern reception on the ground and on DEME-TER is presented in Figure 4.3. The data are presented in the form of a spectrogram from 200 to 2500 Hz and the map of the considered DEMETER pass. The red part of the DEMETER trajectory on the map is the region in which the data shown in the spectrogram was acquired. It is seen that the signal on the ground is stable in strength over the duration of DEMETER pass and shows only weak variations within the 1-s duration of the pulse. On DEMETER, on the other hand, the variations of two time scales are clearly visible. First, the signal amplitude increases as the satellite moves closer to HAARP. This is the type of variation we are most interested in. Other types of variation are seen within 1-s pulses. As mentioned above they appear to be related to density irregularities on the path of propagating ELF waves. In addition to the signal transmitted by HAARP, the harmonics of the signal are also present. The content of harmonics is different on the ground and in space.
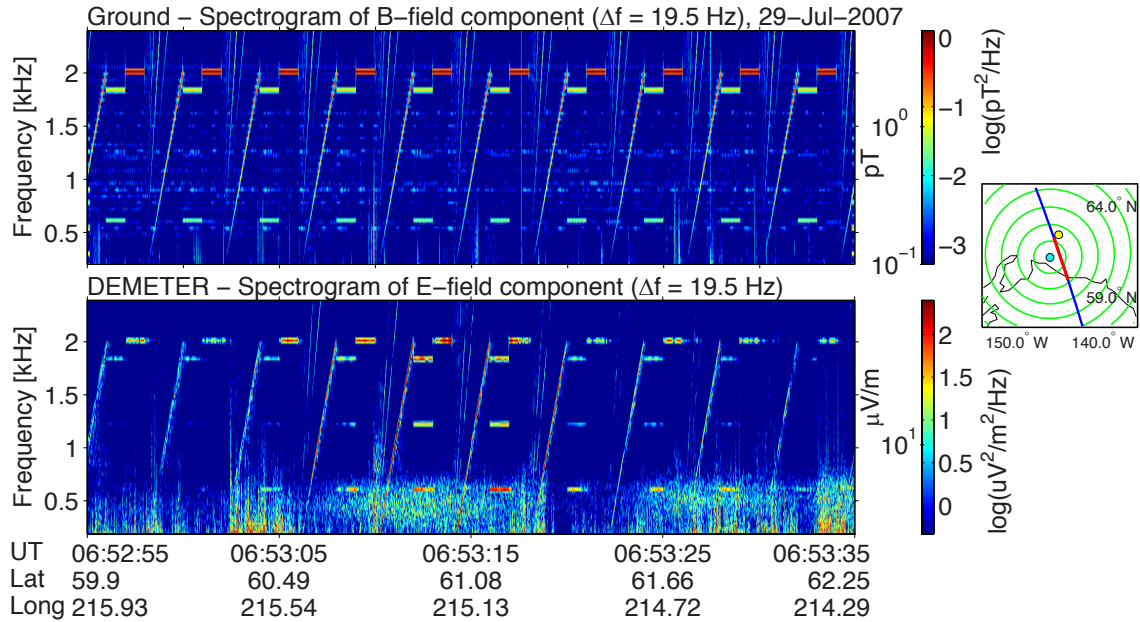
Figure 4.3: Observations of the default ELF pattern on the ground and on the satellite.

Another pattern labeled "Test pattern" in Table 4.1 represents a rich set of different ELF/VLF signal types and frequencies. This pattern can be used to test the

effectiveness of ELF generation and propagation with various frequencies and shapes of modulation at one pass. The disadvantage of this format is that it does not allow the study of the spatial dependence uniquely for a given ELF frequency because it lasts for 1 minute.

It should be mentioned that other ELF patterns were also used, but the default 4-s pattern was used consistently throughout four years of HAARP/DEMETER experiments. Totally six 1-s tones were employed in default pattern: 547, 565, 571, 613, 1973, 2011 Hz. The first four and the last two can be bundled together in aggregate studies.

4.2 Nighttime Conditions

One of our representative observations occurred on 2009-03-14. The DEMETER pass took place during local nighttime, and the part of it between 06:45:41 and 06:47:57 UTC is shown in Figure 4.4. This time period corresponds to 21:10–20:52 LT and 20.07–19.41 MLT. The satellite passed within 100 km of HAARP as seen at the bottom part of the figure. The default transmission pattern as in Figure 4.2 is used. The band of frequencies from 1.9 to 2.1 kHz is shown in a spectrogram at the top of the figure. The spectral analysis is done with $\Delta f = 4$ Hz. If magnified, most 2011-Hz pulses occupy 3 bins in frequency that corresponds to a 12-Hz bandwidth. The signal strength over this bandwidth for every pulse is shown in the middle panel of the figure.

In Figure 4.4 it is seen that one pulse has a distinctly stronger electric field strength of 75 μV·m^{-1} than other pulses of the pass. From the spectrogram it is also obvious that the field is higher for the narrowband pulse, meaning that it is not associated with any type of interference or noise. The close proximity of strong field to the position of magnetic field line coming from the source of ELF waves in D-region suggests the presence of a column of strong signal coming from the the source. This column is the one which is also referred to as the Region 1 throughout this work, and it was first observed in early experiments via case studies [*Piddyachiy et al.*, 2008]. Most probably in the present case the satellite passes through the periphery of the

Figure 4.4: Spectrogram and intensity of the electric field on DEMETER for a representative night time case. The corresponding location of DEMETER with respect to the magnetic field line passing through the ELF source is shown at the bottom. Three regions of ELF field strength can be identified.

column, since only one pulse is observed and the strength of the pulse is lower than in some other observations.
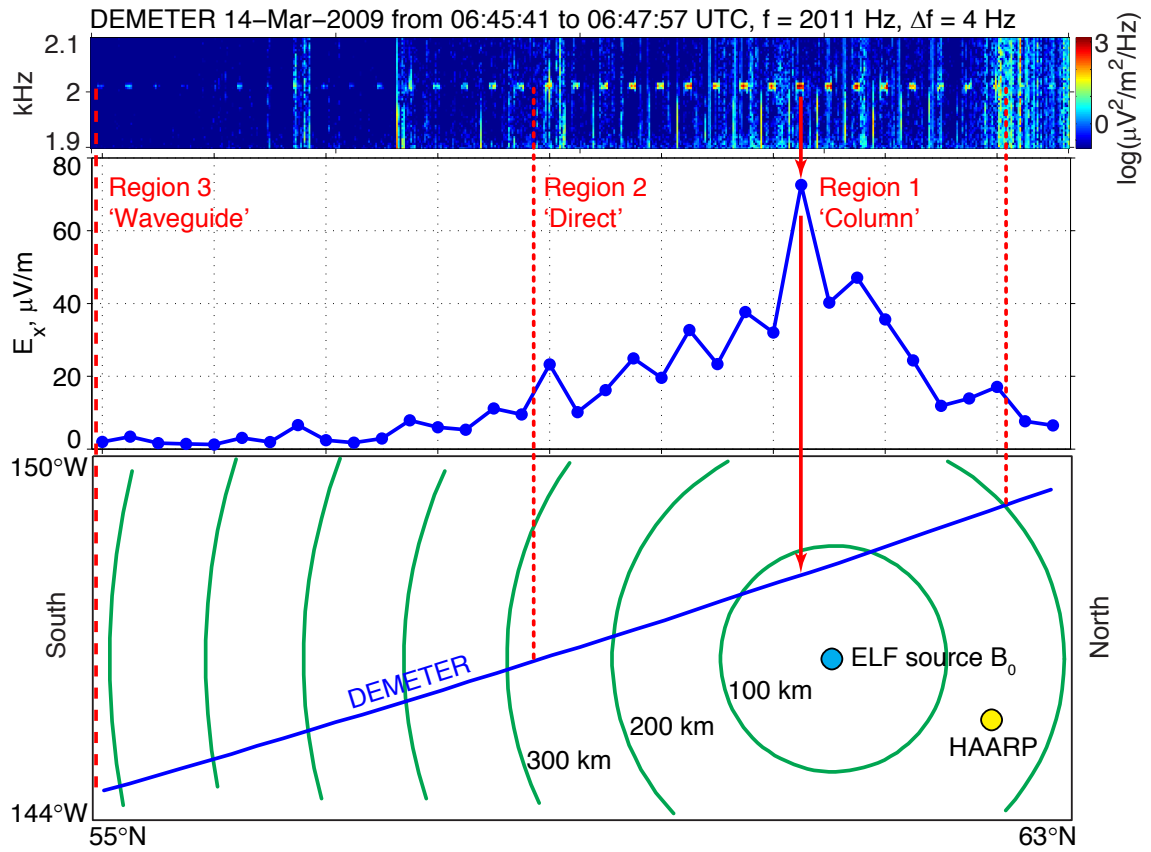
The same observation allows us to recognize Region 2 of the signal strength above HAARP. In the presented case the electric field in this region is characterized by the strength of 10–50 μV·m^{-1}. The rate at which the electric field drops with distance from its peak strength is about 0.15 μV·m^{-1}·km^{-1} at the southern part of the path and about 0.4 μV·m^{-1}·km^{-1} at the northern part. These values constitute the basis on which Region 2 is distinguished from Region 3. In Region 3 the field is below 10 μV·m^{-1}, and the rate of field decrease is about 0.02 μV·m^{-1}·km^{-1}, which is approximately an order of magnitude less in both metrics. For the 2009-03-14 case it is possible to visually distinguish in the spectrogram a signal up to 700 km from the $\mathbf{B}_{0,\text{source}}$ to the south. The northern part of the pass in this situation is affected by natural noise and no signal is seen beyond the plotted region. The names of regions ("Direct" and "Waveguide") are discussed below together with the physical interpretation of wave propagation.

The 01 March 2007 pass is one of the closest satellite passes near HAARP and is another example of nighttime observations (Figure 4.5). The closest horizontal distance to $\mathbf{B}_{0,\text{source}}$ is $d \simeq 50$ km. The three panels show spectrograms for the period from 07:03:50 UTC to 07:05:30 UTC. This corresponds to 21:20–21:04 LT and 20.07–19.46 MLT. The top panel is a spectrogram of the East-West horizontal component of the B field measured at Chistochina. The middle and bottom panels are the spectrograms of the horizontal components of E and B fields respectively from DEMETER. At this time Kp is 3^- and AE is 171 nT. The ELF modulation pattern used for this pass is the one called "Test" in Table 4.1. The signal at Chistochina exhibits no significant changes in time and exhibits a high signal to noise ratio enabling the recognition of the entire pattern transmitted, with higher harmonics also visible in some cases. During this DEMETER pass, HIPAS HF transmitter was also coincidentally operating, producing long (10, 20 or 30 s) tones around 1 and 2 kHz.

Examination of the frequency-time ramps and pulses of different frequency indicates that as the frequency increases from 0.5 to 2 kHz the power of the signal on the ground increases by about one order of magnitude. The ramps are short enough
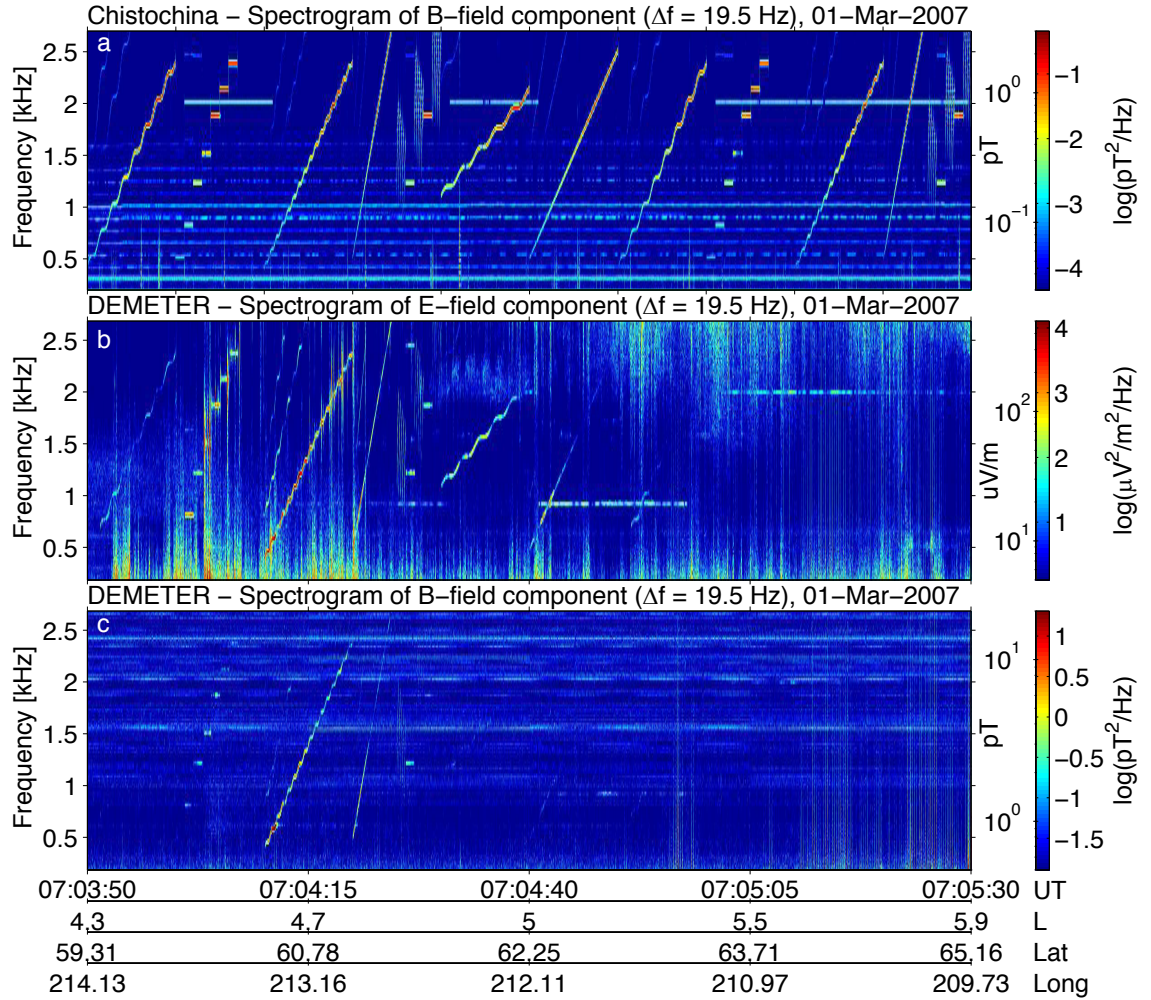
Figure 4.5: Simultaneous spectrograms of the ELF fields during the DEMETER pass on 01 March 2007. (a) East-West horizontal B field component on the ground in Chistochina. (b) A horizontal component of E field on DEMETER. (c) A horizontal component of B field on DEMETER. The figure demonstrates the different frequency dependence of the received signal on the ground and on the satellite.
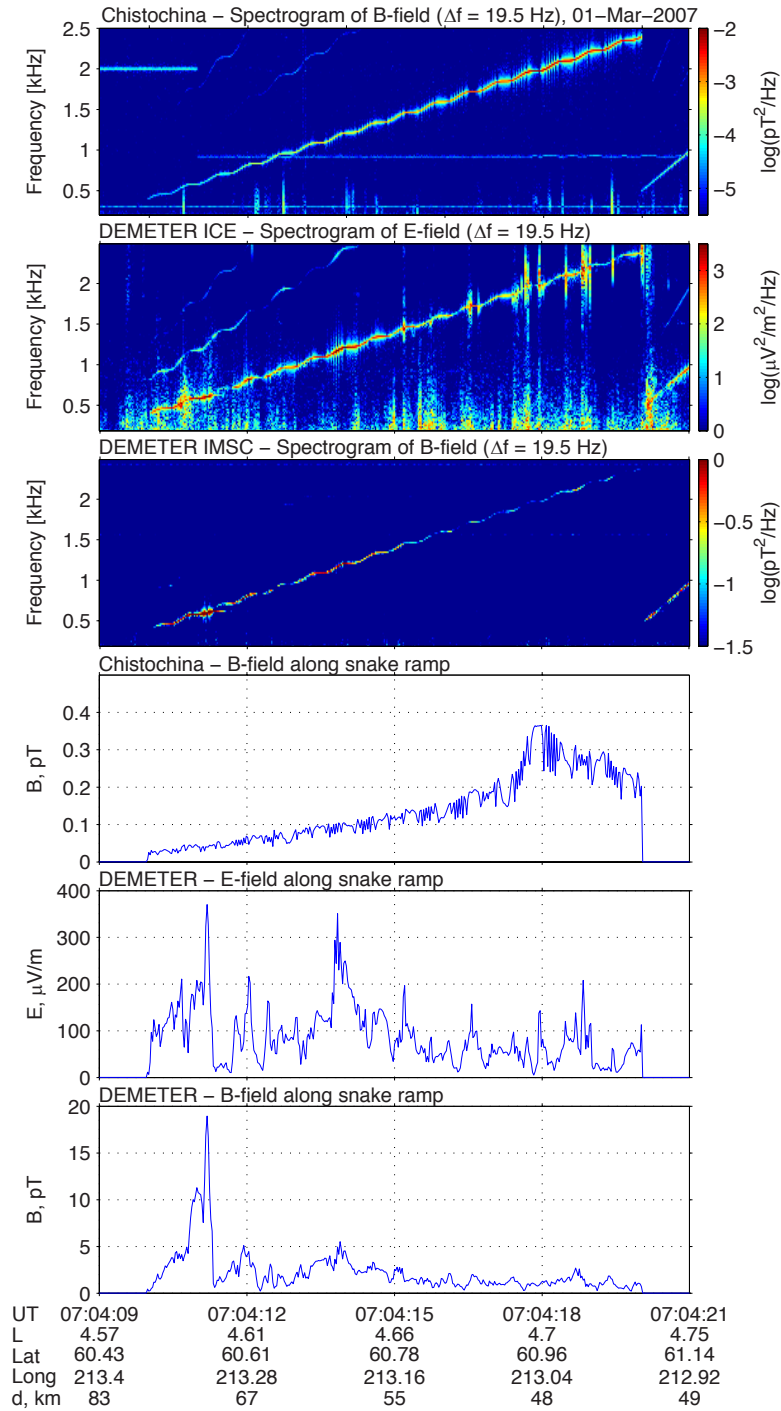
Figure 4.6: The case on 01 March 2007 zoomed and plotted with field strengths along a snake ramp.

so that any natural variations in the auroral electrojet strength can be ignored and the observed variation can be attributed solely to the dependence of ELF generation and propagation on frequency. It is known that the ELF signal on the ground exhibit maxima near multiples of 2 kHz which are attributed to waveguide resonance effects [*Stubbe et al.*, 1982; *Rietveld et al.*, 1989]. The signal strength on DEMETER first of all depends on the distance of the satellite from the magnetic field line of the heater. As the satellite moves northward, it first passes a region of high field near HAARP and then a similar one near HIPAS. The signal to noise ratio on DEMETER for the E field is higher than for the B field, so that the signal in the E field spectrograms is visible over a larger region. Actually, it is a general rule that the E field on DEMETER is easier to distinguish from the noise than the B field, especially for low signal levels, because of the relatively higher sensitivity of the E field receiver and antenna systems. The dependence of the signal strength on distance in this type of observation is intertwined with the dependence of generation efficiency on the ELF frequency. Figure 4.6 shows in detail the most interesting part of the pass when DEMETER is in close proximity to the HAARP heated spot. The first three panels are magnified versions of the spectrograms in the Figure 4.5, while the last three panels represent linear plots of field amplitudes calculated along the main harmonic of the snake-ramp. We can see that the trend of the frequency dependence observed on the satellite is generally opposite to that seen in ground-based data, and that the amplitude in space is more variable. The most interesting features are two peaks in the E field and corresponding high and low peaks in the B field amplitudes. The first peak of $E = 367$ μV·m^{-1} and $B = 19.2$ pT at 07:04:11.19 UTC occurs at a distance of 73 km. The second peak of $E = 366$ μV·m^{-1} and $B = 5.8$ pT at 07:04:13.86 UTC occurs at a distance of 61 km. The frequencies at which the peaks occur are 605 Hz and 1172 Hz respectively. It should be noted that the peak E-field amplitudes are observed before the satellite reaches the closest point to the HAARP field line (07:04:19.59 UTC) indicating that the region of maximum signal is slightly displaced southward. This observation qualitatively confirms AUREOL-3 measurements over the Tromso HF heater [*Lefeuvre et al.*, 1985] of a 3° southward displacement at 1900 km altitude ($d = 200$ km). The B-field intensity on the ground

is ~ 0.1 pT during the E field peaks on DEMETER, which is lower than the average values observed at Chistochina at this frequency.

The electron density measured on the satellite is 4×10^3 cm^{-3}. The other 2 components of E and B up to 1250 Hz were also measured on DEMETER at levels comparable with the components shown in Figures 4.5 and 4.6. It should also be noted that the proton gyrofrequency on DEMETER above HAARP is $f_{c_{H+}} = 636$ Hz which is close to the frequency of the first maximum. However, Oxygen is the dominant ion at the time of the observations ($N_{O+} = 4 \times 10^3$ cm^{-3}, $N_{H+} < 10$ cm^{-3}) so that Hydrogen influence on waves propagation should be minimal. Also, if the first maximum is due to the decrease in group velocity as the waves approach the point of absorption, the polarization of these waves should be circular left-hand, but it was calculated using the method of *Santolík et al.* [2006] that the waves in the maximum have close to linear polarization (the ratio of the axes of the polarization ellipse is from 0 to 0.2). The waves in the second maximum exhibit circular right hand polarization as expected for frequencies above $f_{c_{H+}}$. The calculation of wave normal angle using the method of *Santolík et al.* [2006] gives $\Theta \simeq 110°$–$150°$ below $f_{c_{H+}}$ and $\Theta \simeq 90°$–$120°$ above $f_{c_{H+}}$ (Θ is an angle between the directions of the Earth's magnetic field and the wave vector).

4.3 Daytime Conditions

A representative example for daytime conditions is shown in Figure 4.7. The part of the pass between 20:48:33 to 20:50:25 UTC is shown. This time period corresponds to 11:19–11:03 LT and 10.00–10.08 MLT. Daytime satellite passes are southbound while nighttime passes are northbound; however, the direction of the pass has no effect on our experiments overall since natural conditions are assumed to be stationary within any given DEMETER pass. The display in Figure 4.7 is inverted in time to simplify the spatial comparison with nighttime case presented in Figure 4.4.

From Figure 4.7 we can see that the distinctly strong signal now is observed for two pulses. The horizontal distance between two pulses is 31 km and observations of the column as 1 or 2 pulses are typical in cases when the satellite passes close to
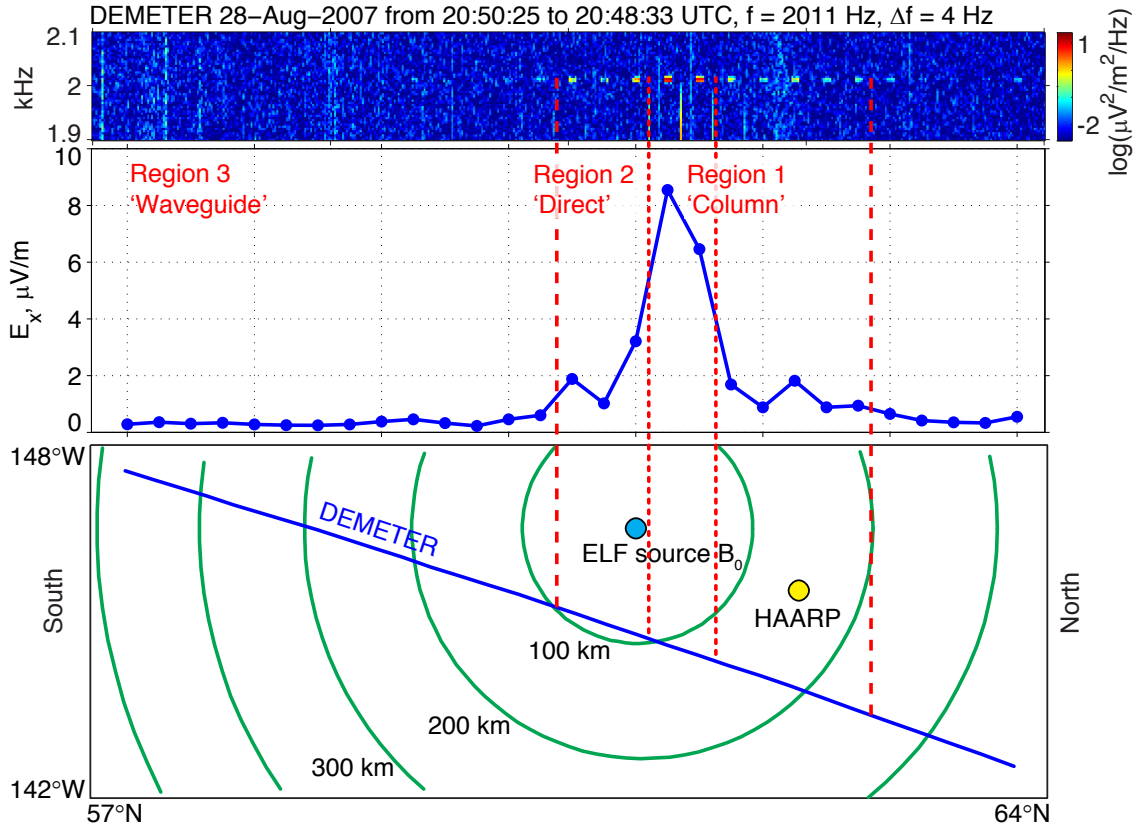
Figure 4.7: Spectrogram and intensity of the electric field on DEMETER for a representative daytime case. The corresponding location of DEMETER with respect to the magnetic field line passing through the ELF source is shown at the bottom. Two regions of ELF field strength can be identified. In the third region the signal is usually below the noise level.

$\mathbf{B}_{0,\text{source}}$. The electric field within the Region 1 Column is 7–9 μV·m^{-1} which is an order of magnitude lower than for nighttime conditions. We also see the signal in the second region within about 250 km. The difficulty in looking at a specific pass is that it is usually not symmetric since it is a very rare situation for the satellite to pass exactly through $\mathbf{B}_{0,\text{source}}$. The strength of the field is on the order of 2 μV·m^{-1} in Region 2, which is again about ten times lower than in nighttime conditions. The signal in the third region is not observed at all as it is below noise level, also a typical feature of daytime observations.

In Figure 4.8 another daytime case is presented. The time of observations shown is 20:46:48–20:47:48 UTC, corresponding to 11:14–11:05 LT and 9.48–9.53 MLT. Even though it is January 19 and the day is short in Alaska, the sunrise was at 09:39 AKST this day. Typically all DEMETER passes around 10:30 LT are daytime passes in the HAARP region throughout the year.

The two top panels of Figure 4.8 show broadband spectrograms of the signal received on the ground and in space. A prominent feature of this example is the presence of the combination of two natural broadband noise phenomena called hiss and chorus emissions [*Golden et al.*, 2009; *Golden*, 2011]. Both hiss and chorus are much more likely to appear around 10 MLT than around 20 MLT [*Meredith et al.*, 2001, 2004]. In this case they are observed with a sharp low cutoff frequency around 400 Hz and variable high cutoff between 1400 and 2000 Hz in space. On the ground the hiss and chorus are barely seen in this example and their intensity is on the order of that of the power line harmonics which are clearly seen above 1.5 kHz. Because the source of the hiss and chorus emissions is in the magnetosphere, it is generally the case that the ratio of hiss and chorus strength to HAARP signal strength is higher on the satellite than on the ground. Hiss and chorus emissions propagate in the same whistler mode as HAARP ELF signal, and in our work hiss and chorus act as a noise, both in electric and magnetic field measurements. Hiss and chorus can preclude the observation of the HAARP signal in space if the transmitted signal falls within the bandwidth of them. In this example they completely mask the 600 Hz signal in space, but in other examples they can mask both the 600 Hz and 2 kHz signals, or just the 2 kHz signal. On the ground, hiss and chorus also mask 600 Hz even though hiss
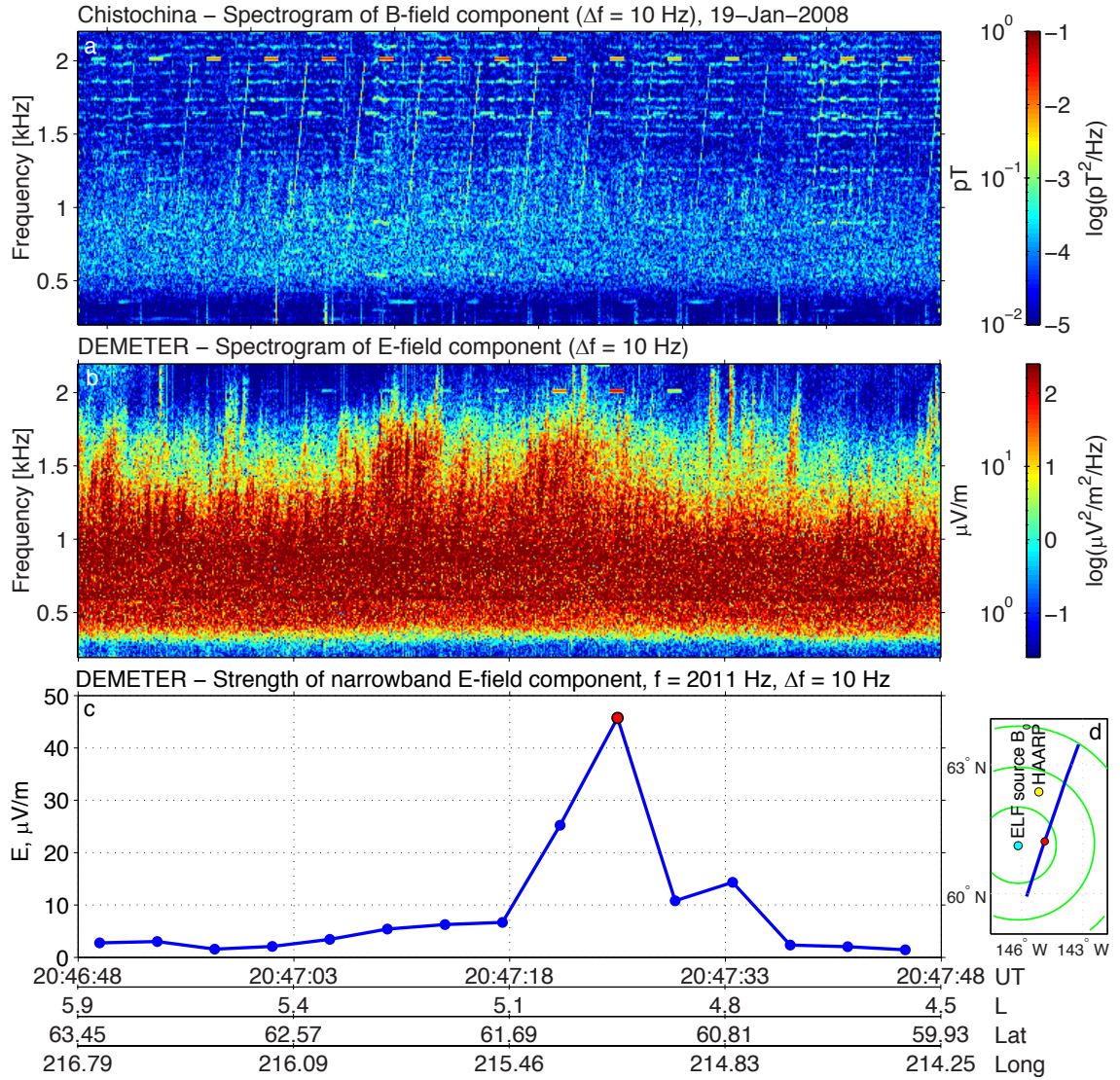
Figure 4.8: Ground and satellite observations of the HAARP signal and hiss/chorus emissions. (a) Ground spectrogram where hiss/chorus to HAARP signal ratio is relatively low. (b) Satellite spectrogram where hiss/chorus to HAARP signal ratio is relatively high and hiss/chorus mask the 600 Hz HAARP signal. (c) Signal intensity of HAARP 2 kHz signal. (d) Map of the pass with the location of the maximum signal marked by a red circle.

and chorus are below the level of 2 kHz signal. The 2 kHz signal on the ground is stronger than the 600 Hz signal as a result of mentioned earlier resonance effect in the Earth-ionosphere waveguide propagation. On the satellite the 600 Hz signal can be even stronger in Figures 4.3 and 4.5 but it is still not enough to overcome hiss and chorus noise.

The satellite signal strength for 2 kHz frequency is shown in panel c of Figure 4.8. The case is typical for daytime observations in terms of the signal profile, but not very typical in terms of absolute signal strength. The signal is one of the highest for daytime observations in space. On the other hand on the ground, the signal strength is relatively average. We see the 2 kHz signal in Regions 1 and 2, and not in Region 3. Two strong pulses can be attributed to the Region 1 Column. The maximum value of $E = 46 \ \mu\text{V}\cdot\text{m}^{-1}$ occurs at the horizontal distance of 80 km from $\mathbf{B}_{0,\text{source}}$. It is also displaced by about 20 km to the north from the closest approach of the satellite to $\mathbf{B}_{0,\text{source}}$, but this displacement can be neglected since the resolution of our observations is 31 km.

Chapter 5

Aggregate Observations over HAARP

Analysis of separate cases in the previous chapter allowed us to learn about several important features of ELF wave propagation from an HF induced source. However, it is crucial to establish the repeatability of those features and determine the kind of wave propagation we can expect on average for day- and night-time conditions. For this purpose, we analyze in this chapter the average field over multiple DEMETER passes. The experiments were conducted for four years in 2007–2010. DEMETER successfully recorded ELF signals in 484 nighttime and 333 daytime passes over HAARP using the Burst mode. However, the actual HAARP transmissions for our experiments occurred in 82 night and 93 day passes. The geometry of all passes is shown in Figure 5.1. The passes for which HAARP transmitted and DEMETER successfully recorded constitute the basis of our analysis in this chapter.

5.1   Automatic Pulse Detection Algorithm

To analyze DEMETER data in a streamlined manner an algorithm was developed. The algorithm can principally be divided into two major parts. In the first part, pulses transmitted by HAARP are automatically detected for every DEMETER pass. As a result, a database of pulses with all characteristics of every pulse is created.
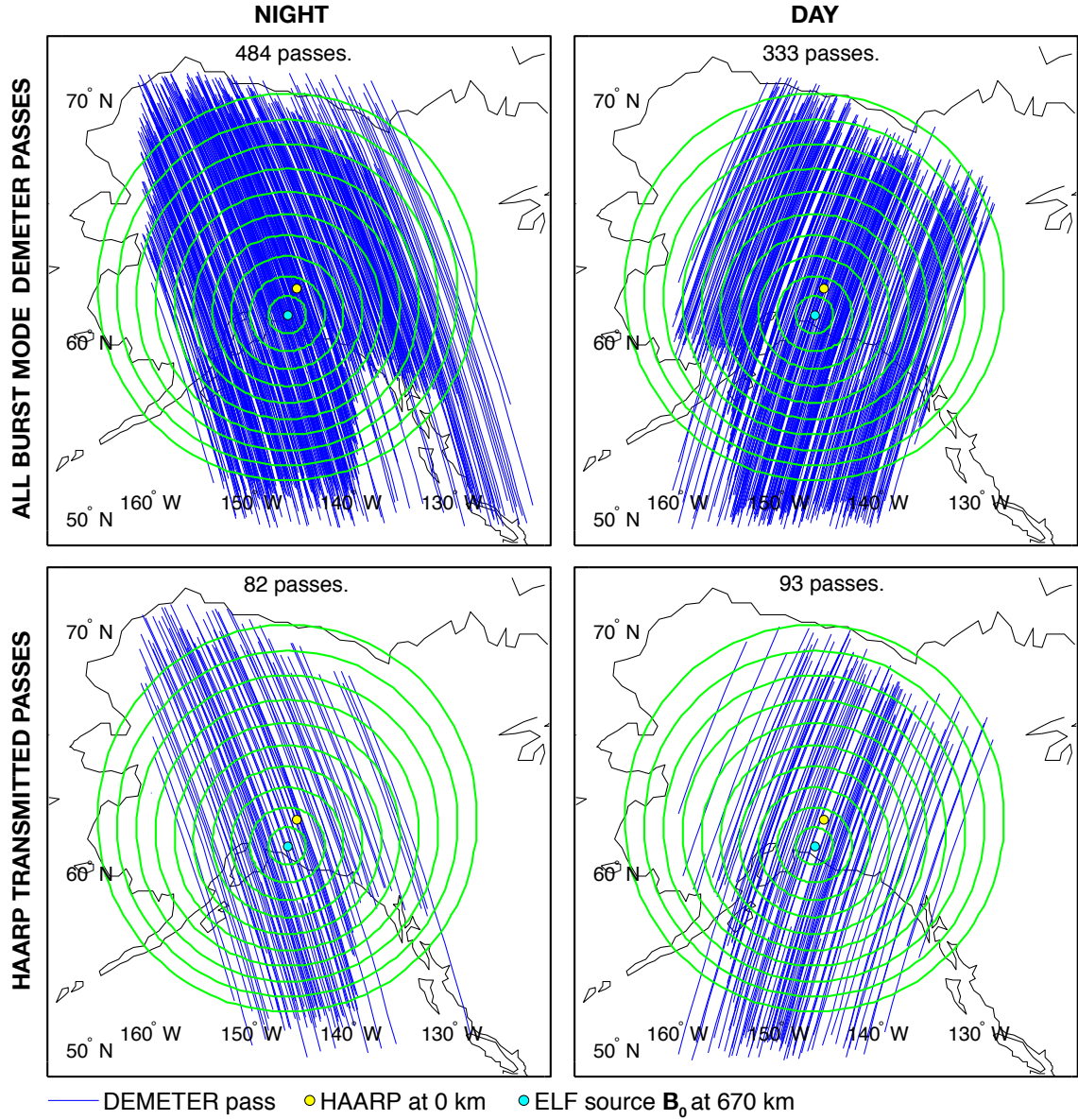
Figure 5.1: Geometry of DEMETER passes over HAARP in which the satellite was recording during the 2007–2010 experimental campaigns. Left side shows nighttime passes around 22:30 LT, while right side shows daytime passes around 10:30 LT. The top maps contain all passes in which DEMETER was recording in the Burst mode. The bottom maps contain the subset of passes for which the satellite was recording and HAARP was transmitting for our DEMETER experiments.

In the second part, the database is analyzed in various manners depending on the application. In other words, the first part is connected with the way experiments were organized, while the second part is connected with the desired applications. The first part is run once on all DEMETER data collected for four years which constitute 260 GB of broadband recordings. All relevant physical features are extracted into a file size of about 20 MB during the first part of the preprocessing. This enables quick analysis in every specific application. In this section we describe the first part: automatic pulse detection, and the second part—analysis of preprocessed data—is shown later in relation to specific applications.

The overview of the automatic pulse detection algorithm is shown in Figure 5.2. The first stage of the algorithm is the creation of a spectrogram over the whole duration of the satellite pass ($\sim$ 3 min) and within the bandwidth of the transmitted signal. Figure 5.2 shows a zoomed part of the real spectrogram for 8 s containing two 614 Hz pulses which are clearly distinguished visually in the presented example. Time resolution of the spectrogram is $\Delta t = 0.25$ s and $\Delta f = 4$ Hz. These parameters enable the concentration of the majority of the pulse power in four bins that occupy 4 Hz and 1 s. The purpose here is not to measure all power related to transmitted signal (in which case frequency side lobes might also be included) but to detect the signal. For this purpose the signal within only the main frequency bin is considered because frequency side lobes contain variable amount of the signal in every specific case. In this connection, we note that the duration of the pulses is 1 s, and therefore the original signal bandwidth is about 1 Hz. However, due to the propagation through the irregular ionospheric plasma, pulses become spread in frequency. The amount of signal leakage into adjacent frequency bins varies. For detection, the maximum power difference between the signal bins and noise bins is desired. It is for this reason that the main frequency bins are used for detection. In time, HAARP always transmitted a signal for 1 s, starting at the beginning of the second. The time delay for the frequencies considered is less than 0.1 s and can be neglected for our purposes. It should also be mentioned that different values of $\Delta f = 1, 2, 8$ Hz, and correspondingly $\Delta t = 1, 0.5, 0.125$ s, were tested, but that $\Delta f = 4$ Hz and $\Delta t = 0.25$ s were found to be the best for detection and signal strength estimation.
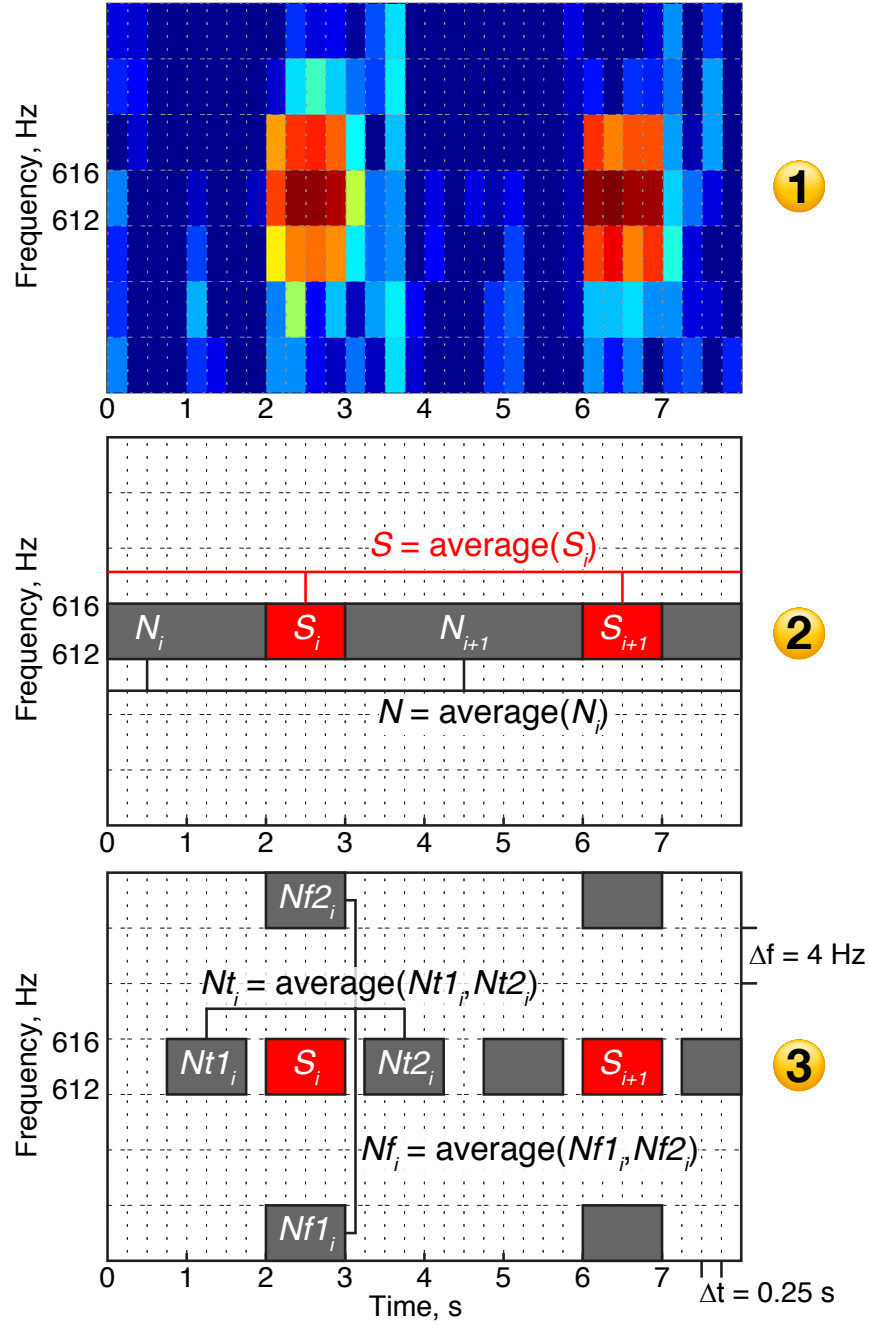
Figure 5.2: Automatic pulse detection algorithm. Stage 1: creation of spectrogram. Stage 2: detection of the whole signal by epoch averaging using the criteria $S > N + 4$ dB. Stage 3: detection of separate pulses using the criteria $S_i > Nt_i + 6$ dB and $S_i > Nf_i + 6$ dB.

At the second stage of the algorithm we detect the overall presence of the signal for a specific DEMETER pass. This detection is done with an epoch averaging technique shown schematically in the middle panel of Figure 5.2. Epoch averaging, rather than single pulse detection, enables the detection of the signal with lower SNR. As shown, the signal is averaged over the time bins when we expect to see the signal, and then compared to adjacent noise. This comparison is done within the DEMETER horizontal distance from $\mathbf{B}_{0,\text{source}}$ of 300 km, where we expect to see the strongest signal from previous case studies. The signal is considered to be detected where S is more than N by some amount of SNR. The epoch averaging technique was trained on about 20 daytime and nighttime cases, and it was found empirically that an SNR of 4 dB allows the detection automatically of the signal which is observed visually at the spectrograms and never to produce false overall detection. As a result, the criteria for a signal to be present during a specific pass is $S > N + 4$ dB.

The ultimate goal of the automatic detection is to register every separate pulse. This is done at the third stage shown in Figure 5.2. At this stage we use DEMETER passes for which epoch averaging produced positive results. We look for the pulses not only within 300 km from $\mathbf{B}_{0,\text{source}}$ but during all DEMETER Burst mode observations which can be at distances up to 2000 km horizontally. Now the signal intensity of the pulse S_i is compared to adjacent average noise in time Nt_i and in frequency Nf_i. It was found empirically that an SNR of 6 dB in time and in frequency allows the detection of at least 95% of visually detected pulses and produces no more than 2% of false detection rate for signals which are not HAARP pulses in reality. It is important to keep the false detection rate low, because false pulses can produce the wrong physical interpretation in the final results. Principally, the epoch averaging stage (Stage 2) could have been omitted since we do SNR filtering in the Stage 3 also, but this omission could create some spurious results when only one or two pulses for a pass are false detected in the random location, because it is easy for random noise to appear within one specific bin where we expect our signal. On the other hand, case studies show that if there is a signal in E-field we can see at least three or more HAARP transmitted pulses.

We should note that the detection is done using the electric field data because the

electric field measurements are more sensitive than the magnetic field measurements on DEMETER. However, after detection in the E-component, parameters of pulses in the B-component can be calculated.

After the pulse is detected at Stage 3, it is stored into a database with all relevant parameters. First, the time, location and frequency of the pulse is stored. Then the strength of the pulse E-field and power spectral density (PSD) of the E-field pulse is calculated with Hamming and rectangular windows of Fourier transform. The same is done for the B-field. Also, frequency and time noise calculated at Stage 3 are saved.

As mentioned above, six pulse frequencies were repeatedly used: 547, 565, 571, 613, 1973, 2011 Hz. After detection the first four (547, 565, 571, 613 Hz) and the last two (1973 and 2011 Hz) are grouped together in this work and referred to as 600 Hz and 2 kHz signals.

5.2   Spatial Distribution of Detected Pulses

A result of the automatic detection algorithm run on DEMETER passes for the years 2007–2010 is shown in Figure 5.3. Here we can see the spatial distribution of detected pulses for nighttime and daytime conditions, and for 600 and 2000 Hz. In every one of the presented passes both the 600 Hz and 2 kHz signals were transmitted with the Default pattern from Table 4.1.

The most general observation is that pulses are centered around $\mathbf{B}_{0,\text{source}}$ as expected. The widest region of received signal occurs during nighttime at 2 kHz (Figure 5.3a). For these conditions pulses are observed in all three regions schematically shown in Figure 1.7. The farthermost pulses are at 1200 km horizontally to the south and at 900 km to the north from $\mathbf{B}_{0,\text{source}}$.

The signal in Figure 5.3b for daytime 2 kHz case is detected within Region 2. It is seen that most of the signal is within 300 km of $\mathbf{B}_{0,\text{source}}$, but it is more concentrated within 200 km. However, there are several pulses beyond the 300 km distance, underscoring the fact that the boundary between Regions 2 and 3 is somewhere between 200 and 300 km, but obviously is not a sharp boundary. For the case of 600 Hz nighttime conditions (Figure 5.3c), the signal is also detected within Region 2. There is just a
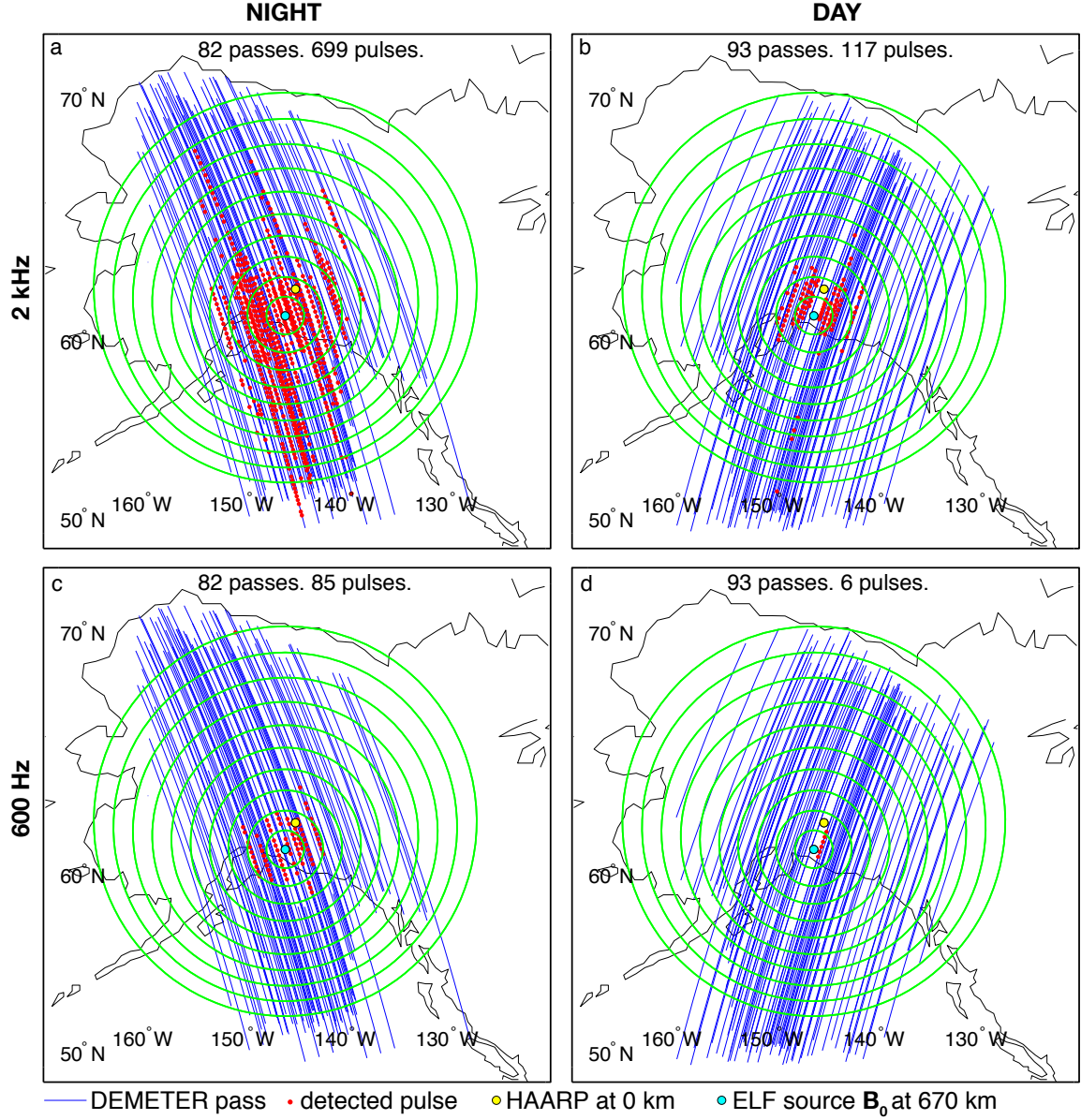
Figure 5.3: Spatial distribution of automatically detected HAARP pulses during 2007–2010 DEMETER passes. Left side shows nighttime passes around 22:30 LT, while right side shows daytime passes around 10:30 LT. The top maps concern 2 kHz pulses. The bottom maps concern 600 Hz pulses.

small amount of pulses in the range of 200 to 300 km. It is interesting that from an observational point of view, detection only within Regions 1 and 2 is clearly similar in 2 kHz daytime and 600 Hz nighttime cases. However, as shown later, the physical interpretation for this fact is quite different. Modeling and physical interpretation is discussed in detail in the next chapter.

For the case of 600 Hz daytime passes, the signal was detected only in one pass and only within Region 1. This rarity of detection unfortunately makes it impossible to do any averaging, but still constitutes a valuable physical result.

5.3 Average Signal Strength

The next step after looking at the location of detected pulses is to estimate the absolute signal strength and its spatial distribution over HAARP. For this purpose the coordinate system introduced in Section 2.1 is used. The DEMETER plane is divided into the orthogonal grid with cell size $\Delta x = \Delta y = 50$ km. The cell size of 50 km is chosen as a compromise between resolution and average amount of pulses falling within a cell. In case of 50 km cell we have up to 10 pulses in the Region 2 for nighttime observations. The white circle is used instead of cyan dot to mark the location of $\mathbf{B}_{0,\text{source}}$ in color plots with signal strength distribution like in Figure 5.4.

5.3.1 2 kHz Nighttime

Figure 5.4 shows the result of averaging for the 2 kHz signal during nighttime passes for years 2007–2010. Electric field is calculated in every cell by averaging electric fields of the pulses that fall within this cell. If no pulse is detected within a cell, then the E-field value is set to zero and is represented as the darkest blue in Figure 5.4.

First and most important result seen in Figure 5.4 is the presence of the Region 1 Column in aggregate observations with signal averaging. It is seen that the column takes 2 cells with average field values of 83 and 106 μV·m^{-1}. To remind the reader, the data used here are the values of one horizontal component of the $\mathbf{E}$-field. Since the column occupies two cells we can conclude the size of the column is $dx_{\text{col}} = 50$ km
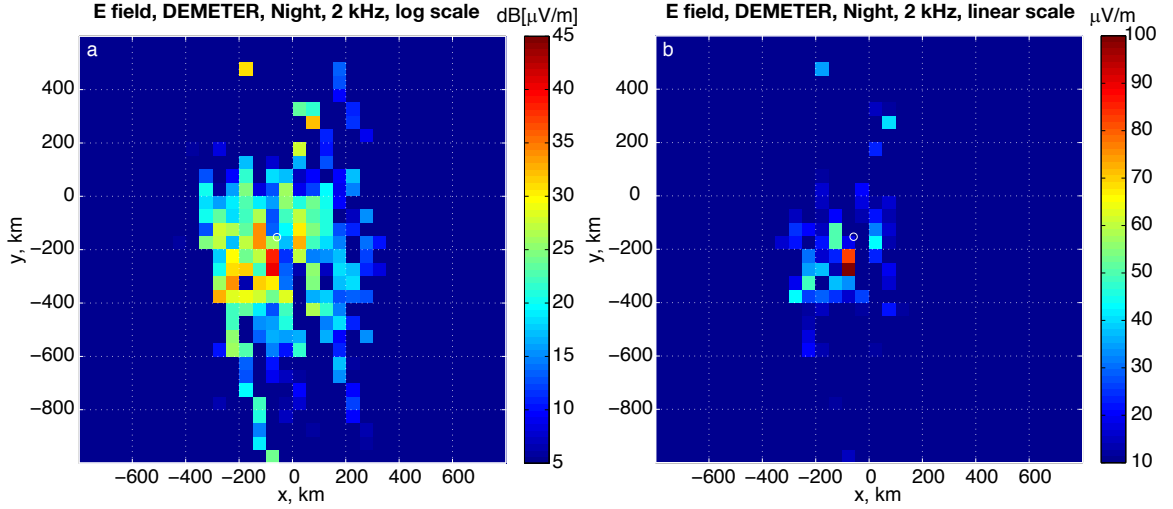
Figure 5.4: Average 2 kHz signal at night at DEMETER altitude for years of 2007–2010. The same results are shown in logarithmic (a) and linear (b) scales. Origin of coordinates corresponds to HAARP vertical projection and white circle shows the location of $\mathbf{B}_{0,\text{source}}$ at DEMETER altitude.

and $dy_{\text{col}} = 100$ km. If we define the location of the column to be on the border between two cells with maximum field then it is at $x_{\text{col}} = -75$ km, $y_{\text{col}} = -250$ km. The column is displaced by $\Delta y_{\text{col}-B_0} \simeq 100$ km south from $\mathbf{B}_{0,\text{source}}$. The displacement in the east-west direction $\Delta x_{\text{col}-B_0} = 17$ km is smaller then the cell size and can be neglected.

Second, it is possible to distinguish the Region 2 in Figure 5.4b. In linear scale with 10–100 μV·m^{-1} range, the signal is observed mostly within 200-300 km range from Region 1 Column. We can notice that the center of Region 2 on average is displaced to the south from $\mathbf{B}_{0,\text{source}}$ by similar amount as the column, but it is slightly more displaced to the west than the column. Logarithmic scale of Figure 5.4a, on the other hand, allows us to see the signal in all regions clearly, including in Region 3. It is seen that the signal level in the Region 3 is quite variable, and that it can, for instance, vary in the range of 1–10 μV·m^{-1} on the edge of Region 3. We should note that this is a real variation since the noise is already filtered by the automatic detection algorithm.

Now we can compare the E-field in different frequencies and local time conditions. For this the logarithmic scale is used since it covers higher dynamic range better. The comparison is presented in Figure 5.5 and a step by step discussion is presented in the following.

5.3.2 Nighttime versus Daytime

We start our discussion of comparison with 2 kHz signal at different local time conditions. Visually the comparison is given in Figures 5.5a and b. First, it should be noted that the scale of daytime plots is 15 dB less than that in nighttime plots. In daytime we also, as in nighttime, can discern Region 1 as the highest signal that occupies 2 cells (marked by white ellipse). In nighttime average values of field are 83 and 106 μV·m^{-1}, while in daytime they are 13 and 14 μV·m^{-1}. This is approximately an order of magnitude less in the field, and two orders of magnitude in power. For daytime we can assume the average location of Region 1 is $x_{\mathrm{col}} = 0$ km, $y_{\mathrm{col}} = -125$ km. Therefore, Region 1 displacement from $\mathbf{B}_{0,\mathrm{source}}$ is $\Delta x_{\mathrm{col-B_0}} = 58$ km east and $\Delta y_{\mathrm{col-B_0}} = 28$ km north. The second value is lower than the resolution of the observations, but the first value is most probably a real physical result. It is interesting that in general the column in this case is displaced towards the vertical from the source ($x = 0$, $y = 0$). As it is discussed in the Chapter 6, such a result is expected for ELF wave propagation in the ionosphere without local horizontal density gradients.

The second important result of day/night comparison is that during the day the signal is mostly observed within Region 2. The size of the Region 2 is up to 300 km in radius and is slightly displaced as a whole from $\mathbf{B}_{0,\mathrm{source}}$ towards the vertical similarly to Region 1. The E-field in Region 2 is attenuated during daytime by about 5 dB more than it is attenuated in Region 1. On the other hand, attenuation in Region 3 is dramatically higher, by at least another 15 dB in comparison with Region 1. The sensitivity of our observations (taking into account receiver sensitivity, averaging, noise, and detection limit) is $\simeq -10$ dB[μV·m^{-1}], because no pulse was detected automatically below this level. This value corresponds to the lower limit of the scale in Figure 5.5b and all detected signals should be visible in this plot. Higher
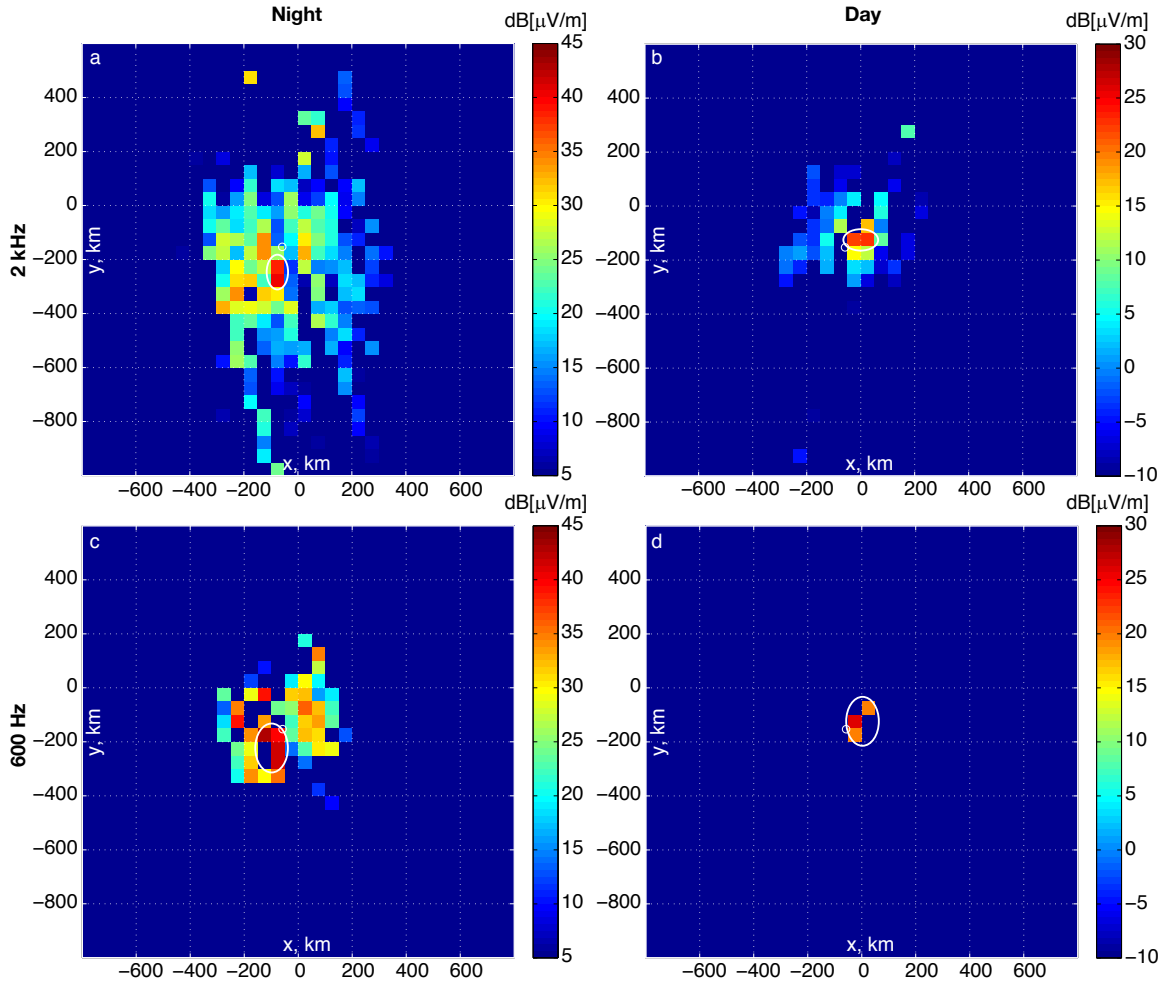
Figure 5.5: Comparison of average electric field on DEMETER for years 2007–2010. Top plots (a,b) are for 2 kHz pulses and bottom plots (c,d) are for 600 Hz pulses. Left plots (a,c) represent nighttime conditions, while right plots (b,d) show daytime conditions. Note that the scale in the right plots is 15 dB less than in the left plots. Region 1 is approximately marked by white ellipses.

attenuation and almost no detected signal in Region 3 suggests that the propagation to the space in Region 3 is qualitatively different than in Regions 1 and 2.

The comparison of nighttime versus daytime for the 600 Hz signal (Figures 5.5c and d) is rather limited by the number of detected pulses in daytime conditions. Even though the number of analyzed satellite passes is even higher during daytime (93 versus 82), just 6 pulses, all of them in single DEMETER pass, were detected on daytime. From this observations, we can only conclude that 600 Hz daytime detection in space can only be obtained under very limited conditions, rather than on a regular basis. The signal is detected only in Region 1 and for this case is detected at about 15 dB lower than for the highest nighttime fields. This result is similar to results for the 2 kHz signal. One reason for the low detection rate of 600 Hz daytime signal is probably the higher occurrence rate of hiss and chorus noise in this frequency band as shown in Figure 4.8b.

5.3.3 2 kHz versus 600 Hz

Figure 5.5c presents the results of nighttime 600 Hz signal observations. Region 1 here is not so obvious as in previous situations, but it is still possible to identify it as an inverted L-shaped region that occupies four cells. It is displaced to the south, but the precise quantification of the displacement is restricted by the resolution of the measurements. It can be qualitatively assessed as partially similar to the 2 kHz nighttime displacement to the south and additionally be partially displaced to the west. The signal strength in the column is about 3–5 dB higher for 600 Hz then for 2 kHz.

The whole space of observed signal is similar to the 2 kHz daytime case in the sense that the signal is detected only within Region 2. However, in the 600 Hz case, Region 2 is well centered around $\mathbf{B}_{0,\text{source}}$. The signal strength in Region 2 is similar to Region 1 being higher by 3–5 dB for 600 Hz then for 2 kHz. Despite the similarity of the entire observed region in Figures 5.5b and c, the signal strengths are substantially different in the 2 kHz daytime and 600 Hz nighttime cases. It is seen in Figure 5.5b that the signal level smoothly decreases to the sensitivity level of -10 dB$[\mu\text{V·m}^{-1}]$.

On the other hand, in Figure 5.5c the signal abruptly disappears in Region 3. The lowest detected signal is $\sim$ 10 dB[μV·m^{-1}] and there is still 20 dB room above our sensitivity level. However, no signal in the -10 to 10 dB[μV·m^{-1}] range is detected in Region 3. This lack of detection suggests different propagation mechanisms in those two situations as discussed later in the theoretical part of this work (Chapter 6).

5.4   Summary of ELF Observations over HAARP

The case studies and aggregated calculations show three typical regions where the ELF signal can be observed. The regions are distinguished on the basis of the E-field strength, the E-field fall-off from the center, and the presence of the signal in the regions for various conditions. The size of Region 1 with the strongest signal varies from about 28 km in case studies when it is seen only for one pulse to up to 150 km in aggregate studies when it takes three 50 km cells. However, those are rather extreme values and more typical range of sizes for Region 1 is 50–100 km (50 km for two pulses in case studies and 100 km for two cells in aggregate study). It is seen that in specific cases the Region 1 Column is recorded as a narrower feature than in aggregate calculations. This result most probably can be explained by the fact that the Region 1 on its own is about 30–50 km in size but that the location of this region can change by up to 100 km from day to day so that in averaged observations its size is 100–150 km. Aggregate studies also show that on average the location of Region 1 is displaced about 100 km to the south from $\mathbf{B}_{0,\text{source}}$ at DEMETER altitude during nighttime. On the other hand, during daytime there is no north-south displacement from $\mathbf{B}_{0,\text{source}}$.

Region 2 is distinguished from Region 3 in case studies by higher signal and by a faster fall-off of the signal. Both in case studies and in aggregate observations, Region 3 appears only for 2 kHz nighttime observations. Region 2 is seen in all considered cases in Figure 5.5 except 600 Hz daytime observations. This result makes Region 2 different from Region 3 not only in terms of quantitative parameters but also in in terms of qualitative characteristics. Figure 5.5 confirms the values for the sizes of the Regions 2 and 3 shown approximately in Figure 1.7. Again, due to day-to-day

variations, the average location of the Region 2 is within 300 km from the maximum signal, but on a specific day the radius can go down to 200 km.

Chapter 6

Modeling and Interpretation

Modeling of ELF wave propagation is an important tool for the future utilization of these waves for both remote sensing and other applications. Modeling can predict those parameters for the future experiments and applications that cannot be obtained directly from experimental techniques. As in any physical science, the experiment serves as the verification of modeling and as the check of the applicability of a model in specific conditions. Also, an experiment can guide us in the selection of the appropriate model. In our work we apply these concepts to full-wave and geometrical optics (ray tracing) models of ELF wave propagation described in Section 2.4.

Additionally, modeling in our work can help in the interpretation of observations. Such model-based interpretation is one of the emphases of the current chapter. The experiments discussed in previous chapters are limited, for instance, by the total number of cases, the altitude and local time of observations, and number of frequencies used. Since it is not possible to capture the whole 3D distribution of electromagnetic fields for every parameter, modeling consistent with experiments can fill the missing gaps in physical understanding. We thus use modeling to interpret the presence of various regions of radiation, and the size and location of each region. We also use modeling in understanding of local time and frequency dependences.

6.1 Full-Wave Modeling

6.1.1 2 kHz Waves

We start with the presentation of results for the strength of the electric field component E_x in the horizontal DEMETER plane (Figure 6.1). The results of the full wave model for 2 kHz signal are presented in Figures 6.1(b,d). The model is compared with corresponding DEMETER observations for the 2 kHz signal in Figures 6.1(a,c). The space is limited from -800 km to 800 km in the x-coordinate from HAARP vertical projection, and from -1000 km to 600 km in the y-coordinate. The white circle in Figure 6.1 represents the location of $\mathbf{B}_{0,\text{source}}$.

The model is run one time for a typical nighttime and daytime ionospheric plasma density profiles over HAARP. On the other hand, the observations shown are the result of DEMETER measurements in different days with varying ionospheric conditions. The best comparison would be done if the model is applied for every pass with specific ionospheric conditions. However, such a case-by-case comparison is not attempted for several reasons. First, the ionospheric profile is usually not known precisely from observations for every day. Second, application of the model for every case would be prohibitive from the point of view of computational resources. One model run takes about an hour for one frequency on a desktop computer. Third and most important, we note that the precise correspondence of the model results and observations is not the main objective of this study. As mentioned before, the purpose is to understand the physics of wave propagation, as well as determine the restrictions of the model so that we can improve it, if possible. Multiple runs, on the other hand, would not change the major features we would like to compare. Most likely, the only noticeable feature that is not seen in observations but is obvious in the model results is a pattern of nulls and peaks resulting from waveguide mode distribution in the Earth-ionosphere waveguide and projected to the DEMETER plane. This pattern is pronounced in Figure 6.1b with spiral maxima and minima in the electric field distribution. It is not symmetrical with respect to the azimuthal coordinate because the ionosphere is an anisotropic medium and there is always a dominant direction of the auroral electrojet current. Most probably, this pattern is not seen in observations because it

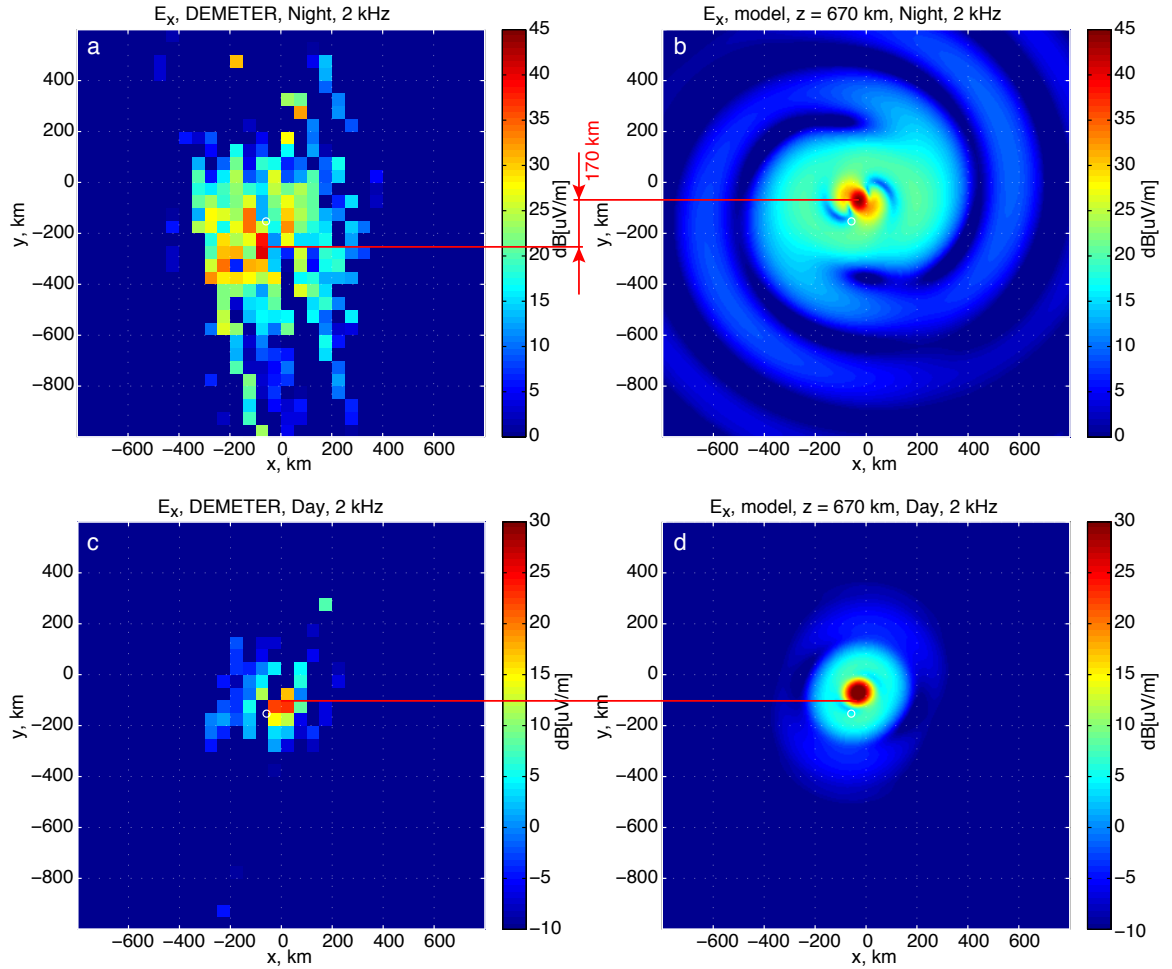Figure 6.1: Comparison of SFWM model and observations for 2 kHz. Absolute value of E_x component is presented. Left side plots: aggregate DEMETER observations discussed in Chapter 5. Right side plots: results of SFWM model for similar conditions. The maxima during nighttime are shifted by 170 km in observations and model. During the daytime the shift is less then the 50-km resolution of observations.

is averaged out by the day-to-day variations of the electrojet current and ionospheric plasma density.

It should be noted that the electrojet current in modeling should sometimes be scaled linearly by some value in order for fields to have similar absolute magnitudes in modeling and observations. This adjustment needs to be done because the electrojet current is not known for every observation. Since we compare modeling with aggregate observations, the scaling of the electrojet current is equivalent to using the average electojet current in modeling. For modeling this procedure leads to the selection of the maximum of the average HF-generated input current density $\mathbf{J}_\perp(\mathbf{r}_\perp, z)$ from equation (2.4). Here, we use $\max|\mathbf{J}_\perp(\mathbf{r}_\perp, z)| = 2.5$ nA·m^{-2} as is consistent with current observations and previous measurements [*Payne et al.*, 2007].

Generally, it is seen that the field distributions in the model and observations have many similar features. The size of Region 1 with the strongest signal is comparable in both observations and model for day and night. For night, it is established in Chapter 5 that the size of Region 2 is 200–300 km in radius. The model shows the comparable sizes of 300 km in the east-west direction and 200 km in the north-south direction (Figure 6.1b). The signal strength is more variable in observations in Region 2 both during night and day, but the average values are close in magnitude to the model. The high variability in observations can be attributed to varying day-to-day ionospheric conditions and not enough data points for those effects to be averaged out. The field in Region 3 for nighttime is close in magnitude for instance at ($x = 0$, $y = -800$ km). However, the fields are not the same at every point of Region 3 for two reasons. First, as is discussed above, there is a spiral pattern in the model which is not expected to be observed in aggregate measurements. Second, the coverage by DEMETER beyond 300 km from HAARP is not symmetrical in north-south and east-west directions. The experiments with close satellite passes were usually given priority. Since the satellite mostly travels in a north-south direction, a close pass covers all distances in the north-south direction, but there are less data points beyond 300 km in the east-west direction. This orbital selection is most probably the reason why Region 3 is not circular in observations for nighttime. On the other hand, the coverage within 300 km is even, which is why Region 2 during the day and night

is measured evenly. The similarity between region sizes and shapes is pronounced strongly in the daytime when there is a clear boundary between Region 2 and Region 3 in which the signal is almost absent.

The important advantage of the full-wave model is that it is easy to calculate the distribution of any field or related values in any plane. Figure 6.2 shows the distribution of the absolute value of the Poynting vector in a vertical plane passing through the center of the source in the north-south direction ($x = 0$). We chose to present the Poynting vector here rather then the electric field as before, because it makes sense for the comparison of values in the ionospheric plasma and the Earth-ionosphere waveguide. Electric field values would include not only the wave propagation effects but also the change of refractive index with altitude as the medium changes, and would not be as appropriate for such a comparison.

Figures 6.1 and 6.2 show that in modeling, Regions 1 and 2 have their own specific structures which are not periodic as in Region 3. This result supports the hypothesis that the field in these regions is not affected strongly by waveguide modes but rather represents the near-field of the radiating source. It is possible to try to make a qualitative analogy with antenna radiation in free space. The classical conditions for the far-field of an antenna [*Stutzman and Thiele*, 1998, Ch. 1] are the following:

$$r > \frac{2D^2}{\lambda}, \tag{6.1a}$$

$$r \gg D, \tag{6.1b}$$

$$r \gg \lambda, \tag{6.1c}$$

where r is the distance from an antenna, D is the linear size of an antenna, and λ is the wavelength in the medium. The wavelength in our case is generally variable in the plasma and the antenna is located close to the interface between the plasma and free space. We can consider $D = 40$ km (see Figure 2.8) and two extreme cases of λ equal to 170 km in free space and roughly 15 km in plasma for 2kHz waves. We then
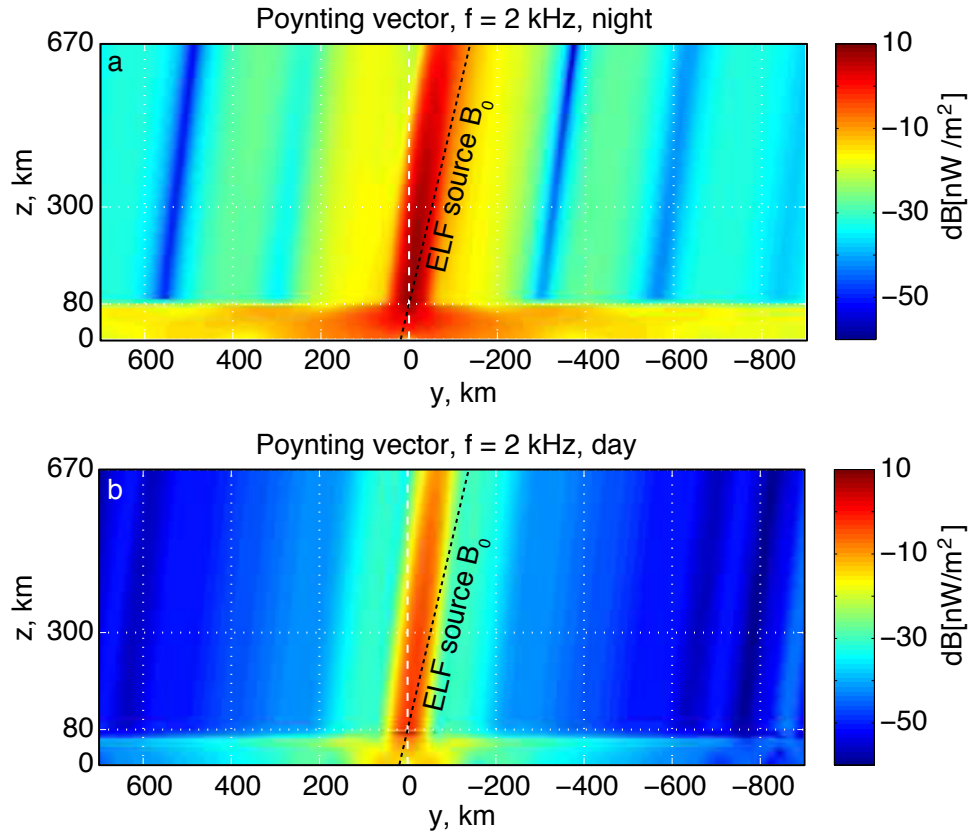
Figure 6.2: Absolute value of the Poynting vector as calculated by the full-wave model for 2 kHz modulation for (a) nighttime and (b) daytime conditions. The ELF waves in the Region 1 Column propagate between the vertical and the Earth's magnetic field $\mathbf{B}_0$ direction.

have respectively for free space and for the plasma:

$$r > 21 \text{ km and } 213 \text{ km}, \tag{6.2a}$$

$$r \gg 40 \text{ km}, \tag{6.2b}$$

$$r \gg 150 \text{ km and } 15 \text{ km}. \tag{6.2c}$$

In other words, it appears that the space within about 200 km is indeed in the near-field of the ionospheric ELF antenna. It should be noted that the full-wave model includes the correct calculations of both near and far-fields, since it solves Maxwell's equations without any assumptions on the distance from the source. In other words, there is in fact no need to differentiate between near and far-fields for the correct usage of the SFWM model, and we do so here only for intuitive understanding of the physics of wave propagation. Also, it is seen from Figure 6.2 that the field structure is mostly formed at the bottom of the ionosphere. In the approximation of the SFWM model, this structure is then projected along the Earth's magnetic field lines to the DEMETER altitude. In other words, Region 2 can be considered qualitatively to fall into the near-field and Region 3 into the the far-field. Obviously, the boundaries between near and far-fields are not abrupt in reality. This intuition is also helpful in order to realize that the fields measured by DEMETER should be mostly comprised by the radiated far fields since the distance from the source to DEMETER is much bigger than any value in (6.2).

The most remarkable and important feature of both measurements and observations is Region 1. This region was named the "Column" since in 3D it represents a columnar structure extending from the source to DEMETER altitude (Figure 6.2). The structure similar to the column was first seen in FDTD modeling by [*Payne et al.*, 2007, Fig. 2]. However, the FDTD model was only run for the small region around the source ($x = -50$ to 50 km, $y = -50$ to 50 km, $z = 0$ to 130 km) which did not allow the full characterization of the structure as the column extending to the top of the ionosphere. The full-wave modeling by *Lehtinen and Inan* [2008] and DEMETER

observations by *Piddyachiy et al.* [2008] found that this structure extends to the top of the ionosphere and plays an important role in the injection of ELF waves up into space.

Figure 6.3 shows the streamlines of the Poynting vector calculated by the SFWM model. It is seen that upward energy propagation is essentially along the straight line direction between the vertical and the Earth's magnetic field. This feature is seen not only in Region 1, but everywhere above the Earth-ionosphere waveguide. For the waves coming directly from the source with k-vectors close to vertical, this result has an important implication that these waves are not spread substantially while propagating upward and that the ELF wave energy generated and launched up is kept within the Region 1 Column. In other words, the group velocities of the waves propagating upward are almost parallel and most of the upward power flux from the source travels inside the column. Also, it is interesting to note from Figure 6.3 that the streamlines of Region 2 in the ionosphere are not passing deep through the Earth-ionosphere waveguide but rather close to the lower boundary of the ionosphere. This result additionally supports the hypothesis discussed above that the field in this region is not influenced substantially by the presence of the waveguide or more precisely by its lower boundary (i.e., not reflected from the ground).

One of the most important discrepancies between the SFWM model and observations is the difference between the location of Region 1 in nighttime. It is seen from Figures 6.1(a,b) that this difference is about 170 km in north-south direction. For daytime (Figures 6.1(c,d)) the difference between model and observations can be neglected as it is within the resolution of observations. In the SFWM model, the location of the maximum signal at DEMETER lies between the vertical from the source and $\mathbf{B}_{0,\text{source}}$. The wave vectors of the ELF waves launched into space are almost vertical because the source has a relatively large horizontal extent [*Lehtinen and Inan*, 2008]. The structure of the refractive index surface of whistler waves dictates the group velocity for vertical wavevectors to be directed between the vertical and the Earth's magnetic field [*Stix*, 1992; *Lehtinen and Inan*, 2008]. This intuitive explanation verifies that SFWM produces correct results with the approximations used herein. As a consequence, it is supposed that the discrepancy arises because

Poynting vector streamlines, f = 2 kHz, night
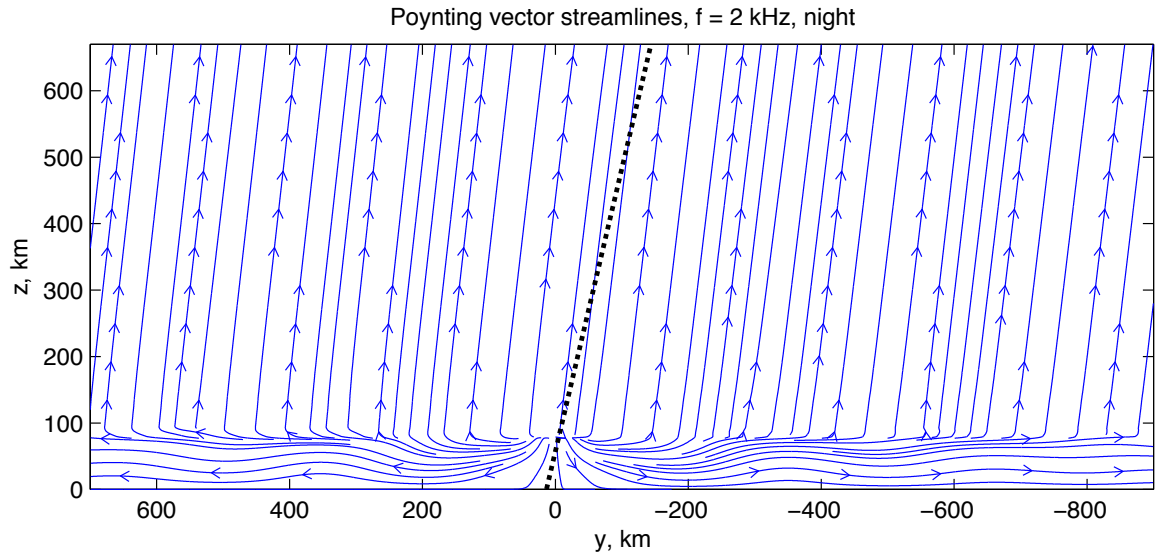
Figure 6.3: Streamlines of the Poynting vector as calculated by the full-wave model for 2 kHz nighttime modulation. Black dashed line shows $\mathbf{B}_{0,\text{source}}$. It is seen that the energy propagates upward in the direction between the vertical and Earth's magnetic field. Also, upward propagation in Regions 1 and 2 is directly from the source without traveling in the Earth-ionosphere waveguide. The waveguide energy propagation is clearly seen too.

SFWM does not take into account the horizontal density gradients that exist in the ionosphere during the night. This result is discussed in detail below, and ray tracing is used for the verification of this hypothesis.

6.1.2   600 Hz Waves

Figure 6.4 shows the results of the full-wave model in comparison with observations for 600 Hz waves. Similarly to 2 kHz analysis, the results of the model for 600 Hz are also presented in a vertical plane passing through the source as seen in Figure 6.5. The most important difference from the 2 kHz case is that waves do not propagate into the Region 3 for 600 Hz. For the frequency of 600 Hz, the half-wavelength in free space is 250 km. Only a TEM mode can propagate in an ideal parallel plate waveguide if the height of the waveguide is less then a half-wavelength [*Inan and Inan*, 2000, Chapt. 4]. The other modes are evanescent. The field in the Earth-ionosphere waveguide consists mostly of evanescent waves that decay with distance and do not propagate upward. In other words, it can be interpreted as the absence of the power that reaches the ground and is reflected afterwards. It is seen from Figure 6.5 that the strong field (> -20 dB[nW$\cdot$m^{-2}]) does not occur near the ground as it does for the 2 kHz case (Figure 6.2).

The absence of the ELF signal in Region 3 for 600 Hz is also clearly visible in observations at both day and night (Figure 6.4). All the signal at night in Figure 6.4a is in Regions 1 and 2. As discussed above, the signal in those two regions reaches the satellite directly or without waveguide propagation. This hypothesis is additionally supported by 600 Hz observations of the signal only in Regions 1 and 2. Since waves are not propagating in the waveguide at 600 Hz, they are also not seen in Region 3 in space.

There are some difference between observations and modeling at nighttime. Region 2 is not symmetrical in the model, but this can be attributed to the fact that the model is run just once for a specific electrojet current direction. The signal in Region 2 is more intensive in observations than in the model, as is also true for the maximum field in Region 1. The strength of the electrojet current model used here
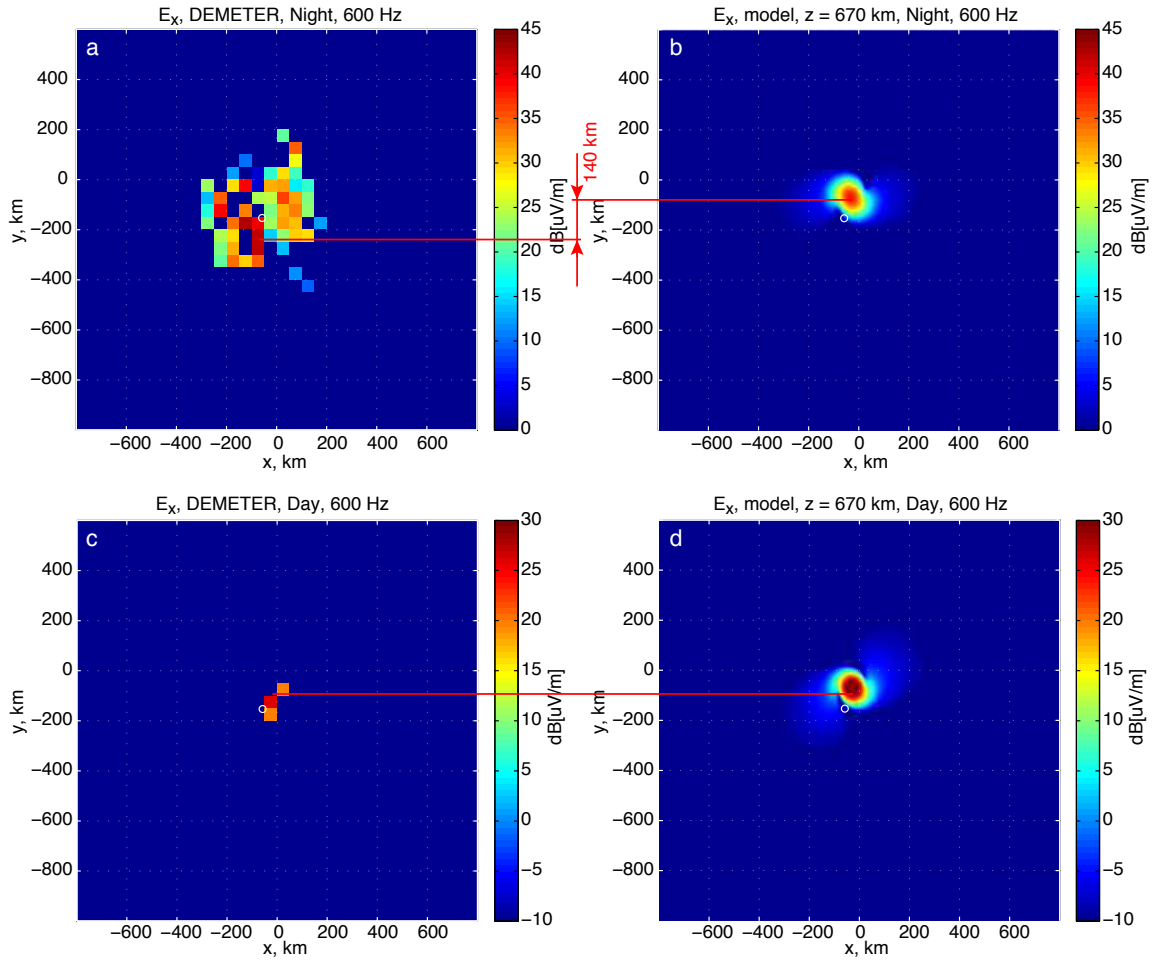
Figure 6.4: Comparison of SFWM model and observations for 600 Hz. The absolute value of E_x component is presented. Left side plots: aggregate DEMETER observations discussed in Chapter 5. Right side plots: results of SFWM model for similar conditions. The maxima during nighttime are shifted by 140 km in observations and model. During the daytime the shift is less than 50-km resolution of observations.
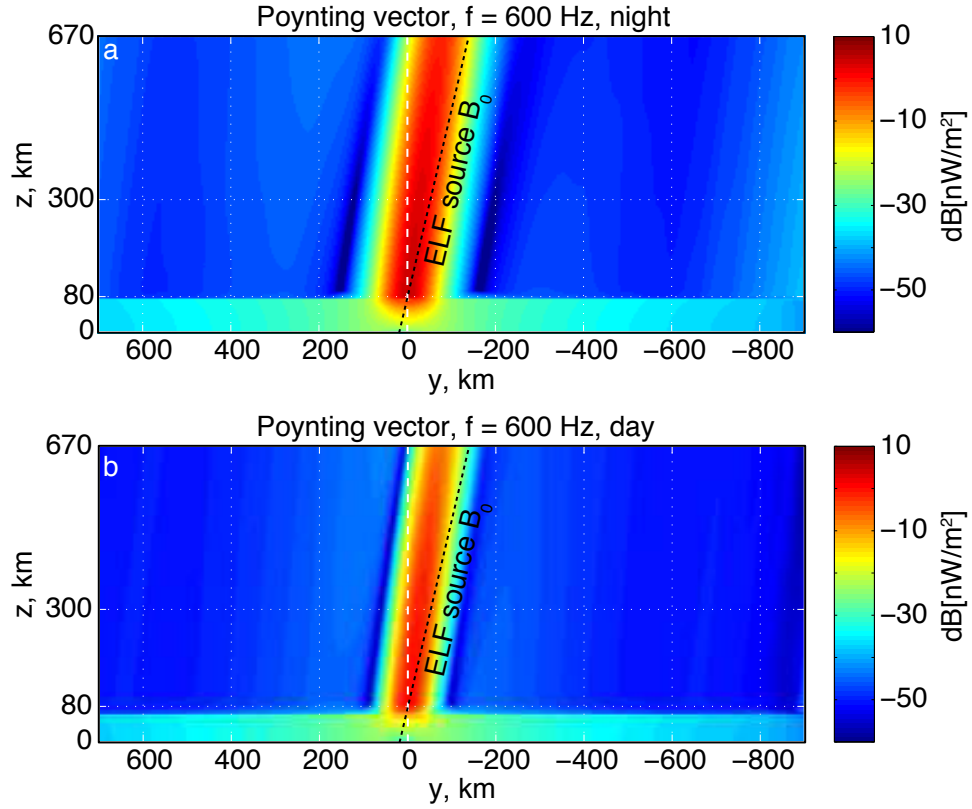
Figure 6.5: The absolute value of the Poynting vector as calculated by the full-wave model for 600 Hz modulation for (a) nighttime and (b) daytime conditions. The ELF waves in Region 1 Column propagate between vertical and Earth's magnetic field $\mathbf{B}_0$ direction. In contrast to 2 kHz waves in Figure 6.2, 600 Hz waves are mostly not propagating in the Earth-ionosphere waveguide because of their long wavelength. As a result, the ELF field is almost absent in the Region 3.

is the same as that for 2 kHz. This model was originally derived for 2 kHz modulation [*Payne et al.*, 2007], and may need to be scaled for 600 Hz. Another possible explanation of the difference is that the model of the ionospheric plasma density from which absorption is calculated might need to be revised.

It is harder to compare reliably observations and model in daytime since the results of observations are derived from only one successful signal reception. However, the fact that the field is well concentrated in the center in modeling may explain the low rate of success for experiments. For the signal to reach the threshold of observations, the satellite needs to pass close to the maximum signal. It is also interesting to note that in the model the difference in signal level between night and day is no longer 15 dB as it is for 2 kHz. For maximum signal of 600 Hz it is 4 dB (38.4 versus 34.4 dB[μV·m^{-1}]). The experimental difference, on the other hand, is closer to the same 15 dB.

The difference in the location of the Region 1 Column during the night for observations and model is also seen for 600 Hz. It is about 140 km, as it is seen in Figures 6.4(a,b). For the daytime, the difference is also below the resolution of observations as in 2 kHz case.

6.2 Ray Tracing

It is shown in the previous section that the major discrepancy between the model and observations is the location of the Region 1 Column. During the nighttime observations, the column is displaced by 170 km to the south for 2 kHz and by 140 km for the 600 Hz waves. The displacement is negligible in the daytime observations. If we recall the results of the ionospheric density observations over HAARP (Chapter 3), it becomes obvious that the density can be very irregular, with variations of various scales. Especially important is a large-scale horizontal gradient in density that occurs within the main ionospheric trough. From Table 3.2 it is seen that the main trough is observed over HAARP in at least 50% of cases during nighttime, and is not seen during daytime. Typical nighttime and daytime measurements of the density on DEMETER are shown in Figure 6.6. The horizontal density gradient is marked in

the figure, and can be as high as an order of magnitude change of the density in several degrees of latitude. However, this number is variable as seen in the data presented in Chapter 3.
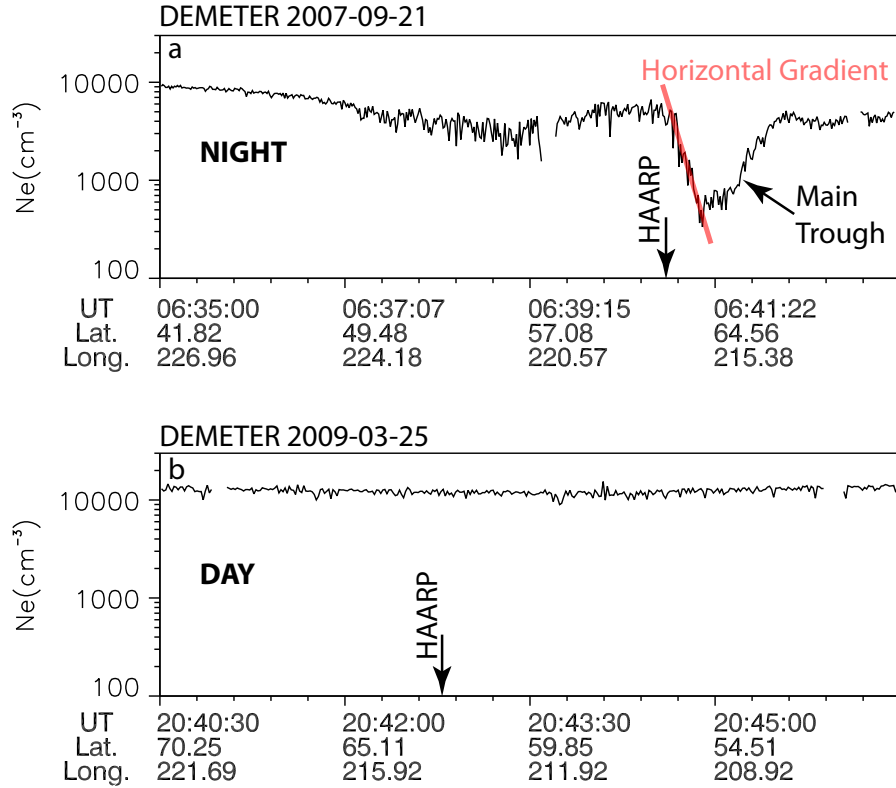
Figure 6.6: A typical electron density at night (a) and day (b) as measured by DEME-TER. The main ionospheric trough is a nighttime only phenomenon. The horizontal gradient within the trough is marked on the plot. The gradient can be as high as an order of magnitude change in density over several degrees in latitude. The location of HAARP is shown by arrows in each plot.

It is hypothesized that the horizontal density gradient is the cause of the discrepancy in the full-wave model and observations. Currently, it is not possible to introduce the horizontal variations in the full-wave model, because it inherently relies on the layered model of the refractive index. The FDTD technique is prohibitive in terms of computer resources for the considered size of the space. Because of these

restrictions, it was decided to use ray tracing to check the hypothesis that the wave energy can be deflected by the horizontal density gradient. Ray tracing is sufficient to verify this hypothesis, because we already know that the large portion of ELF wave energy propagates within the column. As was discussed in Section 2.4.2, the rays in ray tracing represent the path of the wave energy, so they should follow the same path as the column. The purpose here is not to make precise numerical calculations of the column deflection, but rather to show that the displacement values seen in the observations can be reproduced with realistic density gradients.

It is useful to begin the discussion of the ray tracing results with the same stratified medium as was used in the full-wave modeling. Since ray tracing is a simplified method of solving the same Maxwell's equations, it should produce the same results as the full-wave model. The result of ray tracing for 2 kHz waves in the stratified medium without horizontal gradients is shown in Figure 6.7. The figure shows a two-dimensional slice of the region around HAARP. Concentric red lines are located along the Earth's surface, at 210 km where ray tracing starts, and at the DEMETER altitude. The red line perpendicular to the concentric red lines is a vertical passing trough the starting point of the ray tracing. As discussed in Section 2.4.2, the ray tracing can only be started from 210 km altitude since density variations with altitude below this height are too rapid. The Earth's magnetic field line passing through the starting point is plotted in bold black, and the other magnetic field lines are plotted in normal black. Here, it is supposed that the waves do not undergo a substantial change of direction in wave-normals as they propagate from the source to the altitude of 210 km. In other words, the starting wave-normal is perpendicular to the ground as it is predominantly perpendicular to the ground at the source. This assumption can be justified by the small distance between the source and 210 km, and by the fact that strong density gradients occur at higher altitudes. In the following discussion we neglect the fact that ray tracing is not started from the source, because the purpose is to get the proof of the concept with approximate calculations. The color background of Figure 6.7 shows the plasma density distribution in the considered plane. The density is interpolated using the same IRI model as in the full-wave modeling. The most substantial influence of the plasma density on the wave direction is expected

to be in the F-region, where the density is highest and the main trough with density gradients occurs.

Figure 6.7 demonstrates that ray tracing produces the same path of the main energy as it is seen in the full-wave modeling (Figures 6.2–6.3). The ray (blue line) passes the DEMETER altitude between the vertical and the magnetic field line. This verifies that the main assumptions in both models correctly describe the presented case.
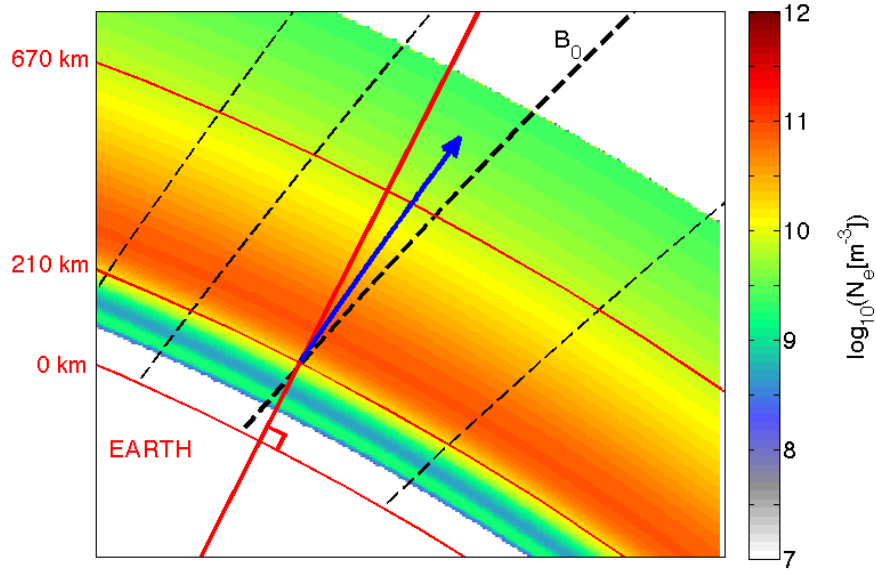
Figure 6.7: Ray tracing with no horizontal gradient in density for 2 kHz waves. A ray starting at 210 km with vertical wave normal angle is shown by blue. The color background describes the electron density distribution in the shown plane. Similar to the wave energy propagation in the full-wave modeling, the ray in the horizontally stratified medium goes between the vertical and the Earth's magnetic field line.

To describe the density gradient at the low-latitude boundary of the trough, a simple empirical model is used:

$$N_e(r, \theta) = N_{e,\mathrm{IRI}}(r) \cdot 10^{(\theta_{\mathrm{HAARP}} - \theta)/\Delta\theta}, \tag{6.3}$$

where r, θ is the radius and latitude, $N_{e,\mathrm{IRI}}(r)$ is the radial density profile over HAARP

from IRI model, θ_{HAARP} is the HAARP latitude, $\Delta\theta$ is the latitude range over which electron density changes by a factor of ten at the fixed altitude. Essentially, the model introduces one parameter $\Delta\theta$ that describes the variation of the density with latitude as a factor in addition to the standard radial IRI profile. This parameter can be deduced empirically from DEMETER observations. Such a model correctly describes the density only at the altitude of satellite measurements and within the latitude range where the density gradient is linear in logarithmic scale. As we can see from Figure 6.6, this can be the case for the low-latitude boundary of the ionospheric trough. For other altitudes such modification of IRI is only approximate and constitutes simply a qualitative model of the density variation. Usually, it is very difficult to model the precise 2D distribution of the plasma density at these altitudes. For instance, IRI model produces the horizontal gradients that are very different from DEMETER observations. Only direct measurements by incoherent scatter radar at the time of HAARP experiments could produce a reliable density distribution. Unfortunately, such measurements were not available. The observations of the trough by EISCAT incoherent scatter radar presented in *Rodger et al.* [1992] demonstrate that the trough can extend from 200 to 600 km altitude within several degrees in latitude. This situation is qualitatively reproduced by our empirical model. The electron density distribution produced by our model is presented by the color background in Figure 6.8. It should be noted that the density is realistic only in the region around the latitude of HAARP (θ_{HAARP}) which is the region of interest for us.

Figure 6.8 shows the variations of ray trajectories under the modification of electron density. Three modifications of IRI were modeled with $\Delta\theta$ equal to $7°, 5°$, and $3°$. These values are close to the ones observed by DEMETER on the inner boundary of the trough where density decreases with increasing latitude. It is seen that the ray bends in the direction of increasing density. The higher the gradient, the bigger a displacement at the altitude of DEMETER is seen. The variation of the ray trajectory is smooth within the modeled range of the gradients.

From Figure 6.8b it is seen that the ray deflects by 150 km from the ray for the case with only radial distribution (i.e., no horizontal gradients, Figure 6.7) when the density changes by an order of magnitude over a range $\Delta\theta$ equal to $5°$. Figure 6.8c
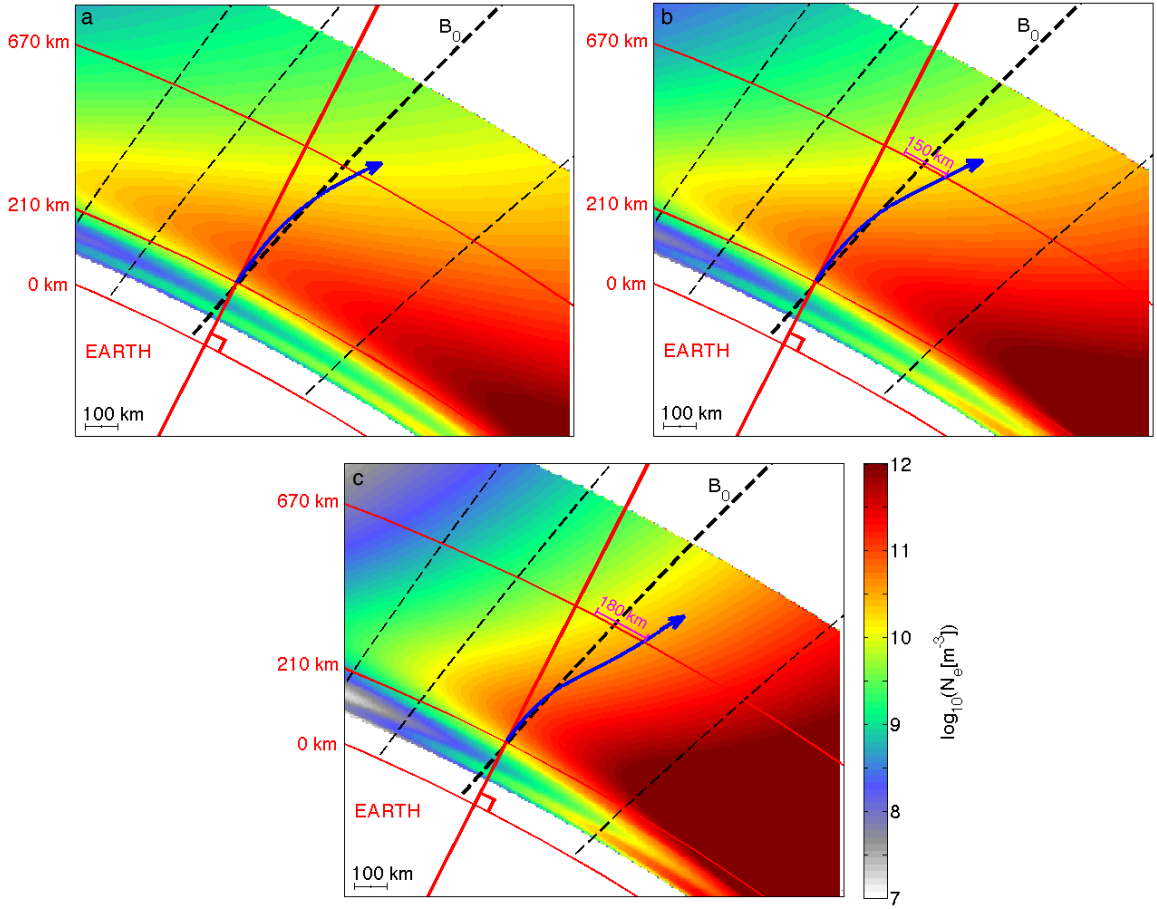
Figure 6.8: Ray tracing with horizontal density for 2 kHz waves. The density changes by a factor of ten over latitude of a) $\Delta\theta = 7°$, b) $\Delta\theta = 5°$, and c) $\Delta\theta = 3°$. The scale of the background density distribution is the same for all plots and is shown only on the last plot. The figure shows that the higher the gradient, the bigger the displacement of the ray from the original position. The displacement from the non-gradient ray (Figure 6.7) is marked on plots b and c, which show the displacements closest to the observed average of 170 km.

demonstrates the deflection is 180 km when $\Delta\theta$ is equal to 3°. These values of the deflection correspond to DEMETER observations with average deflection of 170 km (Figure 6.1a) and constitute the most important conclusion of the presented ray tracing supporting the original hypothesis that the deflection in observations during the night is caused by the horizontal gradients within the trough. Within the assumptions of our model, we also estimated that the gradient should be an order of magnitude change over $\Delta\theta$ equal to 3–5°. This value is reasonable as it is seen from DEMETER data in Figure 6.6. During the day the trough is not present as it was seen in observations, meaning that only radial density profile defines ELF wave propagation in which case ray tracing and full-wave modeling should produce the same result. Consistently, figures 6.1(c,d) demonstrate no significant deviations in observations from modeling during daytime.

Chapter 7

Magnetospheric Propagation Observations

In this chapter we consider the propagation of ELF waves generated by an HF heater further into the magnetosphere. Primarily, the strength and the location of the signal observed in space is discussed, but also some effects created by ELF waves, such as triggered emissions, are shown. For four years of HAARP campaigns, DEMETER observations were performed not only over the HAARP region, but also above the conjugate region which is located between New Zealand and Antarctica. We recorded the first satellite observations of ELF signals generated by an HF heating in the conjugate region (one-hop signal). Additionally, ELF waves were observed over HAARP by DEMETER as they reflected from the conjugate ionosphere and traveled back along the magnetic field lines (two-hop signal). These constitute also the first satellite observations of that sort for ELF waves generated by HF heating.

7.1 One-hop Observations in the Conjugate Region

Similar to overhead DEMETER passes, there are two type of passes over the conjugate region. One type of pass occurs mostly between 20:45 and 22:05 UT or around 9:30

LT. For all seasons these passes correspond to daytime ionosphere both over HAARP and over the conjugate region. Another type of pass occurs mostly between 10:25 and 11:45 UT or around 22:30 LT. For all seasons these passes correspond to a nighttime ionosphere both over HAARP and over the conjugate region. These facts make it easier to separate them and refer to them as either daytime or nighttime passes.

For the majority of experiments a format with 4-sec periodicity (similar to the one shown in Figure 4.2 and described in the two left columns of Table 4.1) was used. The basic considerations for the format selection are the same as for overhead passes (described in Section 4.1). The basic criteria for this format selection was to get the proper distribution of the signal over the conjugate region. However, several other formats were used for special types of experiments, and they are described with specific experiments below.

7.1.1   Case Studies

Figure 7.1 shows a case in which the HAARP-generated ELF signal was received on DEMETER in the conjugate region and on the ground in Juneau, AK, after reflection from the conjugate region. Juneau is located 750 km to the south-east from HAARP. Unfortunately, the data from Chistochina are not available for this time period. For the described experiment, the HAARP array was split into two independent halves: one operating at a 3.25 MHz carrier frequency, while the other operated at 9.5 MHz. Only the signal from 3.25 MHz was received. The ELF modulation pattern for the 3.25 MHz half is similar to the one shown in Figure 4.2, but with pulse frequencies of 571 Hz and 1973 Hz. For all purposes here, they are not different from previously considered 600 Hz and 2 kHz pulses, and are referred to as such hereafter. Similar to the overhead case representation, the map in Figure 7.1 shows the location of the satellite at 670 km. The cyan dot shows the HAARP conjugate point at 670 km, and the yellow dot is the conjugate point on the ground.

The signal received by DEMETER consists of tones, ramps, and triggered emissions. A triggered emission is defined here as a signal with descending and rising frequency following the original tone. Magnified parts of the spectrograms in which

Figure 7.1: (a) A spectrogram with two-hop triggered emissions on the ground. (b) A spectrogram with one-hop ELF pulses and triggered emissions on DEMETER. (c) The strength of the 1973 Hz signal in the conjugate region. The distance on the x-axis is the distance between the location of the satellite and the conjugate point at the altitude of the satellite. The time delay between emissions on DEMETER and at Juneau is approximately constant for the whole pass and equals about 4.1 s.

triggered emissions are seen are shown in Figure 7.2. In addition to the DEMETER
spectrogram, Figure 7.1 shows the strength of an electric field component for pulses
at 1973 Hz averaged over the 1-sec duration of the tones. In addition to the standard
parameters on the x-axis, the distance between the location of the satellite and the
conjugate point at the altitude of the satellite is shown. The signal received at Juneau
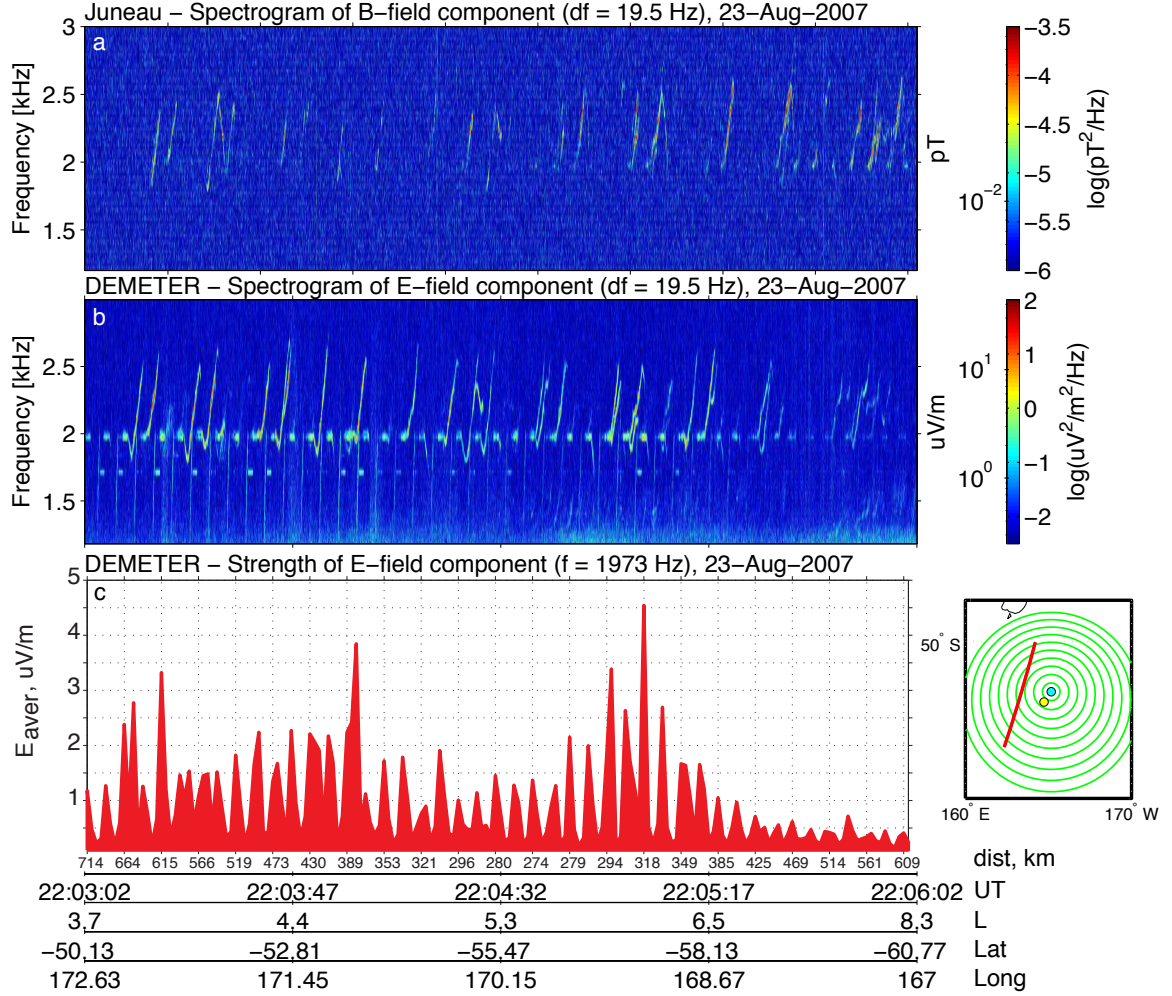consists mostly of triggered emissions and several weak pulses.
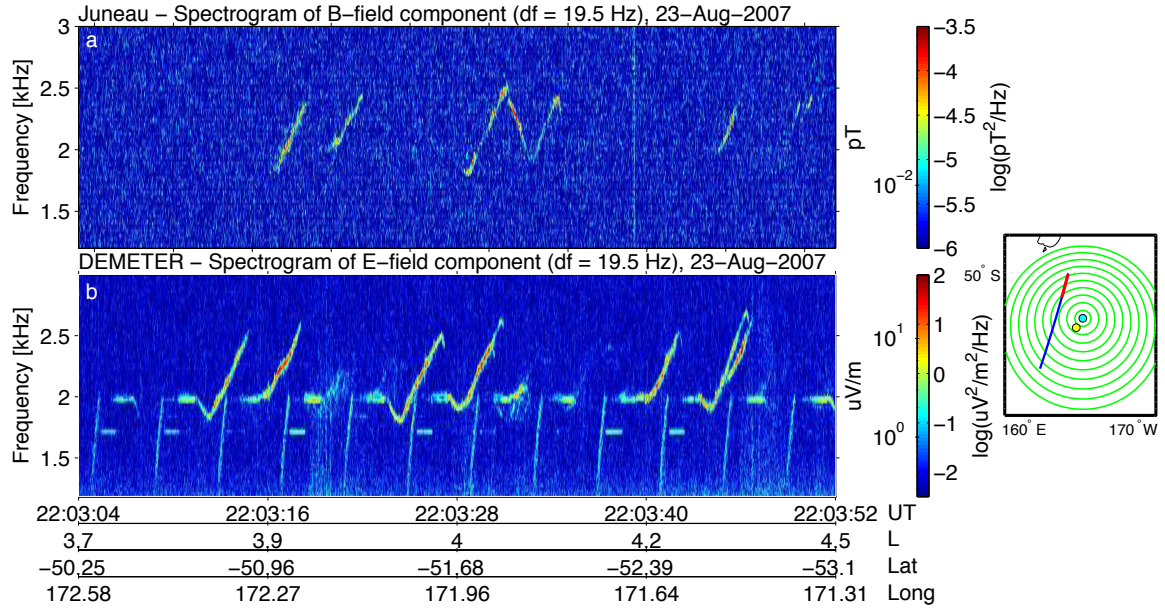
Figure 7.2: (a) A spectrogram with two-hop triggered emissions on the ground. (b) A
spectrogram with one-hop ELF pulses and triggered emissions on DEMETER. The
time delay between emissions on DEMETER and in Juneau is about 4.1 s.

Figure 7.1 shows only Burst mode data, but lower resolution Survey mode data
over a longer path (not presented here) are also available. The data show that 2 kHz
pulses are present on L shells in the range of 3–10, while emissions triggered by these
pulses are found in the range $L = 4$–12. This L range equals about a 1000 km
distance toward the pole from the conjugate point and 1000 km toward the equator
from the conjugate point. No signal is seen on DEMETER when it passes beyond
this range, while the signal at Juneau at the same time (mostly triggered emissions) is
observed. The time delay between one-hop signals on DEMETER and two-hop signals

at Juneau is approximately constant for the whole pass and equals about 4.1 s. These measurements were done by looking at triggered emissions at 2.1 kHz because it is usually possible to juxtapose an emission on DEMETER with the emission associated the same pulse in Juneau. The shape of the strongest part of an emission is preserved and shapes are slightly variable for consequent emissions. Also it is usually possible unambiguously to recognize a series of emissions visually. An example of such a sequence can be seen in Figure 7.2.

In Figure 7.3, another daytime case on 2008-08-25 with triggered emissions is shown. A default pattern with 565 Hz and 2011 Hz pulses of square AM modulation is used. From the ground data in Chistochina, we see the 1st and 3rd harmonics of 565 Hz and 1st harmonic of 2011 Hz. The 2011 Hz signal is stronger than the 565 Hz signal and its harmonics at Chistochina. The 2nd harmonic of 565 Hz is weaker than other harmonics and is below the noise level. This behavior is typical also for ground observations. Surprisingly, the strong triggered emissions in the conjugate region on DEMETER are observed at the 2nd harmonic of 565 Hz. Even though it is hard in this case to see the separate 1130 Hz pulses on DEMETER, it is easy to measure precisely that the starting frequency of triggered emissions is 1130 Hz, which is exactly the 2nd harmonic of 565 Hz. Also, the emissions are observed in the range of $L = 3–8$, which in addition to frequency appears to identify them as the ones triggered by HAARP. On the other hand, just several weak pulses at original 565 Hz can be identified on DEMETER. For instance, a 565-Hz pulse at 21:15:46 UT with $E \approx 1$ μV·m^{-1} can be seen. At 2011 Hz, the pulses are identified within $L = 3–5.5$. Weak emissions triggered by these pulses are seen in the L shell range 4.5–5.2. No pulses or emissions at the 2nd and 3rd harmonics of 2011 Hz are observed on DEMETER. In Chistochina, 2nd and 3rd harmonics of 2011 Hz are observed, with the latter being stronger. The time delay between conjugate hemispheres is 5.2 s for 565 Hz and 3.2 s for 2011 Hz.

Figure 7.4 shows the observations of pure 2 kHz pulses over a long distance on 2010-10-02. The 2-kHz pulses appear at about $L = 2.5$ and abruptly stop at $L = 5$. The zone of signal reception is highly asymmetrical with respect to the conjugate point. No triggered emissions are seen on DEMETER. No emissions or two-hop signals are seen on the ground in Chistochina for the period of the DEMETER pass.
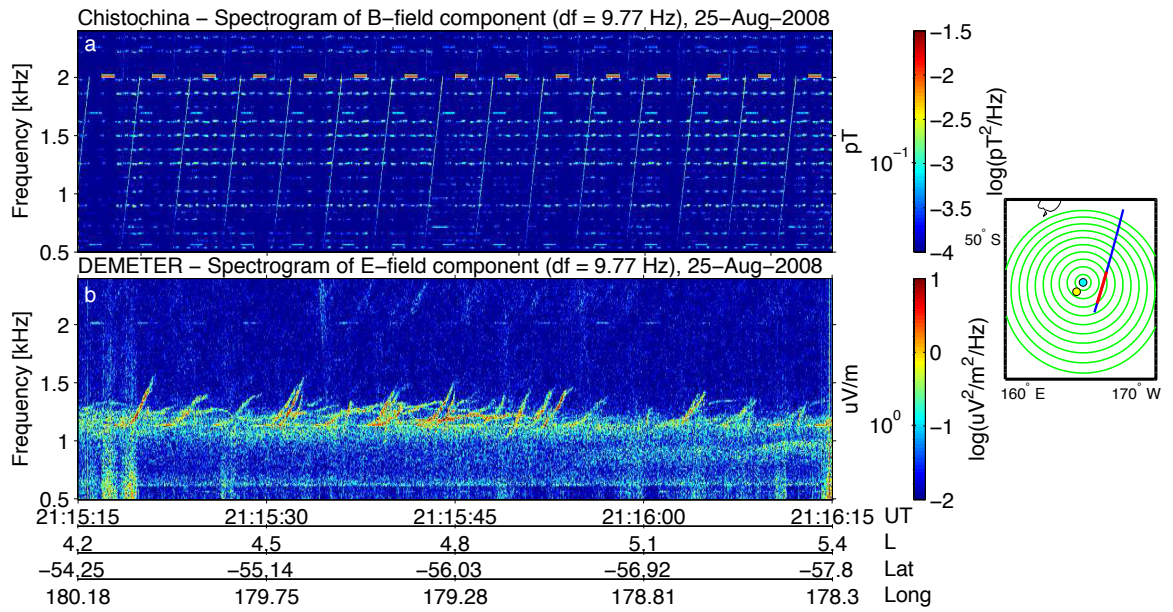
Figure 7.3: (a) A ground spectrogram of the original signal. The 1st and 3rd harmonics of 565 Hz are weaker than 2011 Hz. The 2nd harmonic of 565 Hz is below the noise level. (b) DEMETER spectrogram in the conjugate region. The 2nd harmonic of 565 Hz appears to produce triggered emissions. A weak 2011 Hz signal and triggered emissions by that signal are also observed.

However, weak triggered emissions and two-hop signals at 2 kHz are seen at Chistochina just 10 minutes after the DEMETER pass (not shown here). As in the previous cases, the time delay does not vary significantly as the satellite moves from low to high L-shells. Two 20-second periods of the considered pass with good SNR are compared in Figure 7.5. It is clearly seen that the time delay does not change significantly.
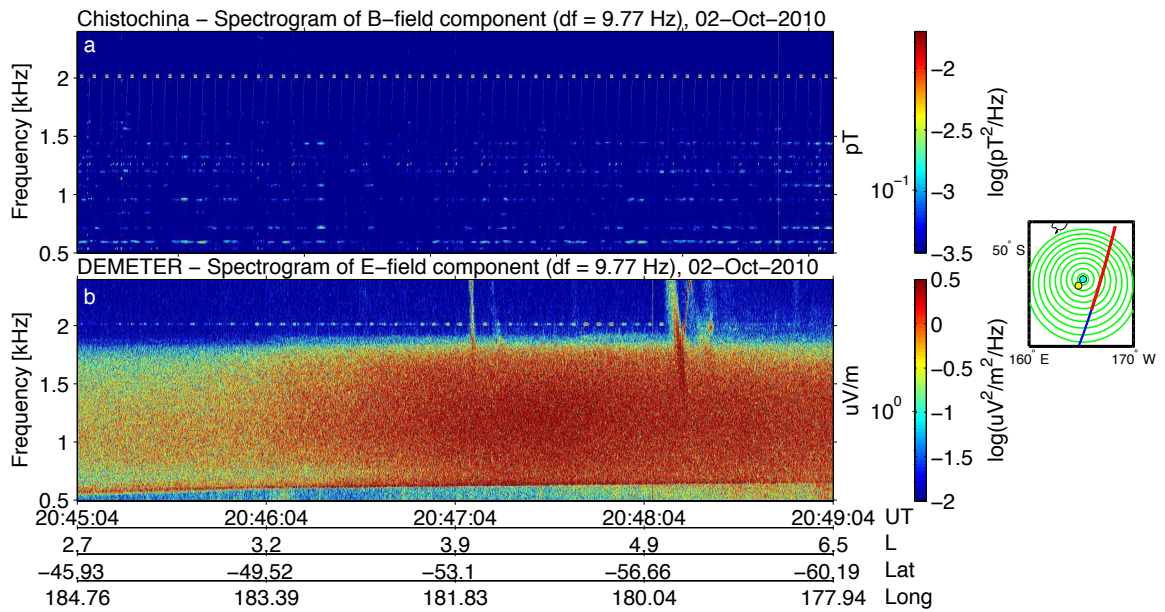
Figure 7.4: (a) A ground spectrogram of the original signal. (b) DEMETER spectrogram in the conjugate region. One-hop signal without triggered emissions is observed over the long part of the path. The signal abruptly stops at $L \approx 5$.

Another interesting one-hop observation occurred at daytime on 2008-03-16. On this day not only DEMETER observations in the conjugate region were carried out, but also the research vessel R.V. Tangaroa was set to record ELF signals as it was passing through the region. The velocity of the ship is negligible in comparison with the satellite, and here we treat it as a stationary ground receiver. The part of the observations in which both the ship and the satellite recorded HAARP pulses is shown in Figure 7.6. The default pattern was used. The signal on the ship is repeatedly
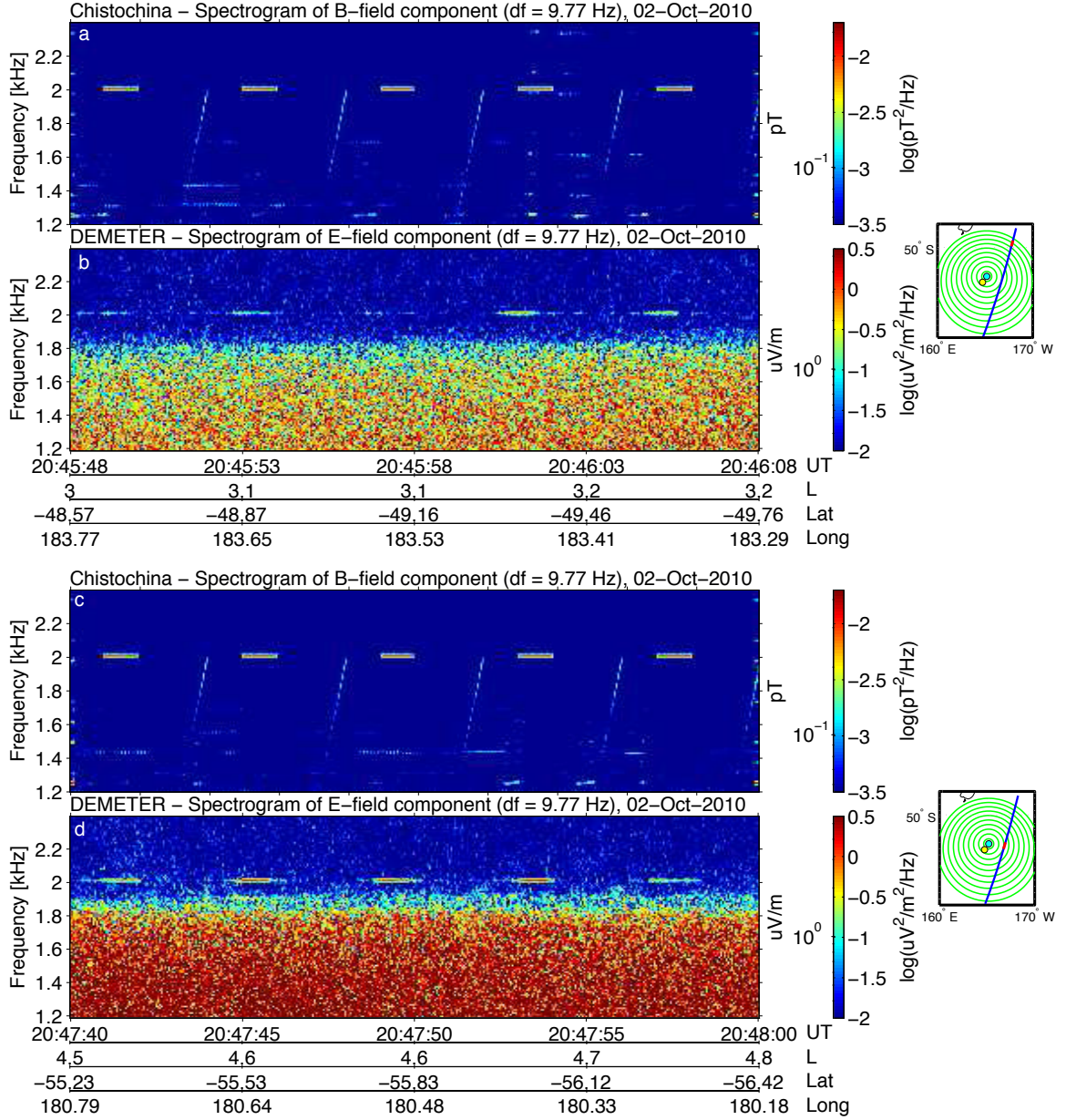
Figure 7.5: (a,c) Ground spectrograms of the original signal. (b,d) DEMETER spectrogram in the conjugate region. Two pieces of the pass marked by red on the maps are shown. The time delay for a one-hop signal is constant throughout the whole pass when $L = 2.5$–5.

observed over at least several minutes. However, some breaks in the pulse observations occurred. Only two pulses are observed on DEMETER at 21:00:24 and 21:00:28 UT. Even though the distance between DEMETER and Tangaroa is large, as seen from the map, the timing of pulses is equal within the precision of 0.1 s.
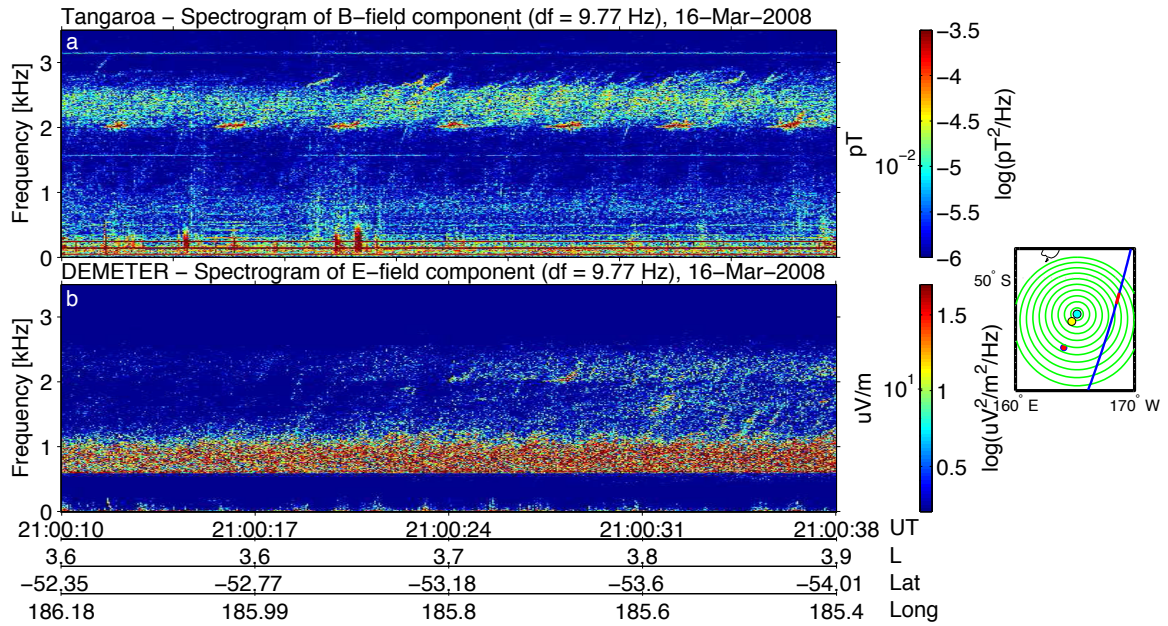
Figure 7.6: (a) A ground spectrogram at the ship Tangaroa. The location of the ship is marked by red dot. (b) A spectrogram at DEMETER. One-hop signal is seen repeatedly on the ship, while on DEMETER only two pulses at 21:00:24 and 21:00:28 UT are observed. It is hypothesized that the signal on DEMETER is observed within a duct. To a location on the ground, the signal propagates in the Earth-ionosphere waveguide after propagation in one or more ducts.

7.1.2 Aggregate Study

For four years of HAARP-DEMETER experiments over 2007–2010, 77 transmissions during nighttime and 101 transmission during daytime were performed by HAARP. The maps of DEMETER passes during this transmissions are shown in Figure 7.7.

DEMETER was recording in the Burst mode during these passes. The maps show that the coverage is comparable to that for overhead experiments.
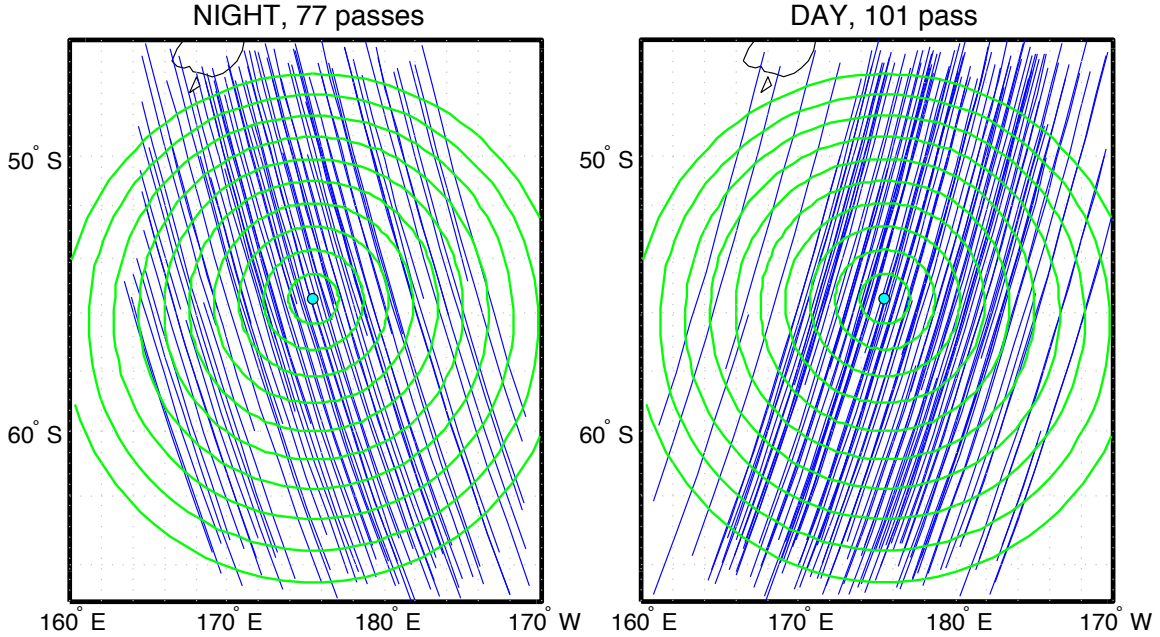
Figure 7.7: Maps of DEMETER passes in the conjugate region for which HAARP transmitter was operating in 2007–2010. Left side shows nighttime passes around 22:30 LT, while right side shows daytime passes around 09:30 LT.

Table 7.1 shows the summary of observations in the conjugate region. This summary is made through manual analysis of the spectrograms on DEMETER. In the section above, several cases with signal detection during daytime were discussed. In 15 cases out of 101, the pulses at 2 kHz are seen. In 3 out of 15 cases, triggered emissions are also present in addition to pulses. The case on 2008-08-25 with triggered emissions from the 2nd harmonic of 565 Hz is not included in these statistics. In nighttime, only 7 cases with pulses out of 77 observations are seen. The highest signal during daytime is 9.5 μV·m^{-1}, while during the nighttime it is around 1 μV·m^{-1}. This finding is opposite to that found from overhead observations, and opposite to that expected from ionospheric absorption characteristics. Therefore, propagation loss through the ionosphere is not a dominant factor for signal strength in the conjugate region.

Table 7.1: Summary of conjugate case studies for 2 kHz

	Number of nighttime cases	Number of daytime cases
HAARP transmits and DEMETER records	77	101
Signal Detected	7	15
Triggered Emissions	0	3

Overall, the low signal-to-noise ratio in the conjugate region limits the ability to do an aggregate study similar to that done for overhead passes. The automatic detection algorithm produces too many either false positive or false negative detections, if only one threshold in SNR is used for all cases. For daytime, it is possible to go manually through the cases identified in Table 7.1 and adjust the threshold for every case. This adjustment allows the use of the automatic detection algorithm for 7 out 15 daytime cases with the highest SNR. These 7 cases are used to create a database of pulses similar to that created for the overhead analysis. The database is very sparse in comparison with the overhead database. Nevertheless, the average E-field distribution can be plotted with the technique described in Section 5.3. The resulting distribution of the signal strength is shown in Figure 7.8. The distribution is at the altitude of the satellite. The origin of coordinates correspond to the vertical from the HAARP conjugate point on the ground to the satellite altitude. The white circle shows the location of the conjugate point at 670 km altitude of DEMETER.

Even though it is hard to make general conclusions from such sparse data, several facts can be noticed. The highest signal is observed in the region displaced about 300 km to the north-east from the conjugate point. About 200 km toward the pole and 200 km to the east. We can divide the space of the plot in two halves: one from the conjugate point latitude to the equator and another from the conjugate point latitude to the pole. It is seen that the signal is observed more often and is higher in the equatorial half.

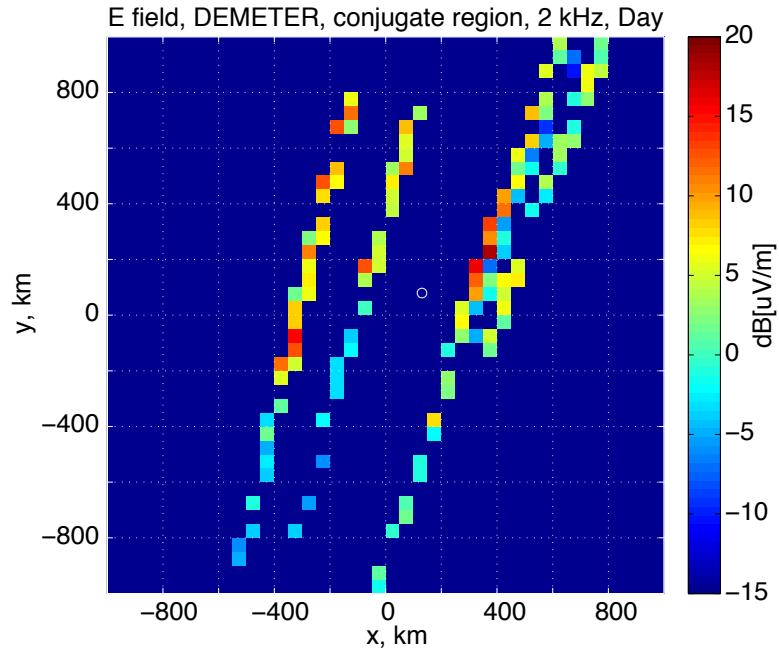Figure 7.8: Average 2 kHz signal during daytime at DEMETER altitude for years of 2007–2010. The white circle shows the location of the conjugate point at DEMETER altitude. The highest signal is displaced about 300 km to the north-east from the conjugate point. Overall, the signal is not symmetrical in the north-south direction. It is observed more often and is higher in the upper half than in the lower half.

7.2 Two-hop Observations

An analysis of two-hop observations on the ground from HAARP is carried out in detail in the Ph.D. dissertation of *Golkowski* [2008] and associated publications of *Golkowski et al.* [2008, 2009]; *Golkowski et al.* [2010]. In DEMETER observations, only one case with two-hop signals have been found for four years of experiments with HAARP. The case occurred during daytime on 2007-08-30 and is presented in Figures 7.9 and 7.10.

The transmitted ELF pattern for this case is similar to the one on 2007-08-23 in Section 7.1.1. The two-hop signal originates from the 1973 Hz pulses. Figure 7.9 shows data from two ground-based VLF receivers and DEMETER. The part of the pass presented in the figure is close to the Juneau receiver, the location of which is marked by a red dot on the map. No two-hop signal is seen at either ground receiver. In fact, no two-hop signal is seen on the ground for the whole duration of the DEMETER pass. On the other hand, the two-hop signal is observed on DEMETER in the range of $L = 2.2$–5.8 which corresponds to about 2000 km extent along the pass. As the satellite moves, triggered emissions appear and disappear, but the pulses are seen all the time. The most striking observation is that the triggered emissions are seen at as low latitude as 44°N, or $L = 2.2$. Figure 7.10 demonstrates a low latitude part of the pass. Triggered emissions stop at 20:16:30 UT but then reappear one more time at 20:17:00 UT. The emissions at $L = 2.5$ are no weaker then emissions at $L = 5$. The time delay is essentially the same along the whole pass, which is similar to one-hop observations.

7.3 Discussion

Since the one-hop and two-hop observations of ELF signal generation via HF heating are the first low-earth-orbit satellite observations of this phenomenon, we can only compare them with observations of ELF waves generated by other means. An active experiment conducted with a transmitter at Siple station, Antarctica ($L \simeq 4.3$) is of the closest kind in which successful conjugate observations were done. *Carpenter and*
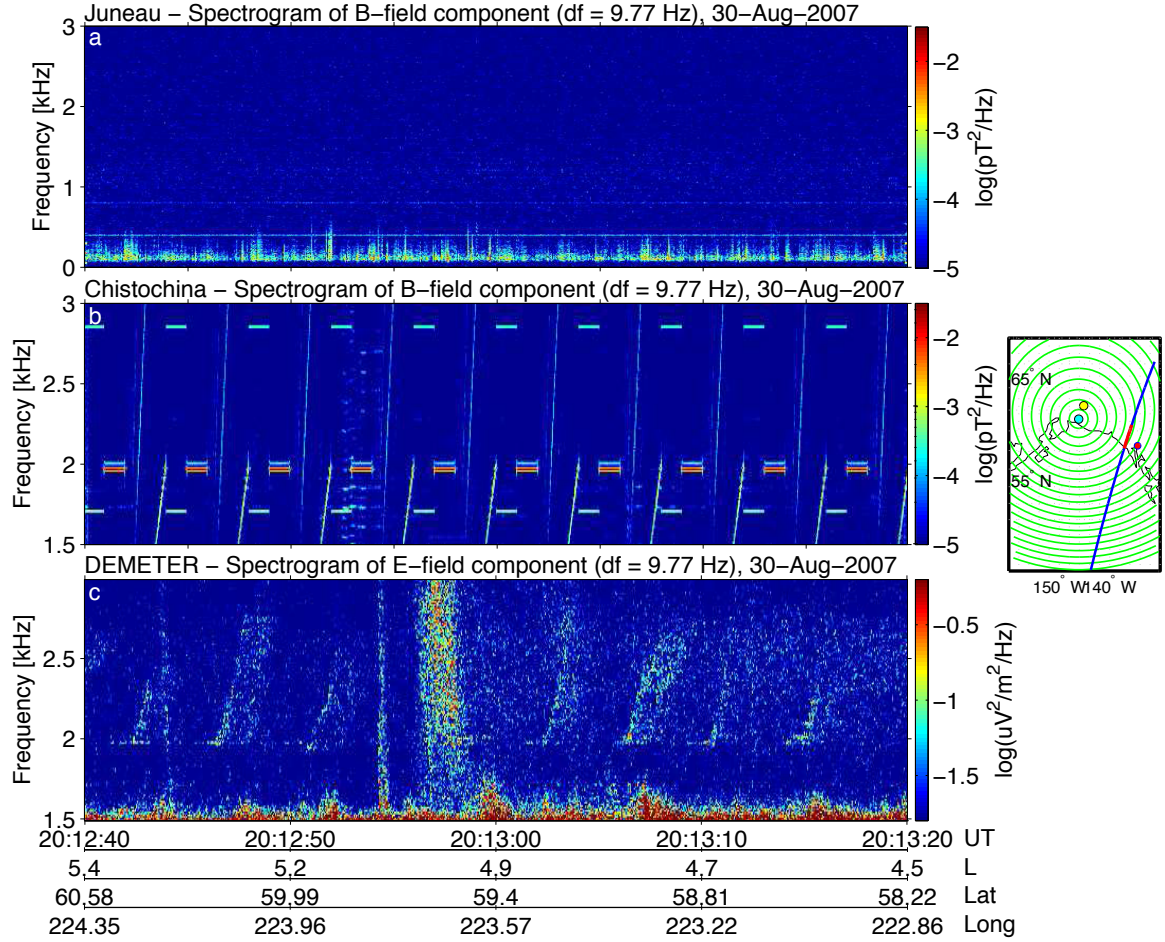
Figure 7.9: Two-hop signal on DEMETER, part 1. (a) A ground spectrogram at Juneau, the location of which is marked by a red dot on the map. (b) A ground spectrogram in Chistochina. (c) A DEMETER spectrogram. The two-hop signal is seen only on DEMETER and not at the ground stations.
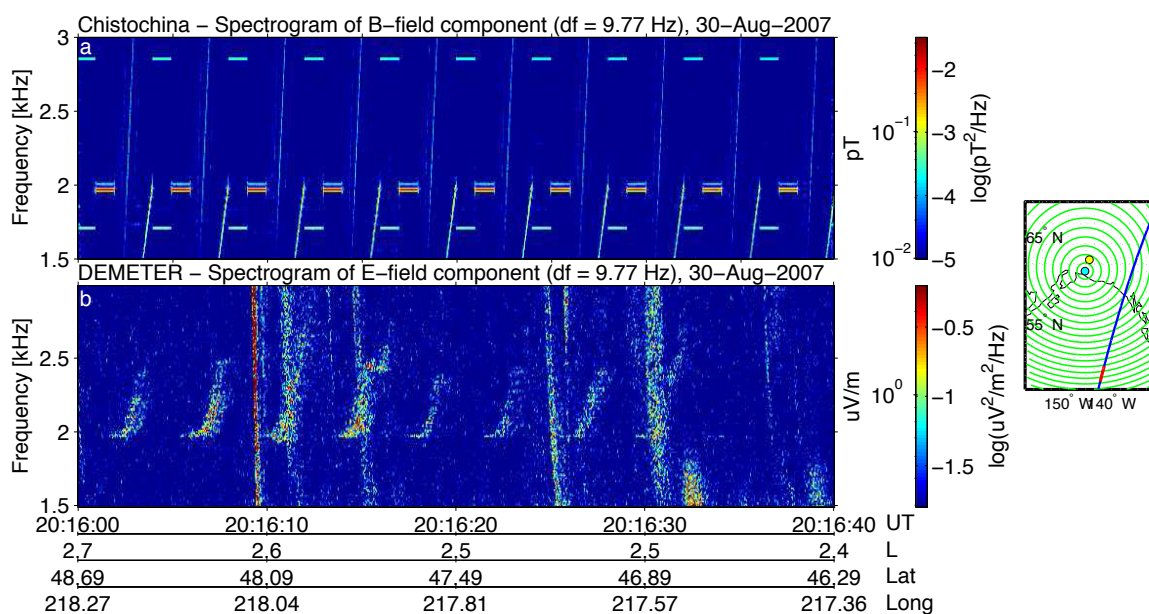
Figure 7.10: Two-hop signal on DEMETER, part 2. (a) A ground spectrogram in Chistochina. (b) A DEMETER spectrogram. Reflected pulses and triggered emissions are seen on DEMETER over the L shell range 2.2–5.8.

Miller [1976, 1983] showed that the propagation of ELF waves mostly occurred in the outer plasmasphere or in the region of steep plasmapause density gradients. The experimental data from Imp 6 satellite [*Inan et al.*, 1977a,b] showed the evidence of plasmapause guiding of ELF waves. For naturally generated ELF waves, it was found that as these waves propagate from the conjugate region to the Alouette 1 satellite at 1000 km, they tend to cut off abruptly as the satellite moved poleward through the plasmapause [*Carpenter*, 1968]. Also, recently *Golkowski* [2008] found from ground measurements of HAARP signals that triggered emissions occur when the HAARP *L*-shell is within the plasmasphere.

Guiding of ELF waves by the plasmapause was shown via raytracing by *Inan and Bell* [1977]. *Inan and Bell* [1977] suggest that the guidance that occurs is a form of gradient trapping of ELF wave energy. They discuss the possibility of guiding at both the inner and outer edges of the plasmapause. Imp 6 satellite observations resembled the guidance by cold plasma density gradients located at the inner edge of the plasmapause. For 2.5 kHz raytracing, *Inan and Bell* [1977] show that as the rays descend to the ionospheric altitudes in the conjugate region, they diverge inward from the plasmapause starting at 3000–4000 km altitude. Specifically, they demonstrate numerically that for $L = 4$, the rays of ELF waves reach the lower ionosphere as much as 5° lower in latitude than the plasmapause or 500–600 km in horizontal distance.

Aggregate DEMETER results are consistent with the theoretical results of *Inan and Bell* [1977]. The guiding by the plasmapause and divergence of ELF waves toward lower latitudes as they descend to the ionosphere explains why the peak intensities are observed not around the conjugate point and why the intensities substantially drop beyond $L \sim 5$. This situation applies to the cases when HAARP is within the plasmasphere. Since HAARP is located at $L = 4.9$, we can expect that it is within the plasmashphere on days with low or moderate magnetic activity measured by K_p-indicies.

In DEMETER observations the signal in the conjugate region was detected in 15% of cases during daytime and in 9% of cases during nighttime. The daytime conditions appear to be preferable for the propagation of ELF waves to the conjugate region despite the fact that injection of those waves into the magnetosphere is less effective

during daytime as discussed in Chapter 5. A similar tendency was reported before in Siple experiment for ground-based observations [*Carpenter and Miller*, 1976] and for space observations [*Inan et al.*, 1977b].

The explanation of why the signal in the conjugate region is often seen over a large region was first proposed by *Bell et al.* [1983]. They observed similar effect in EXOS-B satellite measurements at the altitude of about one Earth's radius. *Bell et al.* [1983] proposed that the signal on the satellite is the result of backscattering of ELF waves by ionospheric density irregularities after their ducted propagation in the magnetosphere. After backscattering, the wave energy spreads over wide range of wave normal angles which probably complicates their effective penetration down to the ground. The constant time delay also supports the idea of the propagation of ELF waves in the magnetosphere along one or several close paths (or ducts). On the other hand, for the 2008-03-16 case in which the signal is seen repeatedly on Tangaroa ship and only two pulses are seen on DEMETER, the backscattering is probably low and the signal penetrates to the ground through one or more ducts. In such a situation, we may have the observations of a very rare case in which the satellite passes within a duct of horizontal extent of about 50 km and observes only two pulses within this duct. The condition of low backscattering also explains cases (not presented here) when two-hop signals are seen on the ground but not by DEMETER in overhead passes because the probability of DEMETER passing through a narrow duct is very low.

The observation of the large region of two-hop signal on 2007-08-30 on DEME-TER and the absence of signal on ground stations also goes along with the idea of backscattering from the ionosphere (first, from the conjugate ionosphere and then from the overhead ionosphere). However, with only two-hop data we cannot exclude the possibility that ELF waves do not travel all the way to the conjugate hemisphere but are Magnetospherically Refected (MR) ELF whistler waves [*Bortnik*, 2004]. If such is the case, such waves should all be reflected in about the same region and travel along close paths to have equal time delay as observed.

Chapter 8

Summary and Future Work

'In matters of the intellect follow your reason as far as it will take you, without regard to any other consideration... and do not pretend that conclusions are certain which are not demonstrated or demonstrable. That I take to be the agnostic faith, which if a man keep whole and undefiled, he shall not be ashamed to look the universe in the face, whatever the future may have in store for him.[1]*'*

In this work we primary discussed the propagation of ELF waves generated by the HAARP HF heater in the region of about 1000 km around the source at 75 km altitude. In this region, we considered low-earth-orbit DEMETER satellite observations and theoretical simulations of physical effects. We also considered a set of experiments in the conjugate region to which ELF waves propagate predominantly along the Earth's magnetic field lines. Below we briefly summarize the main results and suggest possible future work.

8.1 Propagation around the Source

Several new key features of ELF wave propagation from the source in the lower ionosphere are discussed in this work. The first and most important feature is the

---

[1]Thomas Huxley, 1889

column of radiation with the size comparable to the source region (50–100 km). We distinguish it on the basis of the E-field strength, which is about 100–150 μV·m^{-1} at 2 kHz on average, and refer to it as Region 1. We show that on average the location of Region 1 is displaced by about 100 km to the south from HAARP field line at DEMETER satellite altitude during the nighttime. On the other hand, during the daytime there is no substantial north-south displacement from the HAARP field line. The simulations with a horizontally homogeneous full-wave model reproduce well the size of the column but produce up to a 100 km displacement in the other direction, to the north. We propose that the displacement in observations during the night is caused by the horizontal electron density gradient within the main ionospheric trough. Using ray tracing simulation we estimate that the gradient should be an order of magnitude change in density over a latitude range equal to 3–5°. The column is an important feature for the ELF wave injection into space. The size and location of the column and the magnitude of the E-field can be used in the future evaluation of the effects of injected ELF wave in the magnetosphere. The main ionospheric trough in plasma density is an important parameter of the medium above HAARP not only for ELF observations but for other types of experiments too. We found that the trough prominently occurs over HAARP during the nighttime in at least 50% cases.

Additionally, on the basis of the E-field strength, the E-field fall-off from the center, and the presence of the signal in the regions for the daytime versus nighttime we distinguish three different regions of ELF illumination, referred to as Regions 1, 2 and 3. Region 2 extends horizontally up to about 300 km from the center of the Region 1, while the signal in Region 3 is observed up to 1000 km from the center of the Region 1. Region 2 is distinguished from Region 3 by higher signal intensity and by faster fall-off of the signal level in Region 2. Region 3 appears only for 2 kHz nighttime observations and not for 600 Hz observations. This result makes Region 2 different from Region 3 not only quantitatively but also qualitatively.

We propose physical interpretation for the differences of the signal in Regions 2 and 3. The ELF waves observed on DEMETER in Region 3 are at first launched in the Earth-ionosphere waveguide. Only the waves above the critical cutoff frequency of the waveguide propagate effectively and in multiple modes. The 2 kHz frequency

is just above the critical frequency while the 600 Hz frequency is below it. As ELF waves propagate within the waveguide, they partially leak through the ionosphere up to the satellite. The leakage is more efficient during the nighttime when ionospheric absorption is substantially lower then in the daytime. On the other hand, ELF waves in Region 2 can reach a satellite without regard to the lower boundary of the waveguide as shown in simulations. This feature is called direct propagation from the source to the DEMETER satellite, and explains the different features of the waves in the observations. Region 2 might still be important for wave injection into space because the values of the fields are still substantial (about ten times lower E-field than in Region 1). Region 3 may be important for long distance submarine communication. The frequencies above the critical cutoff frequency of the waveguide can be used in propagating modes, while the frequencies below this critical frequency (or very long wavelengths) can be used in evanescent modes.

In future work, it would be interesting to investigate the space injection of ELF waves with the formats of modulation different from AM. An alternative type of modulation which was studied in ground observations of HAARP signals [*Cohen et al.*, 2008, 2010a,b] and produced an increase of the signal strength is a "geometric modulation" (geomod). In geometric modulation the power of the HF carrier is kept constant, but the HF beam is moved periodically with ELF frequency [*Cohen*, 2009]. Some initial results that were obtained with DEMETER measurements of geomod signals [*Cohen et al.*, 2011] are shown in Figure 8.1. However, there were not enough measurements to make final experimental conclusions about the advantages of this modulation technique for space injection.

For submarine communication, the lower the frequency, the deeper the penetration under water. The lowest detected signal from HAARP by DEMETER and ground receivers was 95 Hz. There were only several experiments made in this frequency range. An example of such reception is shown in Figure 8.2. For such frequencies, the time delay in the ionospheric plasma is noticeable and is about 1 s for 155 Hz in the case shown. More measurements are needed to estimate the region of the detected signal. However, initially it is possible to note that only the TEM mode propagates in the Earth's-ionosphere waveguide. Whether it is possible to rely on this mode or
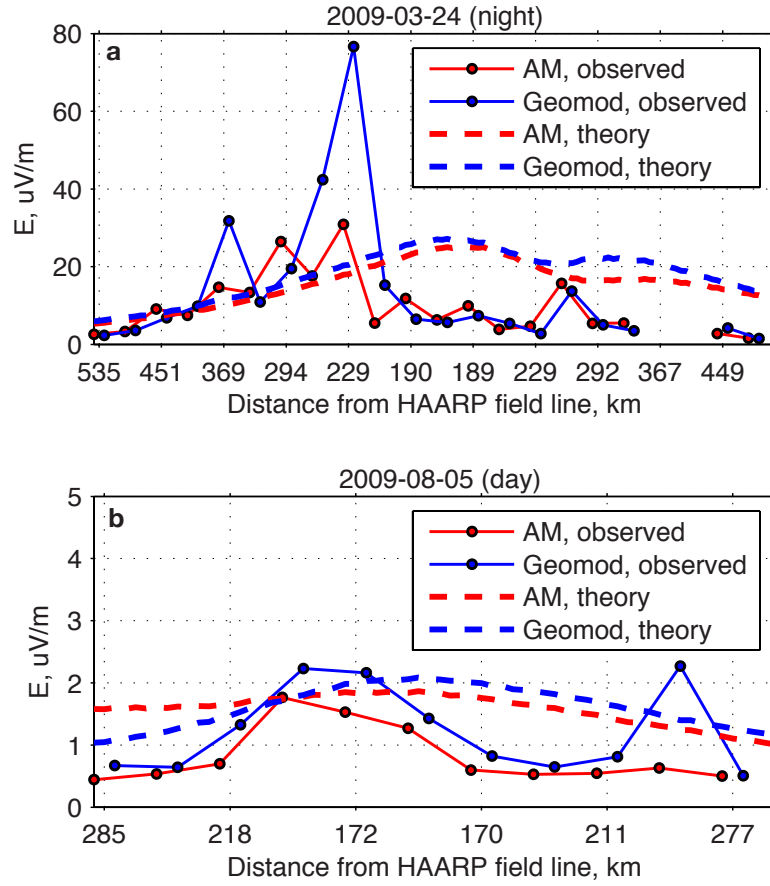
Figure 8.1: Initial results with geometric modulation [*Cohen et al.*, 2011]. Comparison of electric field strengths at 670 km in observations and theory for specific DEMETER passes during the nighttime (a) and the daytime (b). Frequency is 1 kHz.

on higher order evanescent modes needs to be established in future experiments.
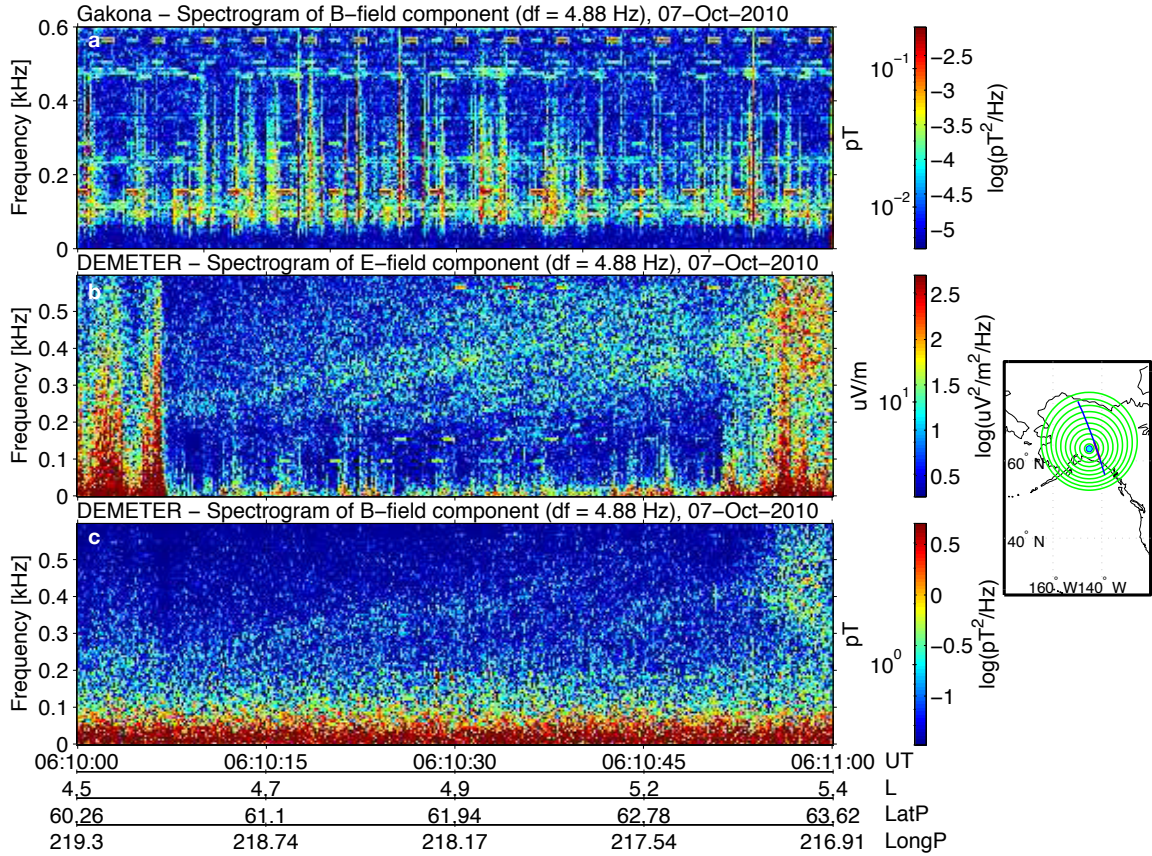
Figure 8.2: Observations of 95 and 155 Hz. (a) A ground spectrogram. (b) A spectrogram of wave electric field on DEMETER. (c) A spectrogram of wave magnetic field on DEMETER.

8.2 Magnetospheric Propagation

We performed the first satellite observations of ELF waves generated by an HF heater over multiple days for four years. These observations were the first observations of ELF waves created by an HF heater in the conjugate region. Even though the number of successful receptions is too low for proper statistical analysis, some general

trends are established. First is the fact that daytime is preferential for ELF wave propagation. The signal in the daytime is observed almost two times more often than in the nighttime, and triggered emissions are observed only in the daytime. The second important conclusion is that the region with the strongest signal is displaced about 300 km towards the equator and the signal is overall higher toward the equator than toward the pole. We hypothesized that this can be the result of plasmapause guiding. This hypothesis is also supported by previously performed ray tracing. The third important observational fact is that one/two-hop signals are observed over a long range of distances (> 1000 km) and over a wide range of L-shells. Despite the wide range of L-shells, the time delay is constant. This result suggests that the propagation in the magnetosphere is within the narrow range of L-shells or within a duct, and the wide range in the observations is the result of ELF waves backscattering from density irregularities in the ionosphere. The backscattering probably does not always takes place. In such cases the signal is either not observed at all or can be observed within a narrow range of L-shells if a satellite happens to pass through the right narrow region (≈ 50 km).

For future work, it is worth noting that among the four cases of observations of triggered emissions on DEMETER, two of them are produced with the modulation format in which two HF frequencies were used (described in Section 7.1.1). The second higher HF frequency produced only weak, or no, ELF signal. Such format was used in about 10% of cases. This result might be only pure coincidence that two cases with triggered emissions were observed, however it is interesting to note this fact for possible future investigations.

In the future, it would also be interesting to conduct more observations of HF-heater generated ELF signals in the magnetosphere where the interaction of ELF waves and energetic particles occurs. Several experiments with HAARP and Cluster spacecrafts have been performed. However, they are not enough to properly evaluate the extent of the region that is illuminated by HAARP. One exceptional case is worth to mention here. In this case, the HAARP signal is at first registered on one of the Cluster spacecrafts and 20 minutes later on a DEMETER overhead pass. As usual, the signal was also recorded on the ground at Chistochina. Figure 8.3 shows the

spectrograms from Chistochina, Cluster and DEMETER for two 20 second periods with best SNR. The signal on Cluster is seen within $L = 5.0$–6.4 with peak around $L = 5.6$. The signal on DEMETER is seen within $L = 2.9$–5.2. It is sensible to assume that natural conditions in the magnetosphere do not change substantially over the period of 20 min when there is no high geomagnetic activity. K_p indices did not exceed the magnitude of 4 for the day before observations. Therefore, we can assume that propagation conditions also did not change over 20 min. For two pulses on the ground spectrograms marked by arrows, the magnetic field is about 1 pT. For the same pulses the electric field on Cluster and DEMETER is 1 μV·m^{-1} and 20 μV·m^{-1} correspondingly. Also, it is interesting to note that the time delay between Cluster and original pulses for about 2 kHz is less than 0.1 s. There is a lot of interesting information to learn in the future if more multisatellite experiments can be conducted.
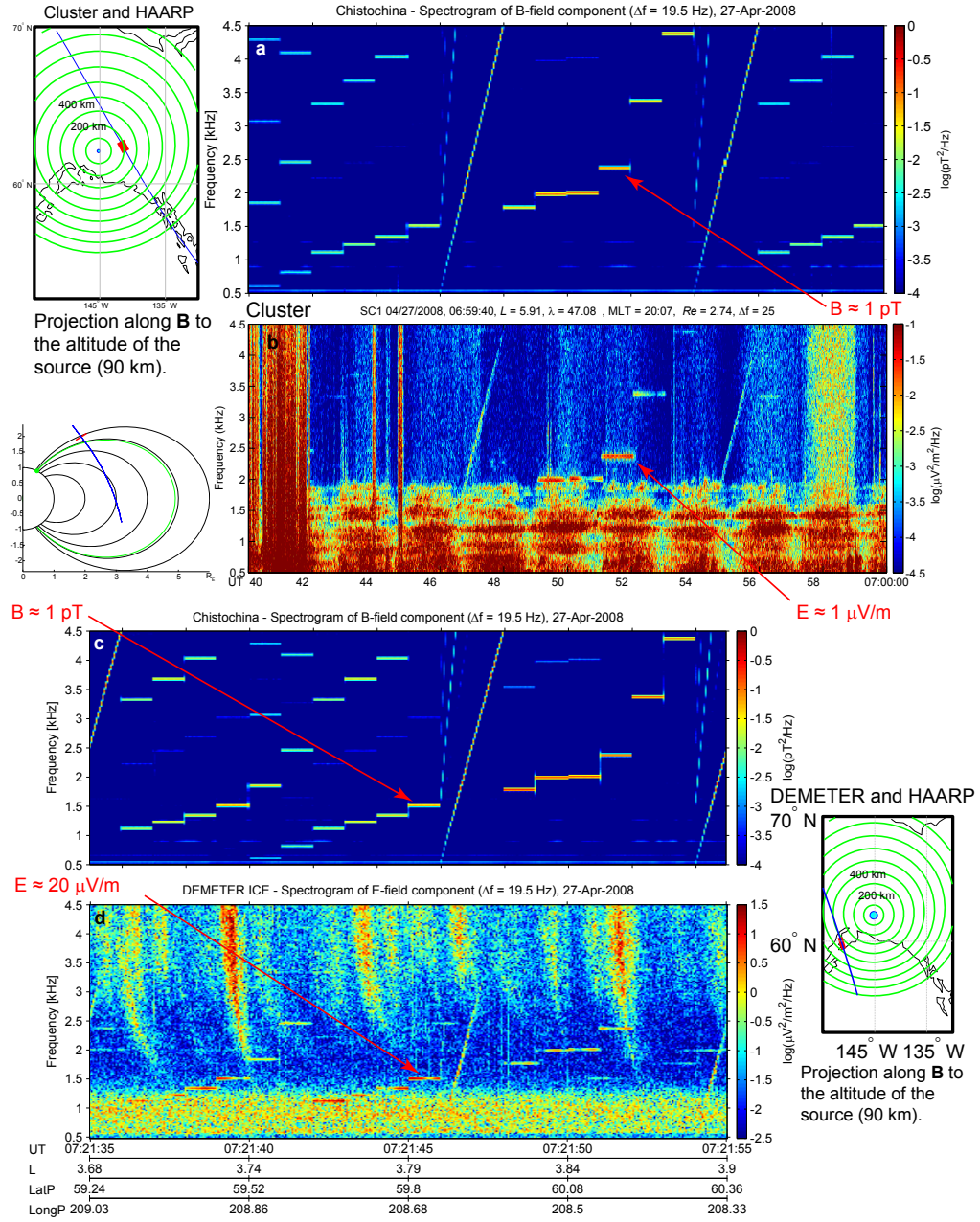
Figure 8.3: (a,c) Ground spectrograms of the original signal. (b) Cluster spectrogram. (d) DEMETER overhead spectrogram. Cluster pass occurred 20 min before DEMETER pass. The pattern was repeated every 20 s. Maps with circles show the positions of the satellites projected along Earth's magnetic field lines to the same horizontal plane of the source at 90 km.

Bibliography

Abel, B., and R. M. Thorne (1998a), Electron scattering loss in Earth's inner magnetosphere 1. Dominant physical processes, *J. Geophys. Res.*, *103*, 2385–2396, doi:10.1029/97JA02919.

Abel, B., and R. M. Thorne (1998b), Electron scattering loss in Earth's inner magnetosphere 2. Sensitivity to model parameters, *J. Geophys. Res.*, *103*, 2397–2408, doi:10.1029/97JA02920.

Alpert, Y., V. Ginzburg, and E. Feinberg (1953), *Propagation of radiowaves [in Russian]*, Gostehizdat, Moscow.

Appleton, E. (1932), Wireless studies of the ionosphere, *Electrical Engineers, Journal of the Institution of*, *71*(430), 642 –650, doi:10.1049/jiee-1.1932.0144.

Barr, R., and P. Stubbe (1984), ELF and VLF radiation from the polar electrojet antenna, *Radio Sci.*, *19*(4), 1111–1122.

Barr, R., M. T. Rietveld, H. Kopka, P. Stubbe, and E. Nielsen (1985), Extra-low-frequency radiation from the polar electrojet antenna, *Nature*, *317*(6033), 155–157.

Barr, R., P. Stubbe, M. T. Rietveld, and H. Kopka (1986), ELF and VLF signals radiated by the 'polar electrojet antenna' - Experimental results, *J. Geophys. Res.*, *91*, 4451–4459, doi:10.1029/JA091iA04p04451.

Barr, R., P. Stubbe, and H. Kopka (1991), Long-range detection of vlf radiation produced by heating the auroral electrojet, *Radio Sci.*, *26*(4), 871–879.

Barr, R., P. Stubbe, and M. T. Rietveld (1999), ELF wave generation in the iono-sphere using pulse modulated HF heating: initial tests of a technique for increas-ing ELF wave generation efficiency, *Annales Geophysicae*, *17*(6), 759–769, doi:10.1007/s00585-999-0759-0.

Barr, R., D. L. Jones, and C. J. Rodger (2000), ELF and VLF radio waves, *Jour-nal of Atmospheric and Solar-Terrestrial Physics*, *62*, 1689–1718, doi:10.1016/S1364-6826(00)00121-8.

Bartels, J., N. H. Heck, and H. F. Johnston (1939), The Three-Hour Index Measuring Geomagnetic Activity, *Terrestrial Magnetism and Atmospheric Electricity (Journal of Geophysical Research)*, *44*, 411–454, doi:10.1029/TE044i004p00411.

Bell, T. F., U. S. Inan, I. Kimura, K. Hashimoto, H. Matsumoto, and T. Mukai (1983), EXOS-B/Siple station VLF wave-particle interaction experiments. II - Transmitter signals and associated emissions, *J. Geophys. Res.*, *88*, 295–309, doi:10.1029/JA088iA01p00295.

Belyaev, P. P., D. S. Kotik, S. N. Mityakov, S. V. Polyakov, V. O. Rapoport, and V. Y. Trakhtengerts (1987), Generation of electromagnetic signals at combination frequencies in the ionosphere, *Radiophysics and Quantum Electronics*, *30(2)*, 189–206.

Bernstein, S., M. Burrows, J. Evans, A. Griffiths, D. McNeill, C. Niessen, I. Richer, D. White, and D. Willim (1974), Long-range communications at extremely low frequencies, *Proceedings of the IEEE*, *62*(3), 292 – 312, doi:10.1109/PROC.1974.9426.

Berthelier, J.-J., M. Malingre, R. Pfaff, E. Seran, R. Pottelette, J. Jasperse, J.-P. Lebreton, and M. Parrot (2008), Lightning-induced plasma turbulence and ion heating in equatorial ionospheric depletions, *Nature Geoscience*, *1*, 101–105, doi:10.1038/ngeo109.

Berthelier, J. J., et al. (2006), ICE, the electric field experiment on DEMETER, *Planet. Space Sci.*, *54*, 456–471, doi:10.1016/j.pss.2005.10.016.

Bibl, K., and B. W. Reinisch (1978), The universal digital ionosonde, *Radio Science*, *13*, 519–530, doi:10.1029/RS013i003p00519.

Bilitza, D., and B. W. Reinisch (2008), International Reference Ionosphere 2007: Improvements and new parameters, *Advances in Space Research*, *42*, 599–609, doi:10.1016/j.asr.2007.07.048.

Born, M., E. Wolf, and A. Bhatia (1999), *Principles of Optics: Electromagnetic Theory of Propagation, Interference and Diffraction of Light*, Cambridge University Press.

Bortnik, J. (2004), Precipitation of radiation belt electrons by lightning-generated magnetospherically reflecting whistler waves, Ph.D. thesis, Stanford University.

Bracewell, R. (2000), *The Fourier transform and its applications*, McGraw-Hill series in electrical and computer engineering, McGraw Hill.

Budden, K. (1985), *The propagation of radio waves: the theory of radio waves of low power in the ionosphere and magnetosphere*, Cambridge University Press.

Burke, C. P., and D. L. Jones (1992), An experimental investigation of ELF attenuation rates in the earth-ionosphere duct, *Journal of Atmospheric and Terrestrial Physics*, *54*, 243–250.

Calvert, W., and J. Warnock (1969), Ionospheric irregularities observed by topside sounders, *Proceedings of the IEEE*, *57*, 1099–1025, doi:10.1109/PROC.1969.7146.

Carpenter, D. L. (1963), Whistler Evidence of a 'Knee' in the Magnetospheric Ionization Density Profile, *J. Geophys. Res.*, *68*, 1675–1682, doi:10.1029/JZ068i006p01675.

Carpenter, D. L. (1968), Ducted Whistler-Mode Propagation in the Magnetosphere: A Half-Gyrofrequency Upper Intensity Cutoff and Some Associated Wave Growth Phenomena, *J. Geophys. Res.*, *73*, 2919, doi:10.1029/JA073i009p02919.

Carpenter, D. L., and R. R. Anderson (1992), An ISEE/Whistler model of equatorial electron density in the magnetosphere, *J. Geophys. Res.*, *97*, 1097–1108, doi:10.1029/91JA01548.

Carpenter, D. L., and Z. T. Bao (1983), Occurrence properties of ducted whistler-mode signals from the new VLF transmitter at Siple Station, Antarctica, *J. Geophys. Res.*, *88*, 7051–7057, doi:10.1029/JA088iA09p07051.

Carpenter, D. L., and T. R. Miller (1976), Ducted magnetospheric propagation of signals from the Siple, Antarctica, VLF transmitter, *J. Geophys. Res.*, *81*, 2692–2700, doi:10.1029/JA081i016p02692.

Carpenter, D. L., and T. R. Miller (1983), Rare ground-based observations of Siple VLF transmitter signals outside the plasmapause, *J. Geophys. Res.*, *88*, 10,227–10,232, doi:10.1029/JA088iA12p10227.

Cohen, M. B. (2009), ELF/VLF phased array generation via frequency-matched steering of a continuous HF ionospheric heating beam, Ph.D. thesis, Stanford Univ., CA.

Cohen, M. B., U. S. Inan, and M. A. Golkowski (2008), Geometric modulation: A more effective method of steerable ELF/VLF wave generation with continuous HF heating of the lower ionosphere, *Geophys. Res. Lett.*, *35*, L12101, doi:10.1029/2008GL034061.

Cohen, M. B., U. S. Inan, M. Gołkowski, and N. G. Lehtinen (2010a), On the generation of ELF/VLF waves for long-distance propagation via steerable HF heating of the lower ionosphere, *Journal of Geophysical Research (Space Physics)*, *115*, A07322, doi:10.1029/2009JA015170.

Cohen, M. B., U. S. Inan, M. Gołkowski, and M. J. McCarrick (2010b), ELF/VLF wave generation via ionospheric HF heating: Experimental comparison of amplitude modulation, beam painting, and geometric modulation, *Journal of Geophysical Research (Space Physics)*, *115*, A02302, doi:10.1029/2009JA014410.

Cohen, M. B., U. S. Inan, and E. W. Paschal (2010c), Sensitive Broadband ELF/VLF Radio Reception With the AWESOME Instrument, *IEEE Transactions on Geoscience and Remote Sensing*, *48*, 3–17, doi:10.1109/TGRS.2009.2028334.

Cohen, M. B., U. S. Inan, D. Piddyachiy, N. G. Lehtinen, and M. Gołkowski (2011), Magnetospheric injection of ELF/VLF waves with modulated or steered HF heating of the lower ionosphere, *Journal of Geophysical Research (Space Physics)*, *116*, A06308, doi:10.1029/2010JA016194.

Cotts, B. (2011), Global Quantification of Lighting-Induced Electron Precipitation Using Very Low Frequency Remote Sensing, Ph.D. thesis, Stanford Univ., CA.

Cummer, S. A., and U. S. Inan (1997), Measurement of charge transfer in sprite-producing lightning using ELF radio atmospherics, *Geophys. Res. Lett.*, *24*, 1731–1734, doi:10.1029/97GL51791.

Cummer, S. A., U. S. Inan, and T. F. Bell (1998), Ionospheric D region remote sensing using VLF radio atmospherics, *Radio Science*, *33*, 1781, doi:10.1029/98RS02381.

Davies, K. (1990), *Ionospheric Radio*, Peter Peregrinus Ltd. on behalf of the Institution of Electrical Engineers.

Davis, T. N., and M. Sugiura (1966), Auroral electrojet activity index AE and its universal time variations, *J. Geophys. Res.*, *71*, 785–801, doi:10.1029/JZ071i003p00785.

Debye, P. (1911), A note to A. Sommerfeld, I. Runge: Anwendung der Vektorenrechnung auf die Grundlagen der geometrischen Optik, *Ann. Phys*, *35*, 277.

Dowden, R. L., P. Stubbe, and H. Kopka (1981), VLF wave generation by modulated RF heating of the electrojet ionosphere, *Advances in Space Research*, *1*, 221–223, doi:10.1016/0273-1177(81)90295-7.

Duncan, L. M., J. P. Sheerin, and R. A. Behnke (1988), Observations of ionospheric cavities generated by high-power radio waves, *Physical Review Letters*, *61*, 239–242, doi:10.1103/PhysRevLett.61.239.

Dyson, P. L. (1969), Direct Measurements of the Size and Amplitude of Irregularities in the Topside Ionosphere, *J. Geophys. Res.*, *74*, 6291–6303, doi:10.1029/JA074i026p06291.

Elsherbeni, A., and V. Demir (2009), *The Finite-Difference Time-Domain Method for Electromagnetics With MATLAB Simulations*, SciTech Pub.

Ferraro, A. J., H. S. Lee, R. A. Allshouse, K. Carroll, A. A. Tomko, F. J. Kelly, and R. G. Joiner (1982), VLF/ELF radiation from the ionospheric dynamo current system modulated by powerful HF signals, *Journal of Atmospheric and Terrestrial Physics*, *44*, 1113–1122, doi:10.1016/0021-9169(82)90022-8.

Ferraro, A. J., H. S. Lee, R. Allshouse, K. Carroll, R. Lunnen, and T. Collins (1984), Characteristics of ionospheric ELF radiation generated by HF heating, *Journal of Atmospheric and Terrestrial Physics*, *46*, 855–865, doi:10.1016/0021-9169(84)90025-4.

Finlay, C. C., et al. (2010), International Geomagnetic Reference Field: the eleventh generation, *Geophysical Journal International*, *183*, 1216–1230, doi:10.1111/j.1365-246X.2010.04804.x.

Frolov, V. L., V. O. Rapoport, G. P. Komrakov, A. S. Belov, G. A. Markov, M. Parrot, J. L. Rauch, and E. V. Mishin (2008), Density ducts formed by heating the Earth's ionosphere with high-power HF radio waves, *Soviet Journal of Experimental and Theoretical Physics Letters*, *88*, 790–794, doi:10.1134/S002136400824003X.

Getmantsev, G. G., N. A. Zuikov, D. S. Kotik, L. F. Mironenko, N. A. Mitiakov, V. O. Rapoport, I. A. Sazonov, V. I. Trakhtengerts, and V. I. Eidman (1974), Combination frequencies in the interaction between high-power short-wave radiation and ionospheric plasma, *JETP Letters*, *20*, 229–232.

Gibby, A. (2008), Saturation Effects in VLF Triggered Emissions, Ph.D. thesis, Stanford University.

Ginsburg, V. I. (1960), *The propagation of electromagnetic waves in plasmas.*, Gos. izd. fiz.-mat. lit-ry.

Golden, D. I. (2011), Source variation and ground accessibility of magnetospheric mid-latitude ELF/VLF chorus and hiss, Ph.D. thesis, Stanford Univ., CA.

Golden, D. I., M. Spasojevic, and U. S. Inan (2009), Diurnal dependence of ELF/VLF hiss and its relation to chorus at L = 2.4, *Journal of Geophysical Research (Space Physics)*, *114*, A05212, doi:10.1029/2008JA013946.

Golkowski, M. (2008), Magnetospheric wave injection by modulated HF heating of the auroral electrojet, Ph.D. thesis, Stanford University.

Golkowski, M., U. S. Inan, A. R. Gibby, and M. B. Cohen (2008), Magnetospheric amplification and emission triggering by ELF/VLF waves injected by the 3.6 MW HAARP ionospheric heater, *J. Geophys. Res.*, *113*(A10), A10,201.

Golkowski, M., U. S. Inan, and M. B. Cohen (2009), Cross modulation of whistler mode and hf waves above the haarp ionospheric heater, *Geophys. Res. Lett.*, *36*(15), L15,103.

Golkowski, M., U. S. Inan, M. B. Cohen, and A. R. Gibby (2010), Amplitude and phase of nonlinear magnetospheric wave growth excited by the HAARP HF heater, *Journal of Geophysical Research (Space Physics)*, *115*, A00F04, doi: 10.1029/2009JA014610.

Gondarenko, N. A., P. N. Guzdar, G. M. Milikh, and S. L. Ossakow (2002), Modification of the electron density profile near the upper hybrid layer during radio wave heating of the ionosphere, *Geophys. Res. Lett.*, *29*(11), 1510, doi: 10.1029/2002GL014934.

Gross, S. H., and D. B. Muldrew (1984), Uniformly spaced field-aligned ionization ducts, *J. Geophys. Res.*, *89*, 8986–8996, doi:10.1029/JA089iA10p08986.

Helliwell, R. A. (1965), *Whistlers and Related Ionospheric Phenomena*, Stanford University Press.

Helliwell, R. A., and J. P. Katsufrakis (1974), VLF Wave Injection into the Magnetosphere from Siple Station, Antarctica, *J. Geophys. Res.*, *79*, 2511–2518, doi: 10.1029/JA079i016p02511.

Helliwell, R. A., J. P. Katsufrakis, T. F. Bell, and R. Raghuram (1975), VLF line radiation in the earth's magnetosphere and its association with power system radiation, *J. Geophys. Res.*, *80*, 4249–4258, doi:10.1029/JA080i031p04249.

Hunsucker, R., and J. Hargreaves (2003), *The high-latitude ionosphere and its effects on radio propagation*, Cambridge Univ. Press.

Inan, U. (1977), Non-linear gyroresonant interactions of energetic particles and coherent VLF waves in the magnetosphere, Ph.D. thesis, Stanford University.

Inan, U., and M. Gołkowski (2010), *Principles of Plasma Physics for Engineers and Scientists*, Cambridge University Press.

Inan, U., and A. Inan (2000), *Electromagnetic waves*, Prentice Hall.

Inan, U., and R. Marshall (2011), *Numerical Electromagnetics: The FDTD Method*, Numerical Electromagnetics: The FDTD Method, Cambridge University Press.

Inan, U. S., and T. F. Bell (1977), The plasmapause as a VLF wave guide, *J. Geophys. Res.*, *82*, 2819–2827, doi:10.1029/JA082i019p02819.

Inan, U. S., T. F. Bell, and R. R. Anderson (1977a), Cold plasma diagnostics using satellite measurements of VLF signals from ground transmitters, *J. Geophys. Res.*, *82*, 1167–1176, doi:10.1029/JA082i007p01167.

Inan, U. S., T. F. Bell, D. L. Carpenter, and R. R. Anderson (1977b), Explorer 45 and Imp 6 observations in the magnetosphere of injected waves from the Siple Station VLF transmitter, *J. Geophys. Res.*, *82*, 1177–1187, doi:10.1029/JA082i007p01177.

Inan, U. S., M. B. Cohen, R. K. Said, D. M. Smith, and L. I. Lopez (2006), Terrestrial gamma ray flashes and lightning discharges, *Geophys. Res. Lett.*, *33*, L18802, doi: 10.1029/2006GL027085.

Inan, U. S., D. Piddyachiy, W. B. Peter, J. A. Sauvaud, and M. Parrot (2007), DEMETER satellite observations of lightning-induced electron precipitation, *Geophys. Res. Lett.*, *34*, L07103, doi:10.1029/2006GL029238.

Inan, U. S., et al. (2004), Multi-hop whistler-mode ELF/VLF signals and triggered emissions excited by the HAARP HF heater, *Geophys. Res. Lett.*, *31*(24), L24,805.

James, H., R. Dowden, M. Rietveld, P. Stubbe, and H. Kopka (1984), Simultaneous observations of ELF waves from an artificially modulated auroral electrojet in space and on the ground, *J. Geophys. Res.*, *89*(A3), 1655–1666, doi: 10.1029/JA089iA03p01655.

Jones, D., and C. Burke (1995), ELF radio, in *100 Years of Radio, 1995., International Conference on*, pp. 101 –106, doi:10.1049/cp:19950798.

Kamide, Y., and A. Brekke (1993), Altitude variations of ionospheric currents at auroral latitudes, *Geophys. Res. Lett.*, *20*, 309–312, doi:10.1029/93GL00335.

Kamide, Y., S.-I. Akasofu, B.-H. Ahn, W. Baumjohann, and J. L. Kisabeth (1982), Total current of the auroral electrojet estimated from the IMS Alaska meridian chain of magnetic observatories, *Planet. Space Sci.*, *30*, 621–625, doi: 10.1016/0032-0633(82)90022-8.

Kapustin, I. N., R. A. Pertsovskii, A. N. Vasilev, V. S. Smirnov, O. M. Raspopov, L. E. Soloveva, A. A. Uliachenko, A. A. Arykov, and N. V. Galakhova (1977), Generation of radiation at combination frequencies in the region of the auroral electric jet, *JETP Letters*, *25*, 248–251.

Kelley, M. (2009), *The Earth's ionosphere: plasma physics and electrodynamics*, vol. 96, Elsevier Inc.

Kelley, M. C. (1972), Relationship between Electrostatic Turbulence and Spread F, *J. Geophys. Res.*, *77*, 1327–1329, doi:10.1029/JA077i007p01327.

Kennedy, E. J., and P. Kossey (2002), Description of the HAARP Gakona facility with some results from recent research, *Proc. of XXVIIth General Assembly of URSI*, Maastricht, 17-24 August.

Kimura, I., A. Wong, B. Chouinard, M. McCarrick, and T. Okada (1991), Satellite and ground observations of HIPAS VLF modulation, *Geophys. Res. Lett.*, *18*, 309–312, doi:10.1029/91GL00029.

Kimura, I., P. Stubbe, M. T. Rietveld, R. Barr, K. Ishida, Y. Kasahara, S. Yagitani, and I. Nagano (1994), Collaborative experiments by Akebono satellite, Tromso ionospheric heater, and European incoherent scatter radar, *Radio Science*, *29*, 23–37, doi:10.1029/93RS01727.

Kivelson, M., and C. Russell (1995), *Introduction to Space Physics*, Cambridge atmospheric and space science series, Cambridge University Press.

Kravcov, J., and J. Orlov (1980), *Geometricheskaja optika neodnorodnych sred*, Nauka.

Landau, L., and E. Lifshitz (1976), *Mechanics*, Course of theoretical physics, Butterworth-Heinemann.

Lebreton, J.-P. (2012), On the issue of surface contamination of a Langmuir Probe sensor: Demeter ISL results, in *EGU General Assembly 2012*, *Geophysical Research Abstracts*, vol. 14.

Lebreton, J.-P., et al. (2006), The ISL Langmuir probe experiment processing onboard DEMETER: Scientific objectives, description and first results, *Planet. Space Sci.*, *54*, 472–486, doi:10.1016/j.pss.2005.10.017.

Lefeuvre, F., et al. (1985), Detection from AUREOL-3 of the modulation of auroral electrojet by HF-heating from ELF signals in the upper ionosphere above Tromsoe (Norway), in *CNES Results of the ARCAD 3 Project and of Recent Programs in Magnetospheric and Ionospheric Physics p 609-619 (SEE N87-10541 01-46)*, pp. 609–619.

Lehtinen, N. G., and U. S. Inan (2008), Radiation of ELF/VLF waves by harmonically varying currents into a stratified ionosphere with application to radiation by a modulated electrojet, *Journal of Geophysical Research (Space Physics)*, *113*, A06301, doi:10.1029/2007JA012911.

McCarrick, M. J., D. D. Sentman, A. Y. Wong, R. F. Wuerker, and B. Chouinard (1990), Excitation of ELF waves in the Schumann resonance range by modulated HF heating of the polar electrojet, *Radio Sci.*, *25*(6), 1291–1298.

McIlwain, C. E. (1961), Coordinates for Mapping the Distribution of Magnetically Trapped Particles, *J. Geophys. Res.*, *66*, 3681–3691, doi:10.1029/JZ066i011p03681.

McNeill, J. D., and V. F. Labson (1991), Geological Mapping Using VLF Radio Fields, doi:10.1190/1.9781560802686.ch7.

Meredith, N. P., R. B. Horne, and R. R. Anderson (2001), Substorm dependence of chorus amplitudes: Implications for the acceleration of electrons to relativistic energies, *J. Geophys. Res.*, *106*, 13,165–13,178, doi:10.1029/2000JA900156.

Meredith, N. P., R. B. Horne, R. M. Thorne, D. Summers, and R. R. Anderson (2004), Substorm dependence of plasmaspheric hiss, *Journal of Geophysical Research (Space Physics)*, *109*, A06209, doi:10.1029/2004JA010387.

Milikh, G. M., K. Papadopoulos, M. McCarrick, and J. Preston (1999), ELF emission generated by the HAARP HF-heater using varying frequency and polarization, *Radiophysics and Quantum Electronics*, *42*, 639–646, doi:10.1007/BF02676849.

Milikh, G. M., K. Papadopoulos, H. Shroff, C. L. Chang, T. Wallace, E. V. Mishin, M. Parrot, and J. J. Berthelier (2008), Formation of artificial ionospheric ducts, *Geophys. Res. Lett.*, *351*, L17104, doi:10.1029/2008GL034630.

Mironenko, L. (2000), Experimental'noe issledovanie izlucheniya pri svehsvetovom dvizhenii radiozajchika vdol' nizhnej granicy ionosphery, Ph.D. thesis, Nizhny Novgorod Radiophysics Research Institute.

Moldwin, M. B., L. Downward, H. K. Rassoul, R. Amin, and R. R. Anderson (2002), A new model of the location of the plasmapause: CRRES results, *Journal of Geophysical Research (Space Physics)*, *107*, 1339, doi:10.1029/2001JA009211.

Moore, R. (2007), ELF/VLF Wave Generation by Modulated HF Heating of the Auroral Electrojet, Ph.D. thesis, Stanford University.

Moore, R. C., U. S. Inan, T. F. Bell, and E. J. Kennedy (2007), ELF waves generated by modulated HF heating of the auroral electrojet and observed at a ground distance of ~4400 km, *J. Geophys. Res.*, *112*, A05309, doi:10.1029/2006JA012063.

Navy Fact File (2001), Extremely Low Frequency Transmitter Site Clam Lake, Wisconsin, *Tech. rep.*, The U.S. Navy.

Nygren, T. (1982), A method of full wave analysis with improved stability, *Planet. Space Sci.*, *30*, 427–430, doi:10.1016/0032-0633(82)90048-4.

Papadopoulos, K., C. L. Chang, P. Vitello, and A. Drobot (1990), On the efficiency of ionospheric ELF generation, *Radio Science*, *25*, 1311–1320, doi:10.1029/RS025i006p01311.

Parrot, M. (2006), Special issue of Planetary and Space Science 'DEMETER', *Planet. Space Sci.*, *54*, 411–412, doi:10.1016/j.pss.2005.10.012.

Parrot, M., et al. (2006), The magnetic field experiment IMSC and its data processing onboard DEMETER: Scientific objectives, description and first results, *Planet. Space Sci.*, *54*, 441–455, doi:10.1016/j.pss.2005.10.015.

Payne, J. A., U. S. Inan, F. R. Foust, T. W. Chevalier, and T. F. Bell (2007), HF modulated ionospheric currents, *Geophys. Res. Lett.*, *34*, L23101, doi:10.1029/2007GL031724.

Peter, W. B. (2007), Quantitative Measurement of Lightning-Induced Electron Precipitation using VLF Remote Sensing, Ph.D. thesis, Stanford Univ., CA.

Pfaff, R. F., C. L. Jr., J.-J. Berthelier, M. Malingre, M. Parrot, , and J.-P. Lebreton (2008), Demeter satellite observations of plasma irregularities in the topside ionosphere at low, middle, and sub-auroral latitudes and their dependence on magnetic storms, *Midlatitude Ionospheric Dynamics and Disturbances, Geophys. Monogr. Ser.*, *181*, 297–310, doi:10.1029/181GM27.

Piddyachiy, D., U. S. Inan, T. F. Bell, N. G. Lehtinen, and M. Parrot (2008), DEMETER observations of an intense upgoing column of ELF/VLF radiation excited by the HAARP HF heater, *Geophys. Res. Lett.*, *113*, A10308, doi: 10.1029/2008JA013208.

Piddyachiy, D., T. F. Bell, J.-J. Berthelier, U. S. Inan, and M. Parrot (2011), DEMETER observations of the ionospheric trough over HAARP in relation to HF heating experiments, *Journal of Geophysical Research (Space Physics)*, *116*, A06304, doi: 10.1029/2010JA016128.

Platino, M., U. S. Inan, T. F. Bell, J. Pickett, E. J. Kennedy, J. G. Trotignon, J. L. Rauch, and P. Canu (2004), Cluster observations of ELF/VLF signals generated by modulated heating of the lower ionosphere with the HAARP HF transmitter, *Annales Geophysicae*, *22*(7), 2643–2653, doi:10.5194/angeo-22-2643-2004.

Platino, M., U. S. Inan, T. F. Bell, M. Parrot, and E. J. Kennedy (2006), DEMETER observations of ELF waves injected with the HAARP HF transmitter, *Geophys. Res. Lett.*, *33*, L16101, doi:10.1029/2006GL026462.

Raghuram, R., R. Smith, and T. Bell (1974), Vlf antarctic antenna: Impedance and efficiency, *Antennas and Propagation, IEEE Transactions on*, *22*(2), 334 – 338, doi:10.1109/TAP.1974.1140777.

Ratcliffe, J. (1959), *The magneto-ionic theory and its applications to the ionosphere*, Cambridge Univ. Press.

Reising, S. C., U. S. Inan, T. F. Bell, and W. A. Lyons (1996), Evidence for continuing current in sprite-producing cloud-to-ground lightning, *Geophys. Res. Lett.*, *23*, 3639–3642, doi:10.1029/96GL03480.

Rietveld, M. T., H. Kopka, and P. Stubbe (1986), D-region characteristics deduced from pulsed ionospheric heating under auroral electrojet conditions, *Journal of Atmospheric and Terrestrial Physics*, *48*, 311–326, doi:10.1016/0021-9169(86)90001-2.

Rietveld, M. T., P. Stubbe, and H. Kopka (1989), On the frequency dependence of ELF/VLF waves produced by modulated ionospheric heating, *Radio Science*, *24*, 270–278, doi:10.1029/RS024i003p00270.

Rodger, A. S., R. J. Moffett, and S. Quegan (1992), The role of ion drift in the formation of ionisation troughs in the mid- and high-latitude ionosphere - A review, *Journal of Atmospheric and Terrestrial Physics*, *54*, 1–30, doi:10.1016/0021-9169(92)90082-V.

Said, R. (2009), Accurate and Efficient Long-Range Lightning Geo-Location Using a VLF Radio Atmospheric Waveform Bank, Ph.D. thesis, Stanford University.

Santolík, O., F. Němec, M. Parrot, D. Lagoutte, L. Madrias, and J. J. Berthelier (2006), Analysis methods for multi-component wave measurements on board the DEMETER spacecraft, *Planet. Space Sci.*, *54*, 512–527, doi:10.1016/j.pss.2005.10.020.

Space Science Board (1978), *Space plasma physics: the study of solar-system plasmas*, National Academy of Sciences.

Spasojevic, M. (2003), Global dynamics of the earth's plasmasphere, Ph.D. thesis, Stanford University.

Stix, T. (1992), *Waves in Plasmas*, American Institute of Physics.

Stubbe, P., and H. Kopka (1977), Modulation of polar electrojet by powerful HF waves, *J. Geophys. Res.*, *82*, 2319–2325, doi:10.1029/JA082i016p02319.

Stubbe, P., H. Kopka, and R. L. Dowden (1981), Generation of ELF and VLF waves by polar electrojet modulation Experimental results, *J. Geophys. Res.*, *86*, 9073–9078, doi:10.1029/JA086iA11p09073.

Stubbe, P., H. Kopka, M. T. Rietveld, and R. L. Dowden (1982), ELF and VLF wave generation by modulated HF heating of the current carrying lower ionosphere, *Journal of Atmospheric and Terrestrial Physics*, *44*, 1123–1131, doi: 10.1016/0021-9169(82)90023-X.

Stutzman, W., and G. Thiele (1998), *Antenna theory and design*, J. Wiley.

Taflove, A., and S. Hagness (2005), *Computational Electrodynamics: The Finite-Difference Time-Domain Method*, Artech House Antennas and Propagation Library, Artech House.

Tascione, T. (2010), *Introduction to the Space Environment*, Krieger Publishing.

Temerin, M. (1978), The polarization, frequency, and wavelengths of high-latitude turbulence, *J. Geophys. Res.*, *83*, 2609–2616, doi:10.1029/JA083iA06p02609.

Uman, M. (2001), *The Lightning Discharge*, Dover Publications.

Villasenor, J., A. Y. Wong, B. Song, J. Pau, M. McCarrick, and D. Sentman (1996), Comparison of ELF/VLF generation modes in the ionosphere by the HIPAS heater array, *Radio Sci.*, *31*(1), 211–226.

Wait, J. (1965), Earth-ionosphere cavity resonances and the propagation of elf radio waves, *Radio Science*, *69D*, 1057–1070.

Walt, M. (2005), *Introduction to Geomagnetically Trapped Radiation*, Cambridge Atmospheric and Space Science Series, Cambridge University Press.

Weidman, C. D., and E. P. Krider (1986), The amplitude spectra of lightning radiation fields in the interval from 1 to 20 MHz, *Radio Science*, *21*, 964, doi: 10.1029/RS021i006p00964.

Wong, A. Y., J. Chen, L. C. Lee, and L. Y. Liu (2009), Observation of Large-Scale Density Cavities and Parametric-Decay Instabilities in the High-Altitude Discrete Auroral Ionosphere under Pulsed Electromagnetic Radiation, *Physical Review Letters*, *102*(10), 105002, doi:10.1103/PhysRevLett.102.105002.